Physical Modeling of Subgouge Deformations in Sand

by

©Wei Yang

St. John's, Newfoundland, Canada

B.Eng., Harbin institute of technology, China (2005)

A thesis submitted to the
School of graduate studies
In partial fulfillment of the
Requirements for the degree of
Master of engineering

Faculty of Engineering and Applied Science
Memorial University of Newfoundland

December 2009

ABSTRACT

A series of 7 tests of PIRAM (Pipeline Ice Risk Assessment and Mitigation) tests were carried out to simulate the progress of a gouging ice keel by centrifuge modeling. This thesis focuses on the subgouge deformations of the ice gouging process. The relationships between gouge depth, frontal berm, force, pressure, subgouge deformation and vertical extent of subgouge deformation are discussed in the thesis. The PIRAM tests were compared with the results of a similar series of previously conducted tests, and previous tests. Significance of the frontal berm height, gouge depth, gouge rate are also discussed.

The experimental program consisted of towing a model ice keel across a model testbed at a set gouge depth under various centrifuge acceleration. The test setup consisted of an aluminum half width ice keel model mounted on a gantry situated on top of the containment box given the centerline of the model was replaced by a viewing window to visualize the subgouge deformation accumulation. The model tests were conducted using saturated fine sand simulating seabed. Two tests were conducted with shallow gouge depths for comparison with previous Delft Hydraulics flume medium scale gouge tests to evaluate the applicability of centrifuge modeling. Three tests were conducted at a fast gouge rate since most of the previous work were conducted at a relatively slow rate. A large amount of data regarding ice keel gouge in sand was acquired from the experimental program the analysis of which described here in.

The combined depth of gouge depth and frontal berm height has a significant effect on the force and subgouge deformation. The force per unit width increases as the gouge depth increases. The vertical to lateral gouge force ratio seems to be independent of the aspect ratio which is gouge width divide gouge depth or attack angle. The kappa value is the frontal bern height normalized by gouge depth is linear with the aspect ratio. The kappa value has a significant effect on gouge force and subgouge deformation. Particle image velocimetry (PIV) technique was successfully used to track the evolution of subgouge deformation in all 7 tests. The maximum horizontal subgouge displacement occurred at the base of the keel and decreased with depth. The associated maximum gouge forces are a function of the keel attack angle and the gouge geometry. In comparison with previous tests, the vertical extent of subgouge deformation (SGD) was a function of combined depth and the soil state, but independent of the attack angle. The SGD are influenced by the attack angle and the soil state. Faster gouge rates may result in larger gouge forces by a factor of 2 to 3 and smaller horizontal subgouge deformations but similar vertical extent.

TABLE OF CONTENTS

LIST OF FIGURES

LIST OF TABLES

NOMENCLATURE

c_v	coefficient of consolidation
d	diameter of penetrometer
D_s, D	gouge depth
D_r	relative density
F_h	Horizontal component of gouge force
F_v	Vertical component of gouge force
I_r	Dilation index
N	gravitational acceleration
v	penetration rate / keel velocity
V	normalised penetration rate
V*	normalised gouging rate
W	gouge width
α	gouge attack angle
κ	frontal berm height as multiple of gouge depth
ν	pore fluid viscosity
σ_b	bearing pressure

1 INTRODUCTION AND LITERATURE REVIEW

1.1 Introduction

An ice gouge, Figure 1-1 is formed when an iceberg or pressure ridge keel is propelled laterally in contact with the seabed. Because of an iceberg's massive size, a huge gouge can be created. Growing ice ridges and multi-year ice floes continuously gouge continental shelves in arctic regions.

The traces made by ice keel gouge can have multiple lines, such as elongated curvilinear and linear seafloor incisions. Research indicates some of the important factors that affect ice gouge, include soil resistance, ice strength, keel geometry and driving force are variables that need to be considered in an analysis. It is a complex calculation in which the related factors, alternately or combined act.

The ice gouge event can pose a significant threat on sub-sea facilities such as pipelines, cables, wellheads and also templates. These sub-sea facilities can be protected from ice keel damage is by installing facilities below the seabed. In Canada, both arctic and eastern offshore regions are acquiring more accurate information to verify models of ice keel gouge.

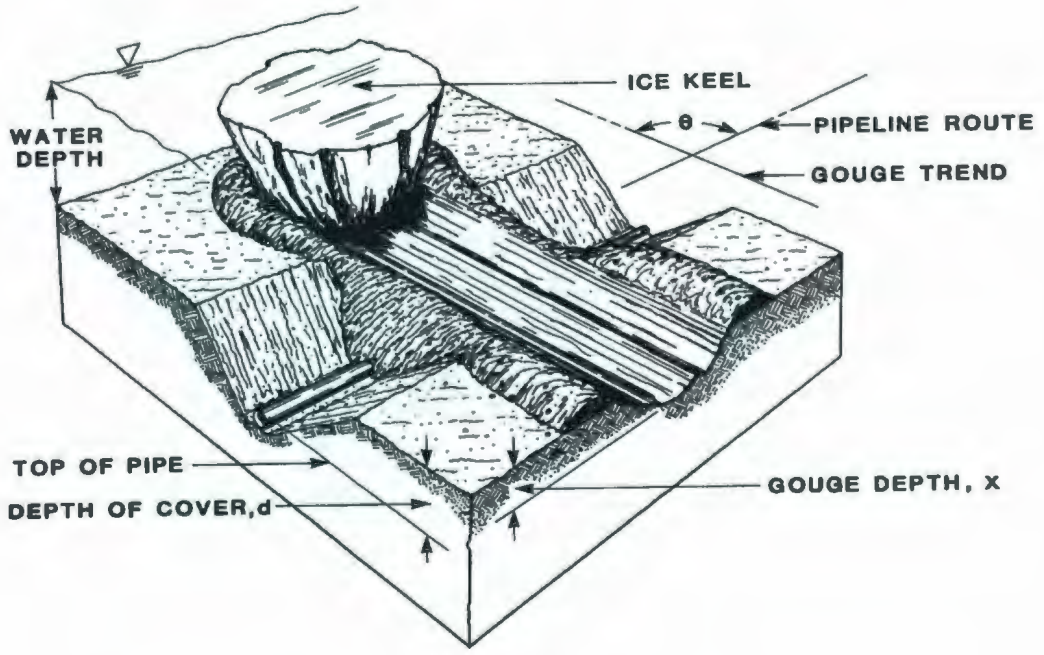

Figure 1-1 Ice gouge, Lanan et al. (1986)

1.2 Gouge Geometry

A gouging ice keel pushes a mound of seabed soil ahead of itself. The soil is brought up on both sides of the gouge. The width of the gouge is usually many times its depth. The gouge depth and gouge width usually keep the same level over distances of kilometers.

Despite the large mass of icebergs, the environmental driving forces are more important. So icebergs move by the driving forces. If icebergs travel at a low velocity, because their large mass, they nonetheless have high kinetic energy.

As shown in Figure 1-2, free floating pressure ridge keel side slope angles have a mean value of 26.6 degrees (Timco and Burden, 1997). Phillips et al. (2005) had indicated that under steady conditions, the ice keel will have been reoriented and reshaped after gouging. From field observations, it is assumed that the attack angle between the keel and the soil is about 15 to 30 degrees.

Gouge characteristics include depth, width, orientation, length, frequency and spatial density. Many offshore and field studies have focused on the ice gouge. Woodworth et. al. (1996) observed ice gouge formed in clayey silt at Cobequid Bay in the Bay of Fundy and in the St. Lawrence estuary. One gouge field has also been observed in southeast Manitoba, beneath the bed of former Lake Agassiz. The gouges were formed in silty clay at a water level of about 110 m, Woodworth et. al. (1996)

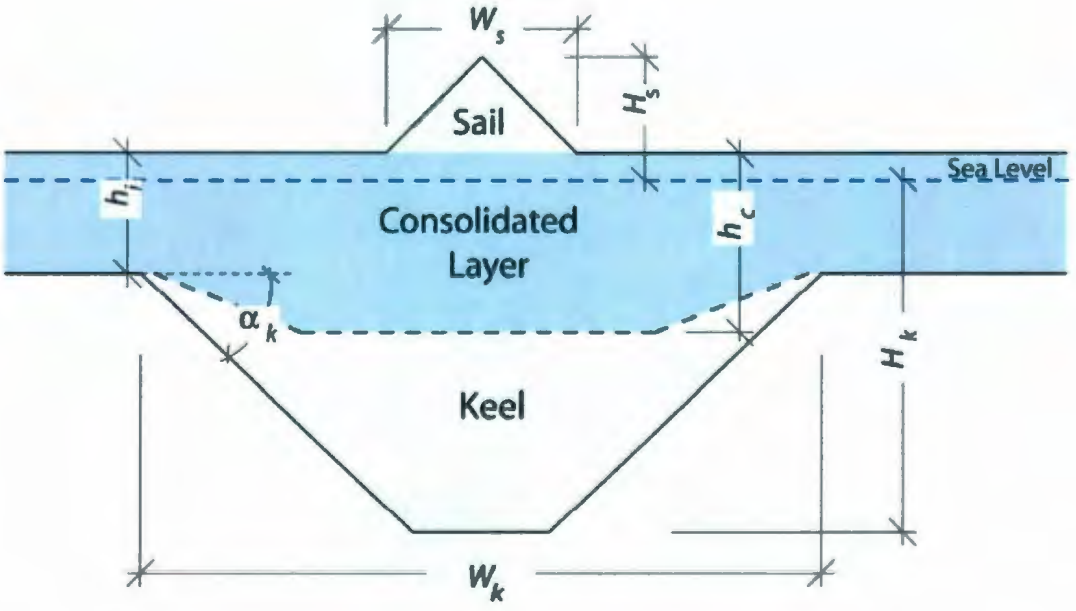

Figure 1-2 Keel side slope angle

There is a large amount of data showing measurements of gouge depths and gouge depth statistics from different areas. Researchers have observed at water depth between 15 m and 20 m in Alaska' Beaufort Sea coast which include 3046 gouges with a depth of between 0.2 m and 1.6 m, Weeks et al. (1983). They found that the depth distribution of ice keel gouges follows a straight line on a semi-logarithmic data plot:

$F(x) = \lambda e^{-\lambda(x-c)}$ for x>c. Where, F(x) is the probability density function for ice gouges. x(k) is ice gouge depth. C (k) is the cutoff depth below which gouges become too small to identify and count (and the ice gouge depth which all of the observed ice gouges exceed). λ is a constant specifying the slope of the negative exponential gouge depth distribution curve, Lanan et al (1986).

1.3 Studies of Ice Gouge

Small-scale physical models and large scale physical models are used to study the ice soil interaction and subgouge soil movement. To determine the force and the displacement under the seabed, Clark et al. (1990) has done small scale tests with 0.5 m for the gouge width in loose and medium density sand. Figure 1-3 shows the influence of the soil strength on the sub-gouge deformation, Clark et al. (1990). The small scale tests with 0.5 m for the gouge width in loose sand have larger depth of disturbance below gouge.

The Chari model, Chari (1975) is an energy model that considers an ice gouge is driven by the mass of the iceberg, current drag and wind. The resistance of the gouge is dependent on the length, width and depth of the gouge, the unit weight of the soil and the

shear strength of the soil. Surkov's model, Surkov (1995), is similar to the Chari model in that they all involve the horizontal translation of an ice feature into a sloped seabed.

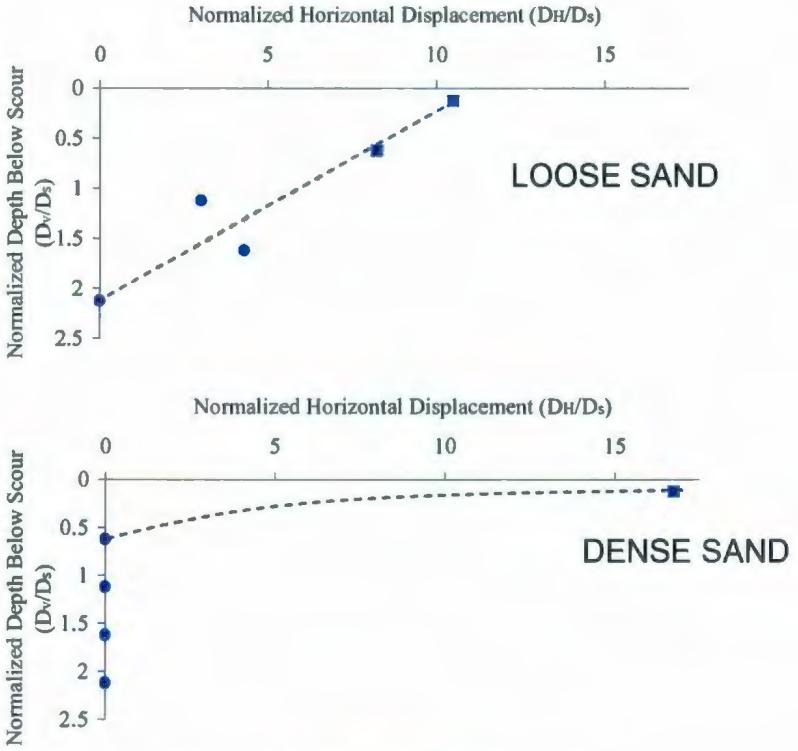

Dv – Depth of disturbance below gouge
DH – Horizontal displacement
Ds- gouge depth

Figure 1-3 Small scale test in sand width 0.5 m, Clark et al. (1990)

The Flume test, Vershinin et al. (2007) is medium-scale test of scale 1:5 to 1:10. A total of 29 tests were conducted using a half-keel with a glass wall so that it can have visual information of the process. The subgouge deformations are limited between the bottom of the keel and 250 mm below the bottom of the keel. The keel model is made by steel with the attack angles 15 degree, 30 degree and 45 degree. Figure 1-4 shows the force vectors. Increasing the keel angle decreases in horizontal force which is related to the change of

direction of the friction force on the keel surface. At low attack angles, the friction force on the keel surface is downwards. Around 30 degree angle, it appears to turn upwards. At higher keel angle, the friction force is directed upward. Friction along the keel bottom would increase the horizontal force. Results from these tests indicated that the smaller attack angle can have the larger deformation. The sub-gouge deformation was determined from digital images by the method of particle tracking.

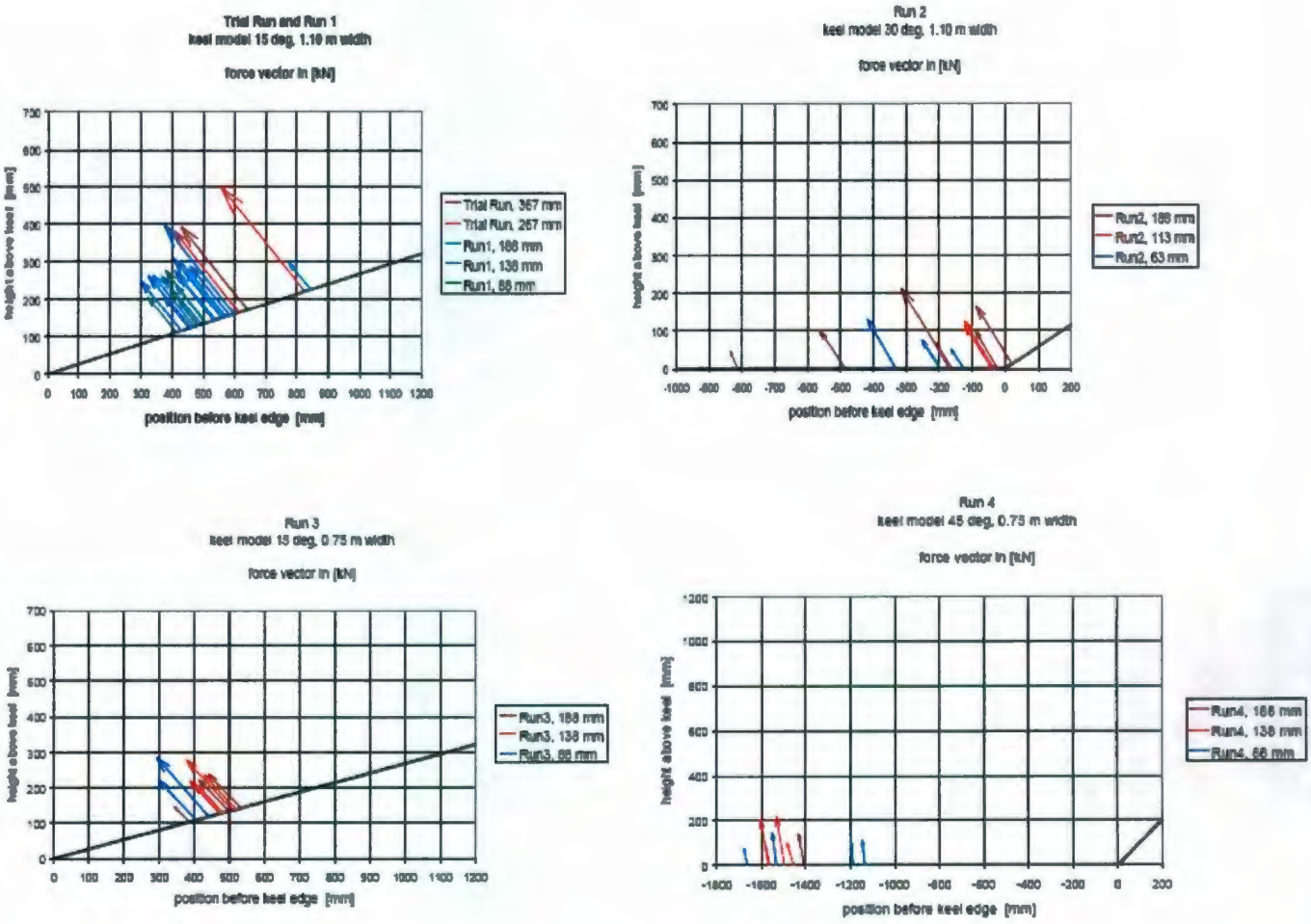

Figure 1-4 Force vectors with keel angle, Vershinin et al. (2007)

Table 1-1 DH Flume (Vershiniin et al., 2007) medium scale sand test parameters

Test I.D.	Attack angle, α (deg)	Dr%	Gouge Depth, Ds (m)	Gouge Width, W (m)	Ir	Velocity, (mm/sec)	F_v kN	F_h kN	F_v/F_h	Kappa
Run 2 test1	30	55	0.19	2.2	2.2	13	67	48	1.39	1.55
Run 2 test2	30	55	0.19	2.2	2.1	12	98	77	1.27	2.51
Run 2 test3	30	65	0.19	2.2	2.3	20	213	147	1.45	2.85

Poorooshasb (1990) undertook medium scale tests in clean silica sand. This research focused on the magnitude and extent of subgouge displacement and finding out if the attack angle, keel width and sand density could affect the gouging progress. The test was using aluminum model ice keel with attack angle 15 degree or 30 degree. This test uses strands of solder and ball bearings to determine the subgouge displacement. Poorooshasb (1990) indicated that the denser the sand density was, the smaller the subgouge deformation would be. The 15 degree keel model test has higher deformation than 30 degree keel model test. The primary direction of displacement was in the direction of travel of the gouging feature.

Table 1-2 Memorial University (Poorooshasb, F. 1990)1g physical model sand test parameters

Test	**Soil Type**	**Relative Density**	**Attack Angle (deg.)**	**Gouge Depth (m)**	**Gouge Width (m)**	**Fh (kN)**	**Fv (kN)**
Poor 2a	Loose Sand	0.09	15	0.075	0.86	6.5	7.25
Poor 2b	Medium Sand	0.33	15	0.075	0.86	8.0	9.0

Paulin (1992) undertook a series of 4 silica tests to continue the Poorooshasb's (1990) sand tests. Paulin (1992) tests were focused on the observation and measurement of the limits of subgouge deformation. The instrument used in Paulin (1992) is similar to Poorooshasb (1990) tests. The test was using aluminum model ice keel with attack angle of 15 degree. Pressure transducers and load cells were used in Paulin (1992) test. Horizontal and vertical subgouge displacement, stress response in the soil and the effect of pore fluid were measured in the tests. Paulin (1992) concluded that horizontal displacements were larger than the vertical displacements.

Table 1-3 Memorial University (Paulin, 1992) 1g physical model sand test parameters

Test	**Soil Type**	**Dry Density (kg/m^3)**	**Attack Angle (deg.)**	**Gouge Depth (m)**	**Gouge Width (m)**	**Fh (kN)**	**Fv (kN)**
Paulin 3	Wet Sand	1365	15	0.038	0.43	0.768	0.969
Paulin 4	Wet Sand	1363	15	0.040	0.43	0.799	0.826

The Pressure Ridge Ice Gouge Experiment (PRISE) led by C-CORE was focused on "developing the capability of designing pipelines and other seabed installations in regions gouged by ice, taking into account the soil deformations and stress changes, which may be caused during a gouge event", Phillips et al. (2005). The PRISE includes five research phases:

- Phase 1: PRISE Planning and Extreme Gouge Dating Project Feasibility Study
- Phase 2: Extreme Gouge Dating Project
- Phase 3: Centrifuge and Numerical Modelling, Pipeline Design Guidelines
- Phase 4: Full-Scale Ice Keel/Seabed Interaction Event
- Phase 5: Full-Scale Ice Keel/Seabed/Pipeline Interaction Event

Table 1-4 PRISE (Phillips et. al., 2005) centrifuge sand test program prototype parameters

Test	Soil Type	Relative Density	Attack Angle (deg.)	Gouge Depth (m)	Gouge Width (m)	Fh (MN)	Fv (MN)
Phase 3a							
PR01B-2	Fine Sand	37.4%	15	1.7	15	33.7	35.1
PR01C-1	Fine Sand	37%	30	0.98	15	8.9	8.4
PR01C-2	Fine Sand	37%	15	1.1	15	12.2	14.2
PR09-1	Fine Sand	47.2%	15	1.2	15	19.3	16.4
PR09-2	Fine Sand	47.2%	15	2.14	15	40.3	38.5
PR10-1	Fine Sand	65.9%	30	1.19	30	40.5	38.0
PR10-2	Fine Sand	65.9%	15	1.16	30	45.9	49.9
Phase 3c							
PRSA01	Fine Sand	81%	30	4.5	15	93.8	123.3
PRSA02	Fine Sand	90%	15	2.50	7.5	24.6	28.6
PRSA03	Fine Sand	55%	15	2.10	15	64.4	56.9
PRSA04	Fine Sand	82%	15	2.66	15	74.4	67.3
PRSA05	Fine Sand	69.5%	15	2.5	15	67.3	63.7

Centrifuge modeling was conducted in Phase 3, which is important for determining the subgouge deformation. Phase 3 centrifuge modeling included 9 centrifuge tests in clay, and 20 centrifuge tests in clay, sand, and layered clay/sand soil. The main parameters for the tests were soil type, soil condition, attack angle, gouge width and gouge depth. Gouge depth for sand tests is from 0.98m to 4.5m. Gouge width for sand tests are 7.5m, 15m, and 30m in prototype. Attack angle are 15 degree and 30 degree (Table 1-4). The PRISE

sand tests focused on the significance of subgouge deformation to assess the safe burial depths for pipelines against ice gouging. These sand tests are compared with PIRAM tests in section 6.5.

1.4 Theorical and Numerical Studies

1.4.1 Ice Gouge Life Cycle

Because the gouge is formed by the ice keel driving across the seabed, soil is heaped on each side of the gouge. After the ice keel moves away, the soil piled on each side may flow back into the gouge, so the gouge depth will be reduced, Figure 1-5. After the ice gouge has formed, it will not keep the same depth but will keep changing. The gouge will become partially infilled.

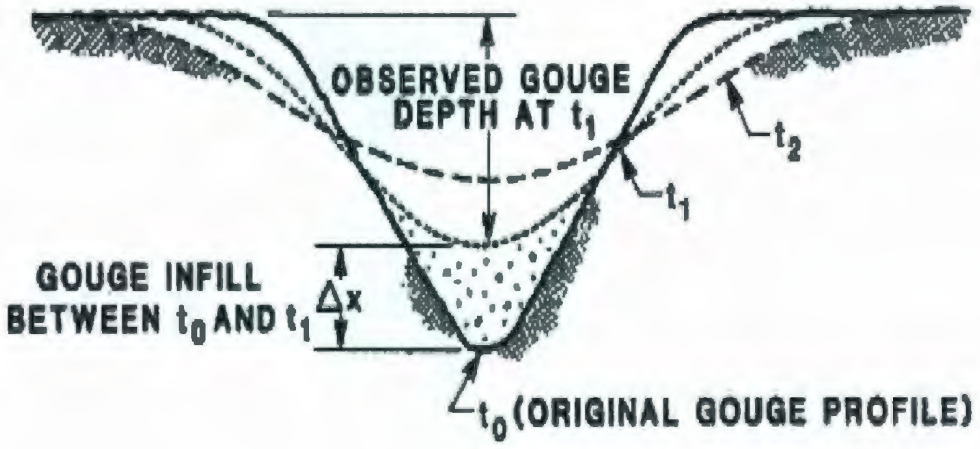

Figure 1-5 Ice gouge life cycle, Lanan et al (1986)

1.4.2 Ice Gouge Parameters with Pipeline Design

There are some necessary components for ice gouge. These include the width of the keel, the depth of the gouge, the contact angle of the ice keel, which are the important parameters for offshore pipeline design. The relationship between ice gouge parameters and offshore pipeline design is shown in Table 1-5.

Table 1-5 Ice gouge parameters with pipeline design, Comfort & Graham (1986)

Ice gouge parameters	**Effect on pipeline design**
Gouge depth	Design trench depth
Keel width	Requirement of damage and repair
Keel residence time	Potential for accessibility to repair site
Variation with water depth	Establishes practical use of dredging equipment
Critical exposure period	Influence repair response
Directionality of gouge	Influences risk and length of potential damage for specific routes
Mechanism of gouge Keel-soil interaction Available forces Keel strength Keel shape	Defines feasible methods of protection
Correlation to surface ice conditions	Defines feasibility of installation repair
Influence of structure	Defines special requirements for trenching near structures
Frequency of occurrence	Defines trench depth

The parameter of the keel residence time is related to the time needed for repair. The variation of ice gouge with water depth is important for designing the offshore pipeline because it determines the equipment used for trenching the pipeline. The directionality of gouge is important in estimating the higher risk but shorter length of damage, which is important for economic consideration. The method of burying and covering pipeline is dependent on the mechanism of gouge. The parameters of influence of structure and correlation to surface ice conditions are more related to the operational aspects.

1.4.3 Pipeline Trench Depth

To avoid damage by ice gouge, the pipe may be required to be buried in a trench below the ice gouge level. There are many factors influencing pipeline depth, such as the behavior of the ice keel, the backfill, the level of the risk that can be accepted, and so on. For designing the pipeline, it is important to know the geometry of the ice gouge. The next one which is also important for designing pipeline is how much forces will be transferred from the ice keel to the seabed and thus to the pipeline.

It is generally agreed that the ice gouge depth can in some part decide the pipeline burial depth. If the ice gouge depth is more than the pipeline burial depth, the pipeline will be damaged. If the pipeline burial depth is larger than the ice gouge depth, there may not be significant damage on pipeline by ice gouge

Palmer (1990) has assumed three zones of deformation, Figure 1-6. Zone 1 is a zone of large deformation in which the soil is moved by ice keel. Zone 2 also has large

deformation that the soil has plastic deform and the location is under the ice keel. Zone 3 is a zone with small elastic deformation. It is easy to see the boundary between zone 1 and zone 2. This boundary is defined by the gouge depth. The boundary between zone 2 and zone 3 can be seen as separate in that the deformation in zone 2 is plastic and the deformation in zone 3 is elastic. It is affected by the driving force, soil type, ice geometry and so on.

A pipeline located in zone 1 is likely to fail in the event of an ice gouge. The pipeline in zone 3 will be safe because there is little deformation in zone 3. However, locating a pipeline in zone 3 may not be economically viable because of the buried depth. The best choice for located the pipeline is in zone 2. In zone 2, there are two aspects to affect the pipeline. They are gouge load and soil displacement. So the combination of the gouge load and soil displacement is the largest damage for the pipeline in this zone. In order to design the pipeline, it is important to calculate the gouge load and soil deformation.

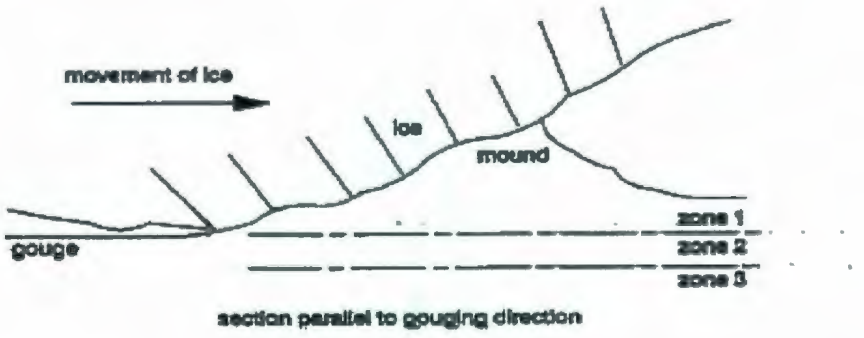

Figure 1-6 Three zones under the ice gouge, Palmer et al. (1990)

King et al. (2008) presented a methodology for a probabilistic pipeline burial analysis for protection against ice gouge. Through a first-order estimate of required pipeline cover depths for a hypothetical gas pipeline on the Grand Banks, the results demonstrate the need to properly combine both ice gouges and pits into the overall scour risk analysis, as well as the influence of ice management on pipeline cover depths required to meet target annual reliability levels.

1.5 Research Objective and Outline

Ice gouging can have detrimental effect on subsea facilities such as wellheads, pipelines and submarine cables. To help understand the significant effect, a large amount of research has been undertaken. Due to field study, small scale physical modeling and large scale physical modeling, the process of ice gouging, ice soil interaction, the profile of subgouge deformation have been understand. As mentioned in section 1.3 experimental studies, many studies has been undertaken before. Delft Hydraulics Flume tests were conducted in small gouge depth. PRISE tests were conducted in sand and clay with large gouge depth. All the previous tests mentioned are conducted in sand saturated with water. PIRAM test which has the objective of developing practices for risk mitigation and protection of pipeline infrastructure from ice keel loading, is developing a set of engineering models to establish probabilistic estimates of the pipeline mechanical behavior in response to ice keel load events, and assess engineering concepts of protection and risk mitigation strategies. The development of methodologies to determine contact frequency and ice keel loads will also form part of the integrated model.

As the component of PIRAM tests, this thesis focuses on the magnitude and the vertical extent of subgouge deformation by PIV techniques. The established experimental objectives included modeling 7 tests using fine sand saturated with viscous pore fluid to retard the dissipation of excess pore pressures, comparing with previous Delft Hydraulics flume medium scale gouge tests to evaluate the applicability of centrifuge modeling. The effects of fast gouge rates in fine sands was a focus as much previous work was conducted at a relatively slow rate.

This thesis comprises seven chapters. Chapter 1 is an introduction and literature review which presents the general deformation of ice keel gouge and the various phenomenological, analytical, and experimental studies from previous researchers. Chapter 2 establishes the principle of centrifuge modeling and discusses the relationship of the scales between the experimental model and prototype. Chapter 3 describes the equipment used for the PIRAM experiment. The procedure of the experiment and the theory of the saturation are presented in Chapter 4. Chapter 5 and Chapter 6 establish the experiment results, analysis and comparison with previous tests. A discussion of the results and the conclusions are presented in the final chapter.

2 CENTRIFUGE MODELING

2.1 Introduction

A centrifuge is a load frame that is used to test soil models, and plays a major role in geotechnical engineering. The model is placed at the end of the centrifuge arm and is rotated about the central axis of the centrifuge. At a high-speed rotation, the model can have a much higher acceleration in the radial direction than that of earths gravity. As the pressure of the soil increases through the depth of the soil, a small-scale model placed on the centrifuge can provide a similar stress profile as the prototype.

A total of seven tests were conducted in the centrifuge, Table 2-1. The first six tests were conducted using a keel with an attack angle of 30 degree. However, the attack angle for the last test was 15°. The two first model tests were conducted relatively slowly in dry, dense, and water-saturated medium density sand to prove the new equipment and techniques. Two tests are included for comparisons to previous Delft Hydraulics flume medium scale gouge tests, to evaluate the applicability of centrifuge modeling. Three tests are conducted with faster gouge rates using a viscous pore fluid to retard excess pore pressure dissipation

Table 2-1 Centrifuge sand test prototype parameters

#	Test I.D.	Attack angle α (deg)	Gouge depth (m)	Gouge width (m)	W/ Ds	Dr (%)	Saturation condition	G level	Keel speed (mm/sec)
1	P02	30	1.3	10	7.6	93.6	Dry	55.6	0.5
2	P03	30	1.4	10	7.0	51.5	Water	55.6	0.5
3	P05	30	0.18	2.2	12	58	30 cst	12.2	1.1
4	P06	30	2.3	14.4	6.25	50.8	30 cst	80	1.1
5	P07	30	2.4	14.4	6.0	39	30 cst	80	5.5
6	P08	30	0.19	2.2	11.3	68.1	30 cst	12.2	55
7	P09	15	1.2	16	13.3	38.6	30 cst	80	57

2.2 Centrifuge Modeling Principle

A soil model that is loaded on the end of the centrifuge arm is rotated around a central axis of the centrifuge. During the rotation progress, the model can get the radial acceleration that provides a higher gravity than Earth. The increased radial acceleration $r\omega^2$ is equal to Ng, where ω is the angular velocity of rotation expressed in radians per second, r is the distance between the object and its axis of rotation and g is the gravitational acceleration, Taylor (1995). When the model and the prototype is using the same soil and has the acceleration of N times of the Earth's gravity, the vertical stress at depth h_m will be identical to that in the corresponding prototype at depth h_p where $h_p = N h_m$, Taylor (1995). This is the basic scaling law of centrifuge modelling. Figure 2-1

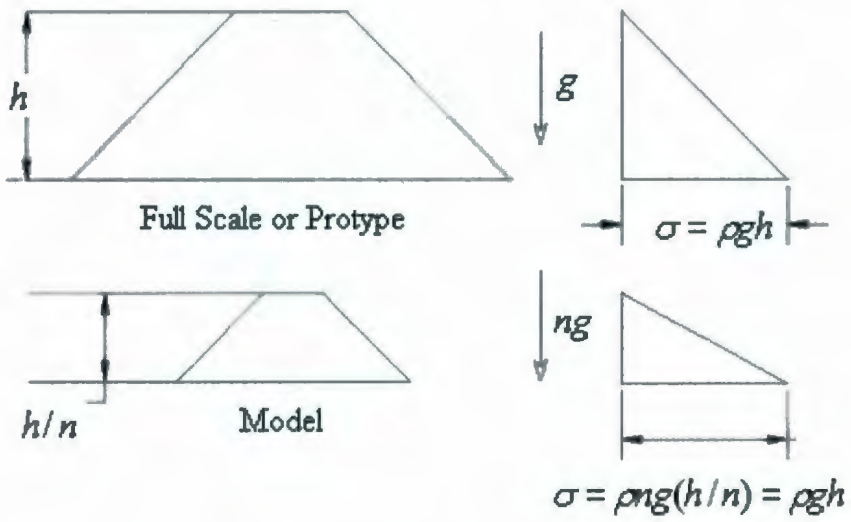

Figure 2-1 Centrifuge scaling

2.3 Scaling Law for Modeling

According to the basic law above, if a model which has the density of ρ and acceleration of N times Earth's gravity, then the vertical stress σ_{vm} at depth h_m in the model is:

$\sigma_{vm} = \rho N g h_m$ Equation 2.1

In the prototype it is:

$\sigma_{vp} = \rho g h_p$ Equation 2.2

Where: ρ represents mass density, g represents earth's gravitational acceleration and h is the depth, Taylor (1995).

As the model is the linear scale of the prototype, so the displacement will also have a scale factor of 1: N. In order to maintain the vertical stress of the soil model at the same level as the vertical stress of the prototype, it is apparent that either the density or the

gravity of the model should be N times that of the prototype when the soil depth of the model h_m is 1/N times of the prototype h_p from the equations 2.1 and 2.2 above. As it is not easy to change the density a lot, the acceleration g must be N times of the Earth's gravity which is present below, Taylor (1995):

$$\sigma_{vm} = \rho N g h_p (1/n) \qquad \text{Equation 2.3}$$

For the non-linear variation of stress in the model, the vertical stress at depth z in the model can be determined from:

$$\sigma_{vm} = \int_0^z \rho\omega^2 (R_t + z) d_z = \rho\omega^2 z (R_t + \frac{z}{2}) \qquad \text{Equation 2.3}$$

Where: R_t is from the radius to the top of the model.

According to the Taylor (1995), there is an exact correspondence in stress between model and prototype at two-thirds model depth. The effective centrifuge radius should be measured from the central axis of the centrifuge to one-third the depth of the model. As the equation shows below:

$$R_e = R_t + \frac{h_m}{3} \qquad \text{Equation 2.5}$$

Where: R_e is the effective radius.

The maximum error is given by equation 2.6:

$$r_u = r_o = \frac{h_m}{6R_e} \qquad \text{Equation 2.6}$$

Where: r_u is the maximum under-stress, r_o is the maximum over-stress. As most geotechnical centrifuge has the h_m / R_e less than 0.2, the maximum error in the stress is minor and less than 3% of the prototype stress. The distribution of vertical stress in the

model and prototype is shown in Figure 2-2. The comparing of the vertical stress of the model and prototype is shown in Figure 2-3 after Taylor (1995)

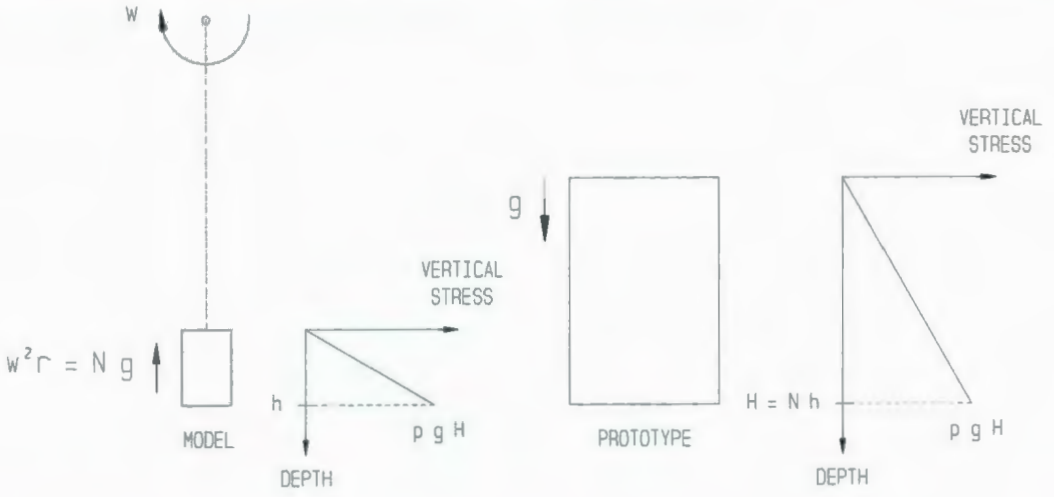

Figure 2-2 The distribution of vertical stress in the model and prototype, Taylor (1995)

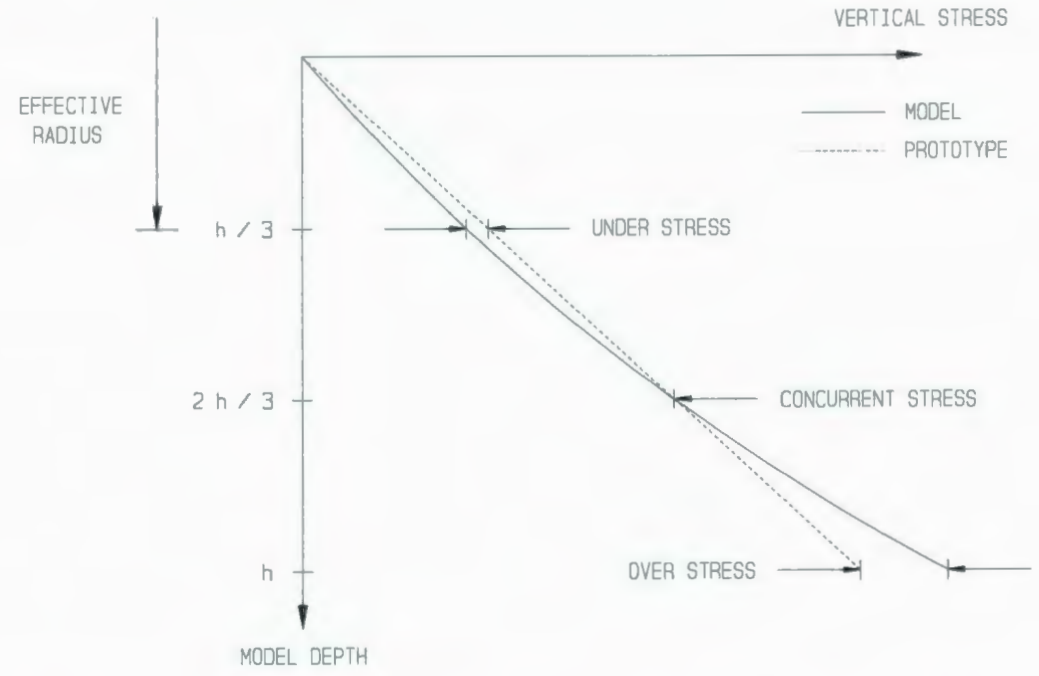

Figure 2-3 Comparison of stress variation with depth in a centrifuge model and its corresponding prototype, Taylor (1995)

Using the inverse relationship between model and prototype length as a starting point, for example, the volume occupied by the model (V_m) in relation in relation to the volume of the prototype (V_p) is given as

$V_m = \frac{1}{N^3} V_p$ So $m_m = \frac{1}{N^3} m_p$

Then we can get: $F_m = m_m a_m = (\frac{1}{N^3}) m_p N a_p$ so $F_m = (\frac{1}{N^2}) F_p$

The centrifuge scaling relationships are shown as Table 2-2

Table 2-2 Centrifuge scaling relationship

Physical Quantity	**Model at Ng**
Gravitational acceleration	N
Linear dimension	1/N
Area	$1/N^2$
Volume	$1/N^3$
Mass	$1/N^3$
Velocity	1
Stress	1
Force	$1/N^2$
Strain	1
Soil density	1
Fluid density	1

The non-dimensional Terzaghi time factor T for consolidation is defined as $\frac{C_v t}{d^2}$.

As $d_p = n d_m$, so $T_m = \frac{1}{n^2} T_p (\frac{C_{vp}}{C_{vm}})$. Cv $= \frac{k}{\mu m_v}$ where k is Darcy permeabilty coefficient

and m_v is compressibility of soil. k and m_v are all related to soil and μ is the pore fluid properties. We know the model using the same soil as prototype, so we can do 'part' of the normalisation using pore fluid viscosity which can bring $\frac{\mu_m}{\mu_p} = m$. So $T_m = \frac{m}{n^2} T_p$.

The relationships are shown below.

Table 2-3 Centrifuge scaling relationship using viscous fluid

Time(diffusion with water)	$1/N^2$
Time (diffusion with viscous fluid)	M/N^2
Fluid viscosity ratio	M
Velocity (water)	N
Viscous fluid velocity (m times viscous than water)	N/M

3 EXPERIMENT EQUIPMENT AND PRINCIPLES

3.1 Centrifuge

The centrifuge used for all the tests is the Acutronic 680-2 geotechnical centrifuge which is a beam centrifuge housed in a 13.5 m diameter chamber with 0.3 meter thick concrete walls. The centrifuge is located in C-CORE on the St. John's campus of Memorial University of Newfoundland. As shown in Figure 3-1 the Acutronic 680-2 geotechnical centrifuge contains a swinging platform on which the models are tested, two parallel steel tubes which support the platform, an adjustable 20.2 tonne counterweight, a central drive box and electrical cabinets, pedestal, gear box, motor and drive. The power of the centrifuge is provided by an AC variable speed motor, with power consumption mainly due to aerodynamic drag within the centrifuge chamber. The radius of the centrifuge is 5.5 m from its axis to the base of the swinging platform. The maximum rotation speed is 189 rpm and the maximum gravity is 200 gravities at a radius of 5 m. The platform can carry a model up to 1.1 m wide by 1.4 m long by 1.2 m to 2.1 m height in the centre of the platform. The maximum payload that the centrifuge platform can carry is 650 kg when the rotational speed is 189 rpm. The centre has a circular concrete chamber and a building containing machine shop, sand raining room, electronics lab, cold room and x-ray facility.

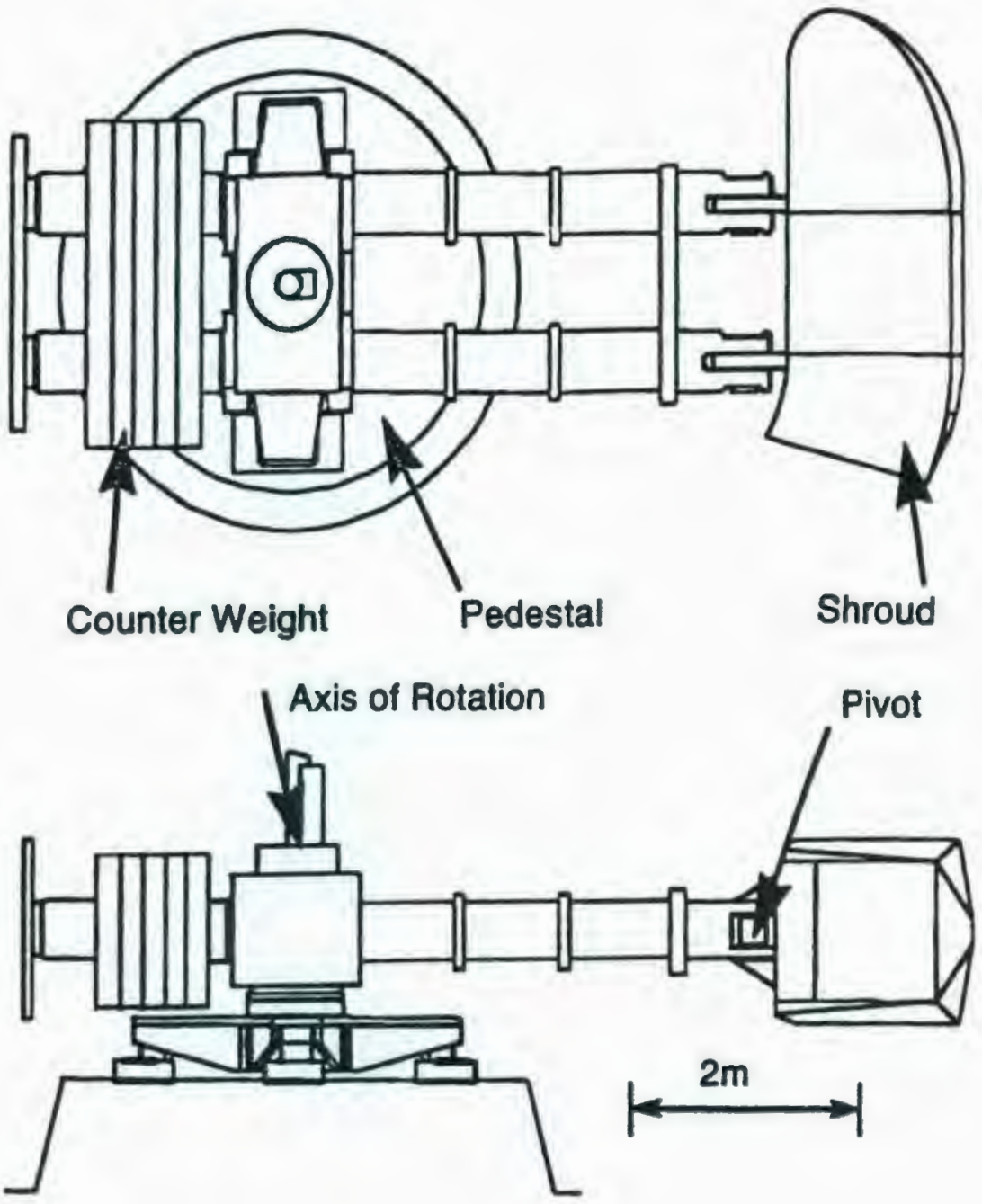

Figure 3-1 Acutronic 680-2 geotechnical centrifuge schematic(C-CORE)

3.2 Strongbox

Centrifuge models use strongboxes to contain the model soil and to provide a base for securing other experimental equipment. After preparing the model in the strongbox, it was carried by a forklift and loaded onto the centrifuge platform for testing.

There are two strongboxes that were used. One box uses acrylic wall box, Figure 3-2, which weighs 213.6 kg when empty. It contains two glass walls through which can be seen the model soil movement during centrifuge testing. The inside dimension of acrylic wall box is 735 mm×275 mm×394 mm. It has channels machined into the base of the strongbox for pore fluid pressure movement. The Acrylic wall box has two valves outside of the box connected to the channels in the base of the box, so the pore fluid supply lines could be connected to both of the valves. For holding the vacuum, the Acrylic wall box has a cover which can be bolted on the top of the box.

The other strongbox is a plane strain box, Figure 3-3. It has one glass wall from which model soil movement during centrifuge testing can be seen. The inside dimensions of Plane strain box is 900 mm×276 mm×294 mm. The empty weight without protective glass is 304.4 kg.

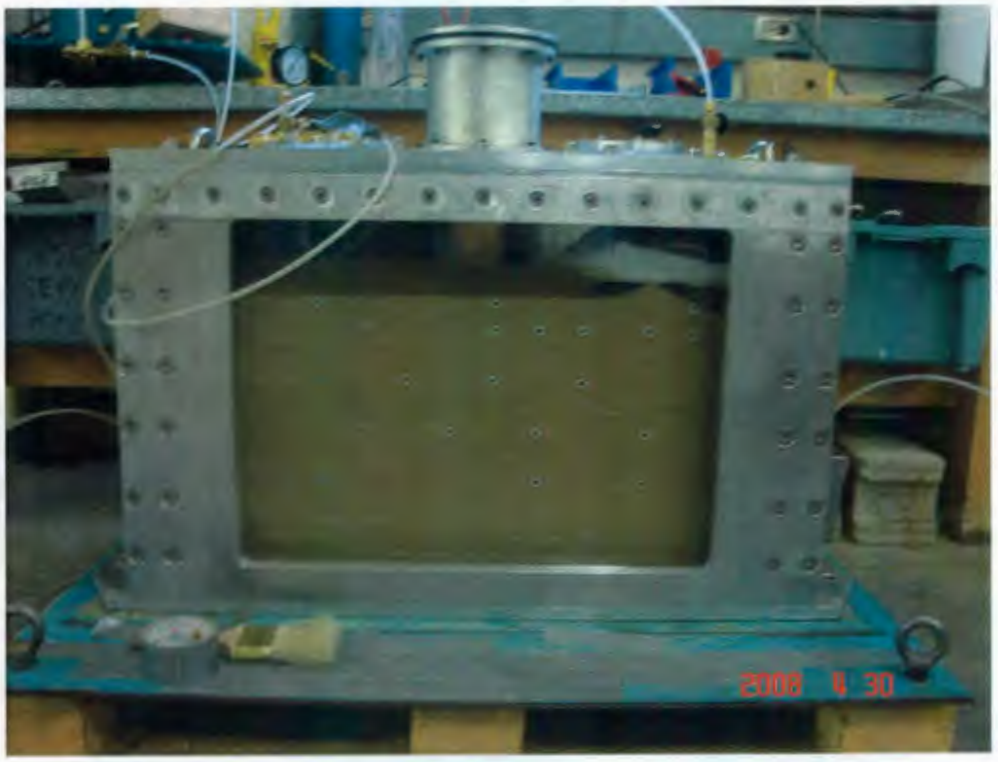

Figure 3-2 Acrylic wall box

Figure 3-3 Plane strain box

Channels are also machined into the base of the strongbox. This box has only one valve on the back of the box. The strain box also has a cover for holding the vacuum which can be bolted on the top of the box and sealed up with Vaseline.

3.3 Model Ice Keel

The test setup consisted of an aluminum half width ice keel model mounted on a gantry situated on top of the containment box because the centerline of the model was replaced by a viewing window to visualize the subgouge deformation accumulation. The model ice keel is made of aluminum plate that is welded together. The attack face which meets the sand is knurled to increase the interface friction above the angle of the internal friction of the sand. There are two kinds of model ice keels used in the test. P02, P03, P05, P06, P07, P08 are using the model ice keel with an attack angle of 30 degrees from the sand level. The width of the model ice keel is 90 mm. P09 is using the model ice keel with attack angle of 15 degrees. The width of the model ice keel is 100 mm. The dimension of these two model ice keels is shown in Figure 3-4 in which all the dimensions are in mm.

In order to measure the vertical load and horizontal load, there are load cells between the model ice keel and the carriage and motor respectively. Three 2.2 kN and 4.4 kN tension/compression load cells are attached to the ice keel and the carriage, which can measure the vertical load. The location of the load cells is shown in Figure 3-5 There is one 4.4 kN tension/compression load cell attached to the front of the model ice keel which is used for measuring the horizontal load by connected to the motor through the steel cables.

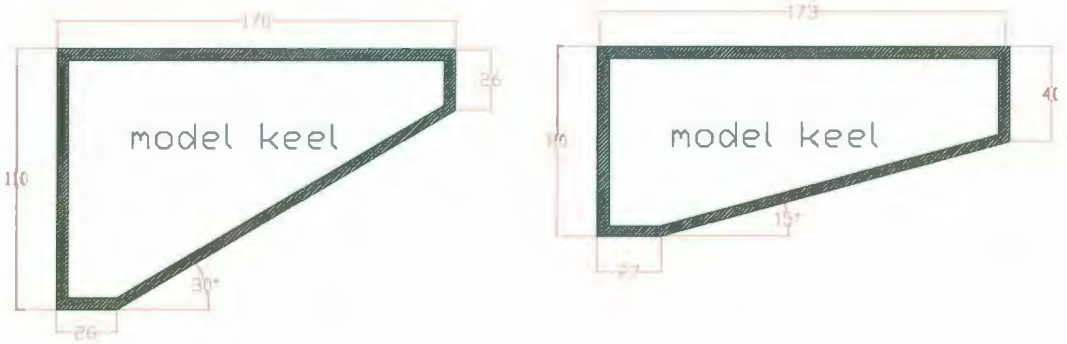

Figure 3-4 Dimensions of these two model ice keels in mm.

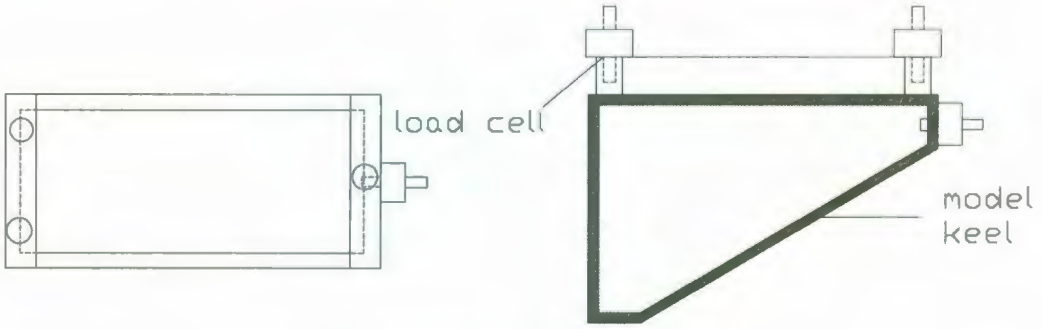

Figure 3-5 Location of the load cells

3.4 Actuator

The actuator holds the carriage on which is bolted the model keel. It is bolted on the top of the strongbox. The actuator is designed to provide the horizontal motive force and to resist vertical motion, Figure 3-6. There are two parallel steel bars on the top of the actuator for guiding the movement. Four bearings, two on each steel bar are bolted together through two steel plates. The bearings can slide on the bars with small friction resistant which can be ignored compared with the horizontal force and the vertical force that expected during the centrifuge test. A motor is connected to a drive shaft and capstan connected to the model keel by steel cables. The model ice keel movement is transmitted through the steel cables by the motor. The moving speed of the model ice keel is

controlled by the speed of the motor adjusted by the computer in the control room. There is a limit switch at the end of the actuator. When the bearings touch the switch, the motor stops running and the model ice keel stops moving.

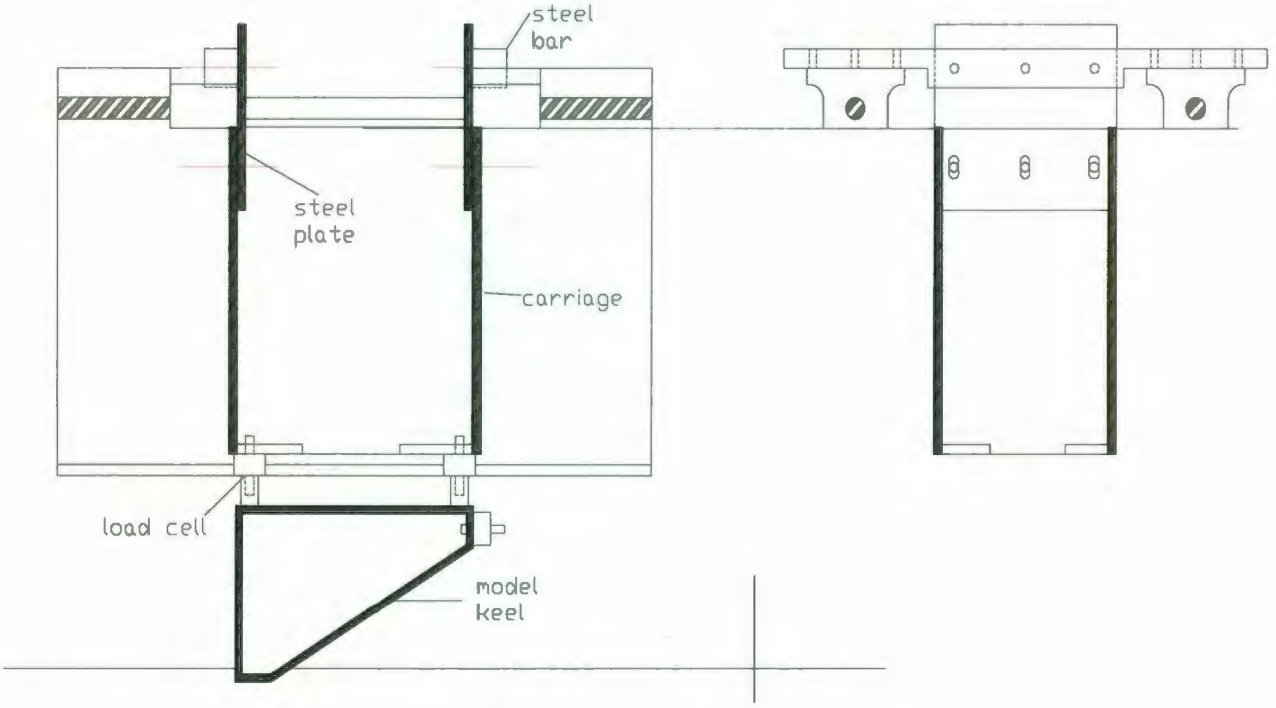

Figure 3-6 Actuator side view

3.5 Data Aquisition System

Data aquisition system contains a signal conditioning box, a string potentiometer, LVDT's, four load cells, and two cameras. The string potentiometer was placed at the end of the actuator and connected to the carriage which is used to get the displacement of the model ice keel. During centrifuge testing, because of the increased g level, the model sand will compress and become denser. So the sand level will be reduced. LVDT'S are located on the side of the actuator and stand on a plastic bearing plate on the top of the sand to measure the settlement of the sand level, Figure 3-7 After centrifuge test, the sand

density can be calculated by the original sand level measured after loading the model on the centrifuge platform minus the settlement during test. Cameras are used to take pictures of the sand through the model ice keel moving process. The pictures are analyzed by PIV method to assess the subsurface sand movement during gouge modeling. The signal conditioning box is located on the side of the strongbox. All the measuring equipment are connected to the signal conditioning box. The data is transferred through signal conditioning box to the computer. The centrifuge acquisition and control systems are contained in the centrifuge electrical cabinets.

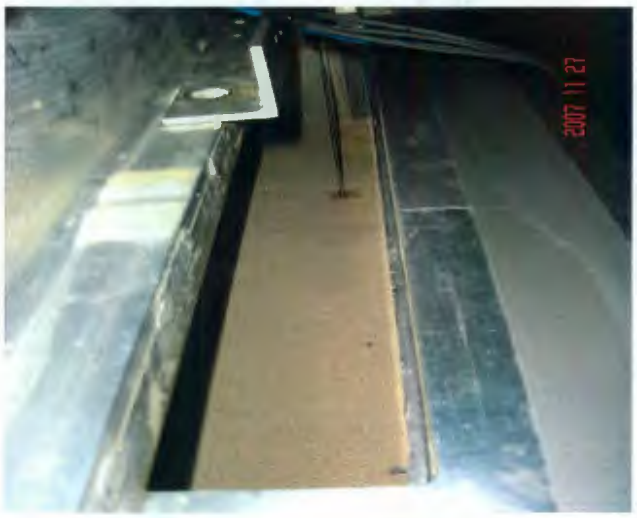

Figure 3-7 LVDT'S location

4 EXPERIMENT PROGRAM AND TECHNIQUES

4.1 Introduction

A series of seven centrifuge model gouge tests were performed and the subgouge deformation accumulations were tracked using particle image velocimetry, PIV techniques adopted by White et al. (2003). The soil consisted of AlWhite Silica sand. The characteristics of the soil are presented in section 4.2, while the experimental planning and identification are described in section 4.3. Centrifuge tests at a scale of N g's were conducted on viscous pore fluid-saturated models to retard excess pore pressure dissipation. This fluid is a solution of a water-soluble polymer derived from cellulose diluted to M times the viscosity of water, see Table 2-3. The procedure for sample preparation, the placement of transducers and saturation are presented in detail in section 4.4. Section 4.5 discusses the model instrumentation and data acquisition. The centrifuge testing procedure is discussed in section 4.6. Section 4.7 presents the particle image velocimetry, PIV techniques.

4.2 Sand Description

Alwhite Silica sand #00 was used in all tests. Classification tests to determine material properties for Allwhite Silica sand were conducted according to ASTM specifications. The sand corresponding index properties and classification are reproduced in Table 4-1.

Table 4-1 Index properties and classification of tested sand

Maximum dry density	15.84 g/ cm^3
Minimum dry density	12.94 g/ cm^3
Specific Gravity	2.66
Effective gravity size (d_{10})	0.1 mm
Mean grain size (d_{50})	0.3 mm
Uniformity coefficient (C_u)	3.2
Coefficient of gradation(C_c)	1.25
USCS Group	SP-SM

4.3 Testing Program

A total of seven tests were conducted in the centrifuge, Table 2-1. Centrifuge tests were performed under drained to undrained conditions using half width models and a viscous fluid of a viscosity 30 cSt (P05, P06, P07, P08 and P09). The first model test P02 was conducted in dry dense sand to prove the new equipment and techniques. The second model test P03 was conducted relatively slowly in water saturated medium sand. Two tests P05 and P08 were included for comparisons to previous Delft Hydraulics flume medium scale gouge tests, Appendix A. Three tests P07, P08 and P09 were conducted with a faster gouge rates using a viscous pore fluid.

4.4 Preparation of Soil Model

The model test bed was rained dry into the centrifuge strongbox from a hopper. The raining technique consists of pouring dry soil layers through a fixed drop height. Raining

can be achieved by using stationary or traveling hoppers. The traveling raining technique is used in this study to control the density of sand over a wide range from a loose state to a dense one in a stable manner.

Figure 4-1 Setup of the sand raining tool

The hopper shown in Figure 4-1 was manually moved back and forth over the area of sample preparation. The relative density of the soil was controlled by the falling height of the sand and travelling speed of the hopper. Sand pouring is done in thin layers by raising the hopper the same thickness of layer to obtain a constant height of raining for each layer. A 100 mm thick layer of coarse sand with particle size larger than 1mm was placed before raining the sand to distribute the fluid throughout the sample during saturation as shown in Figure 4-2. The drainage layer was covered with a geotextile layer. The initial

soil sand mound as shown in Figure 4-4 is prepared after reaching the final sand level. The total weight of the dry soil is tracked.

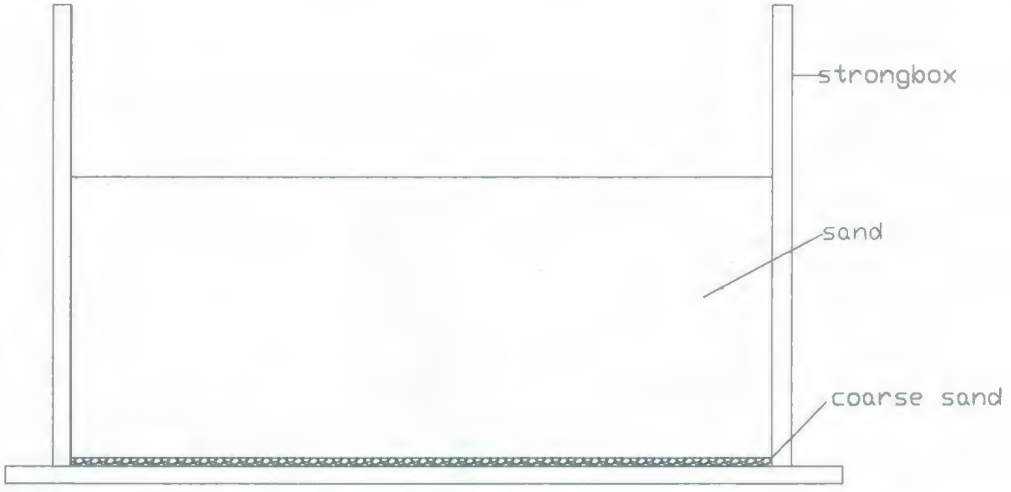

Figure 4-2 Model configuration

Hydroxypropyl methylcellulose (HPMC) was prepared by mixing Methocel F50 Powder at a specific concentration with de-ionized water to reach the required viscosity (say 30 cSt). A mass of Benzoic Acid USP powder equal to approximately 1% of the mass of the HPMC powder is added to the mixture to prevent any bacterial growth that may occur in the completed fluid batch. After that, the pore fluid reservoir is de-aired for 48 hours.

Figure 4-3 and Figure 4-5 show the configuration of the sample container, vacuum pump, and fluid tank. The sample is first de-aired by the application of vacuum to the prepared sand for a period of approximately 48 hours at about 70 kPa. Following this initial vacuum stage the vacuum pump to the sealed model container is shut off and carbon dioxide is then used to displace the less soluble air that may be present in the voids of the

sand model. Carbon dioxide gas is introduced slowly into the bottom of the model under atmospheric pressure. Following this process, the strongbox is again placed under vacuum to bring it back to the 70 kPa vacuum level. The process of introducing carbon dioxide followed by vacuum is repeated four times to ensure that the majority of the gas inside the container is carbon dioxide which is much more soluble in water than air to allow a more complete saturation. The next step is to open the vacuum to both the de-aired pore fluid tank and the strongbox to ensure equal vacuum to both containers so that when fluid is introduced it is not moving by differential pressure that can cause disturbance to the model. After equalizing the vacuum between the two containers, a valve is opened to allow the pore fluid to saturate the model from the bottom. It usually takes 3 days to saturate the sand in the box from the bottom to the top.

4.5 Model Instrumentaion and Data Acquisition

Data acquired during the gouging event included the resultant vertical and horizontal forces acting on the model keel. The total vertical force was computed through summation of contributions from the three individual 2.2 kN and 4.4 kN tension/compression load cells (front, close and far load cells) which linked the model keel to the carriage assembly. The horizontal force is determined by measuring the tension in the cable via a 4.4 kN water-resistant tension/compression load cell. The model keel displacement is measured via a positions transducer while differentiating displacement with time gives gouging rate. Settlement of the seabed surface was monitored with one linear variable displacement transducer (LVDT). In test P09 a total of three pore water pressure transducers (PPTs) were embedded in the model seabed.

Figure 4-3 Configuration of the sample container during saturation process

Figure 4-4 The initial sand mound

Digital photography by a CCD photographic camera or a high speed Phantom camera is used to capture images of soil deformation during ice gouging. There were two additional cameras mounted on the package to monitor the progress of the test and cable movement.

The data acquisition-sampling rate during centrifuge spin-up was set at 10 Hz and during ice-gouging event was set at 10-500 Hz based on the keel speed.

Data acquisition is performed using a PC-based data acquisition system. Transducer excitation voltage and filtering are provided using a custom-designed signal conditioning system. Transducer signals are digitized through a 64-channel data acquisition system contained in a VXI chassis and collected using a Windows-based data acquisition program called DaqExpress.

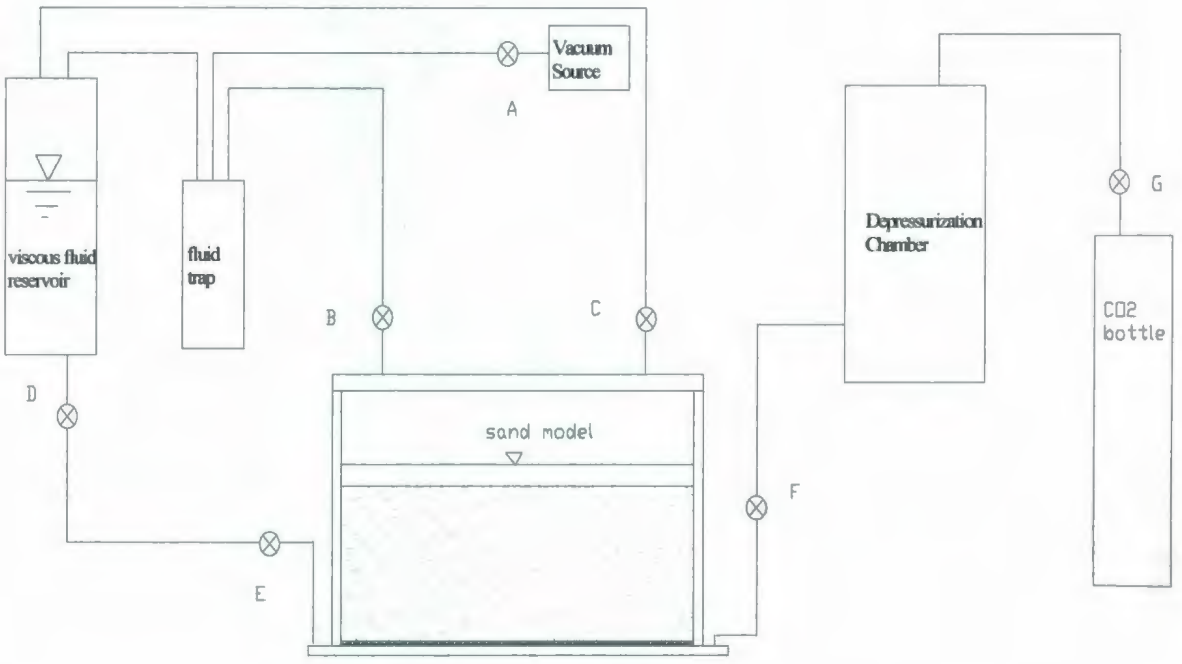

Figure 4-5 Model saturation system

4.6 Centrifuge Testing Procedure

A centrifuge proof test was undertaken to evaluate the performance of the drive system. Once saturation is complete, the actuator was put on the strongbox as well as other apparatus, including camera mounts, CCD cameras, signal conditioning (S/C) box and LVDT. The test package was carefully moved to the centrifuge arm and spun up to 42 rpm to check the centrifuge and model response. The centrifuge was then spun up to the specified test acceleration level at the base of the model keel. After the gouge process, the centrifuge was decelerated and then stopped. Following inspection and photographs of the model testbed, the model test package was removed from the centrifuge chamber.

4.7 Particle Image Velocimetry

Particle image velocimetry (PIV) is an image analysis tool that can be used to measure soil deformations with considerable precision. Combined with high-resolution digital images, PIV software is able to utilize an autocorrelation function and bi-cubic interpolation to track the movements of patches of pixels between two images and return deformation measurements to a fraction of a pixel. PIV tracks the movement of patches of pixels between digital photographs taken from a stationary camera at a set time interval. Digital images are matrices that provide a brightness value for each pixel. In a colour photograph a pixel is assigned three brightness values ranging from 0 to 255, one for each of the three colour channels, whereas pixels in a monochromatic image will be assigned a single brightness value, White et al.(2003). The contrast between adjacent pixels is proportional to the difference between their respective

brightness values. A square patch of pixels is selected from the first image and PIV searches for it in the second image. The Fast Fourier Transform is applied to the patches in order to approximate the brightness matrix with a function of sine and cosine to that the autocorrelation function can be used to compare patches in the two images, Renawi (2004). The patch location in the second image is shifted about a predetermined search area and the pixels are compared to the patch in the first image. The autocorrelation function returns a planar surface that represents the degree of compatibility between the two patches being compared. These planar surfaces, each one a square pixel, form the surface shown in Figure 4-6. A distinctive peak in the figure indicates the location of greatest compatibility between the original patch and one in the second image, White et al. (2003).

This method can determine the displacement of the patch to a fraction of a pixel by fitting a bi-cubic interpolation to the very top of the peak returned by the autocorrelation function as shown in Figure 4-6 The resolution of the bi-cubic interpolation determines the resolution of the displacement vector. If the bi-cubic interpolation is evaluated at $1/200^{th}$ of a pixel, the displacement vector will have a resolution of 0.005 pixels. Higher resolutions require more computing power and other sources of error generally render a resolution much higher than 0.005 pixels unnecessary, White et al.(2003).

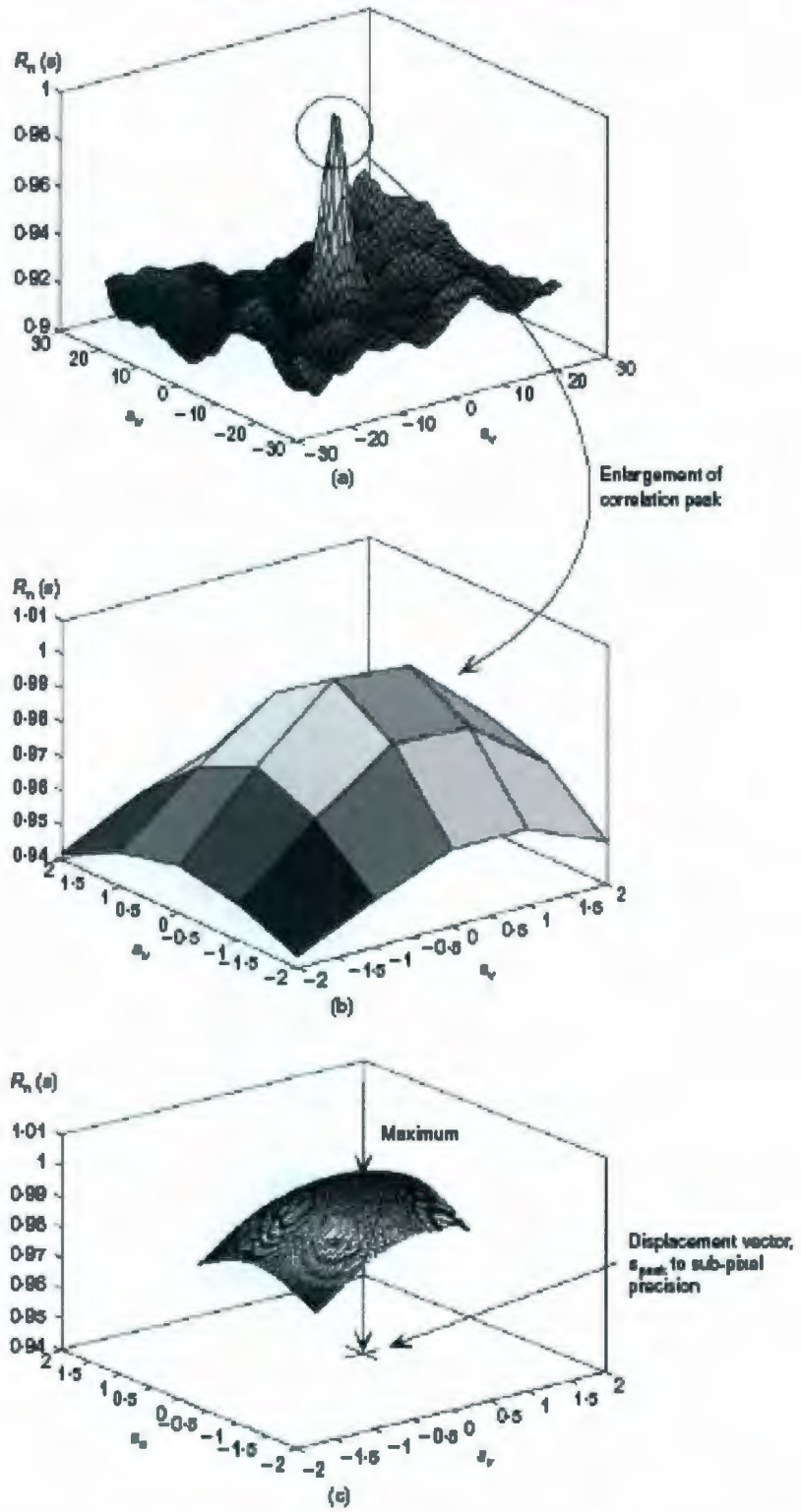

Figure 4-6 Autocorrelation function and bi-cubic approximation being used to determine the displacement of a patch, White et al.(2003)

The centerline of the model was replaced by a viewing window to visualize the subgouge deformation accumulation using PIV techniques. The photographic reference field used consists of at least fourteen 6mm diameter black dots shown in Figure 4-7 provided a reference field of known object-space coordinates while knowing the image and the object-space locations of each dot, the optimal photogrammetric transformation parameters can be found. The camera is placed at a distance from the viewing window. The subgouge deformation movements were tracked through a successive series of digital images captured by a CCD photographic camera for tests P02 to P06 at about 0.2 frame/sec. For high speed tests, a high speed Phantom camera was used for tests P07, P08 and P09 at up to 300 frames/sec. This technique has been used successfully for all tests.

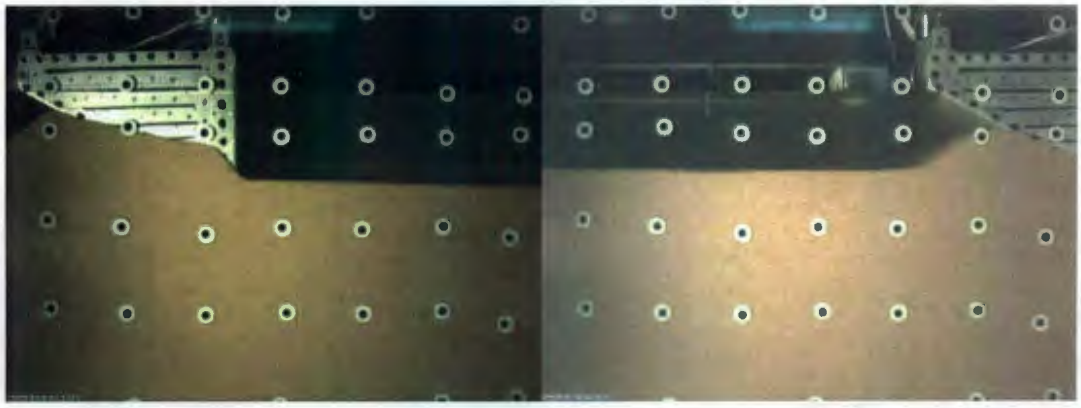

Figure 4-7 Centrifuge model test of ice gouging with photographic reference field at test start and end

5 EXPERIMENTAL RESULTS

5.1 Introduction

This chapter discusses the experimental results of the behaviour of saturated sand subjected to ice-gouge loading under drained to undrained conditions. The studied soils consisted of Alwhite Silica sand #00. Its characteristics were presented in section 4.2. In the study of the ice-gouge problem where excess pore pressure dissipation will occur during the dynamic event, it is necessary to increase the model consolidation time so that it is more compatible with the inertial time by using a viscous fluid with the same water density.

A total of seven tests were conducted in the centrifuge, Table 2-1. The parameters are different between the seven conducted tests. The significance of parameters such as attack angle α = 15 and 30 degrees, width/depth ratio of 6 up to 13, gouge depth Ds = 0.2 to 2.4m, keel speed from 0.5 to 55 mm/sec and soil conditions were examined. Two tests P05 and P08 were included for comparisons to previous Delft Hydraulics flume medium scale gouge tests, table A 4. Three tests P07, P08 and P09 were conducted with a faster gouge rates using a viscous pore fluid. All the first six tests were conducted using a keel with an attack angle of 30° however the attack angle for the last test, P09 was using the model ice keel with attack angle of 15°.

Centrifuge tests were performed at different centrifugal accelerations on scaled pore fluid-saturated models as shown in Table 2-1. Responses such as vertical and horizontal loads, particle deformations, and pore pressure (in test P09) were examined throughout the tests. The Particle Image Velocimetry (PIV) technique was used to track small patches of soil texture through a successive series of digital images captured by a CCD photographic camera for tests P02 to P06 at about 5 second intervals (0.2 frame/sec) or high speed Phantom camera when required for high speed tests P07, P08 and P09 at up to 300 frame/sec.

5.2 Experimental Load Data Analysis

The centerline of the model was replaced by a viewing window to visualize the subgouge deformation accumulation. The test were using an aluminum half width ice keel. For measuring half model vertical load, three load sells as shown in Figure 5-1 below were used to link the carriage and the model ice keel. The vertical load is obtained by adding the data from the three individual load cells. The vertical load versus keel displacement are shown in Figure 5-2 to Figure 5-8 which show that the three load sells have different vertical loads. The far load cell usually has higher readings than the other load cells, which is due to excess surcharge load from the lateral soil mound formed near the far cell. The maximum vertical load expressed in prototype scale varies from 0.14 KN to 65.2 KN.

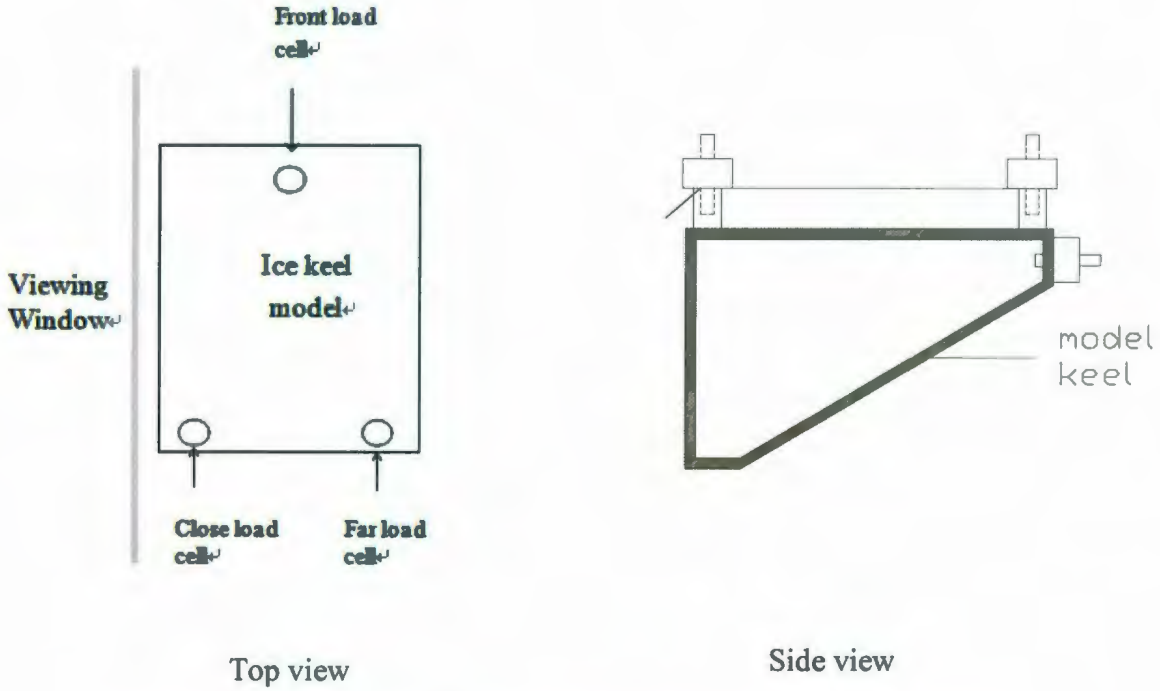

Top view

Side view

Figure 5-1 Top view and side view of vertical Load Cells arrangement

Vertical and horizontal forces data were acquired during the gouging event. Figure 5-2 to Figure 5-8 shows the model half forces with keel movement for all tests. It may be observed from all test data that both horizontal and vertical loads increased rapidly as the keel started to move until a cyclic steady state condition develops. The keel resistance developed a steady state after about 100-150mm of keel model displacement in all tests, Figure 5-9 to Figure 5-15. The gouge force increases are associated with the growth of the frontal berm. Figure 5-15 shows an example of gouge forces for P09. The arrows are the selected keel position in Figure 5-30 to Figure 5-32 showing the development of the frontal berm. The frame number versus keel displacement is presented from Figure A. 30 to Figure A. 36. Table 5-1 shows prototype maximum loads at steady state conditions for all seven tests. The steady state prototype gouging horizontal forces were in the range of

7.7 MN to 47.0 MN except for the two shallow gougeing tests P05 and P08 that showed much less forces, Table 5-1.

The horizontal load and vertical load versus keel displacement for each gouge event presented in Figure 5-9 to Figure 5-15 show that the cyclic variation present in vertical load is also apparent in the horizontal load at the same displacement. The total vertical load represents the summation of the three load cells attached to the model ice keel and carriage.

Figure A. 1 to Figure A. 6 in Appendix A show the ratio between vertical load and horizontal load for each gouge event. The ratio is from 1.15 to 1.5 during steady state (after about 100-150 mm of keel model displacement in all tests) for the entire tests except dense dry sand test P02 which ratio between vertical load and horizontal load is 3.15.

Table 5-1 Sand test results in prototype parameters

Test I.D.	Attack angle, α (deg)	W/Ds	Speed (mm/sec)	Maximum Fv, MN during steady state	Maximum Fh, MN during steady state	Average Fv/Fh during steady state
P02	30	7.6	0.5	25.3	8.0	3.15
P03	30	7.0	0.5	9.9	7.7	1.28
P05	30	12	1.1	0.14	0.095	1.5
P06	30	6.25	1.1	65.2	47.0	1.39
P07	30	5.96	5.5	52.5	45.4	1.28
P08	30	11.3	54.6	0.45	0.32	1.3
P09	15	13.3	56.8	32.4	28.2	1.15

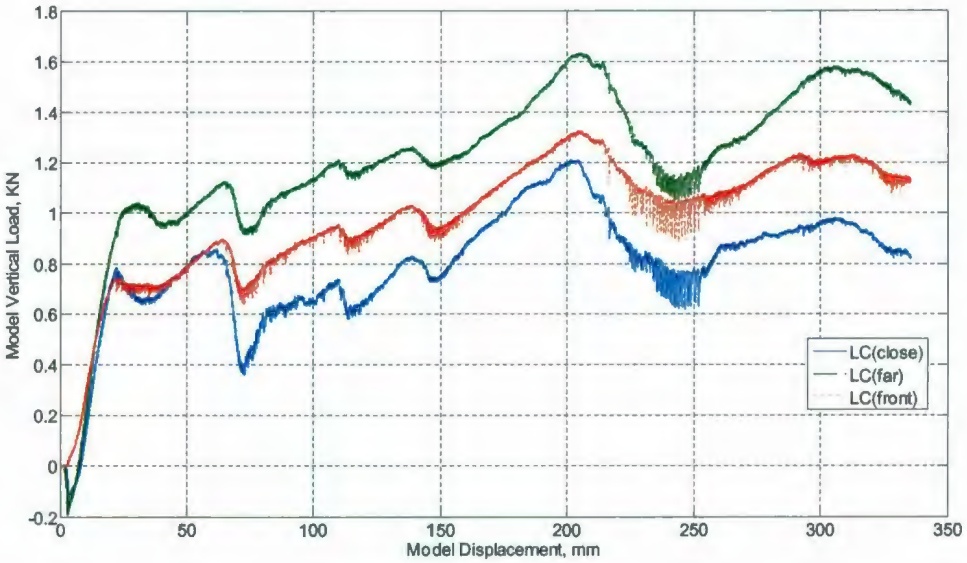

Figure 5-2 Model vertical load versus ice keel displacement for test P02

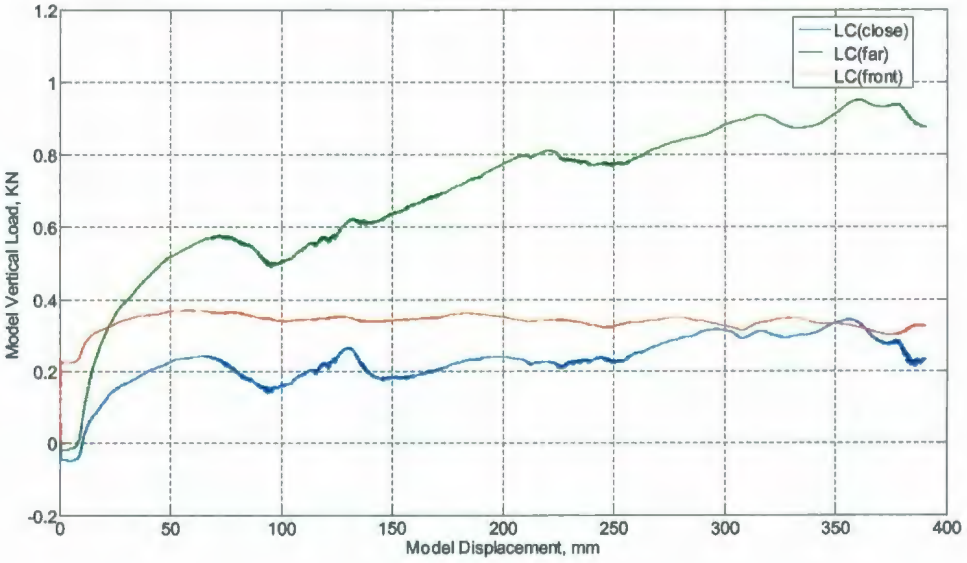

Figure 5-3 Model vertical load versus ice keel displacement for test P03

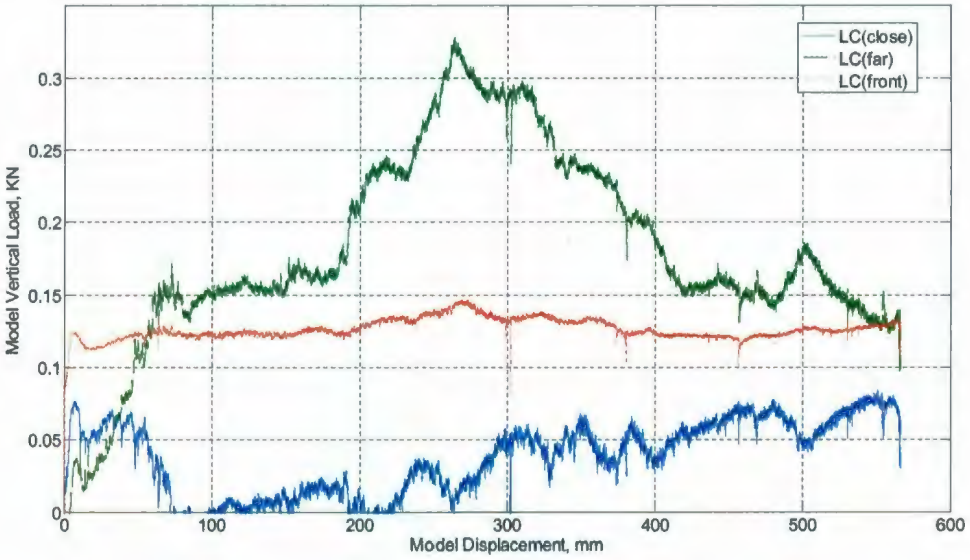

Figure 5-4 Model vertical load versus ice keel displacement for test P05

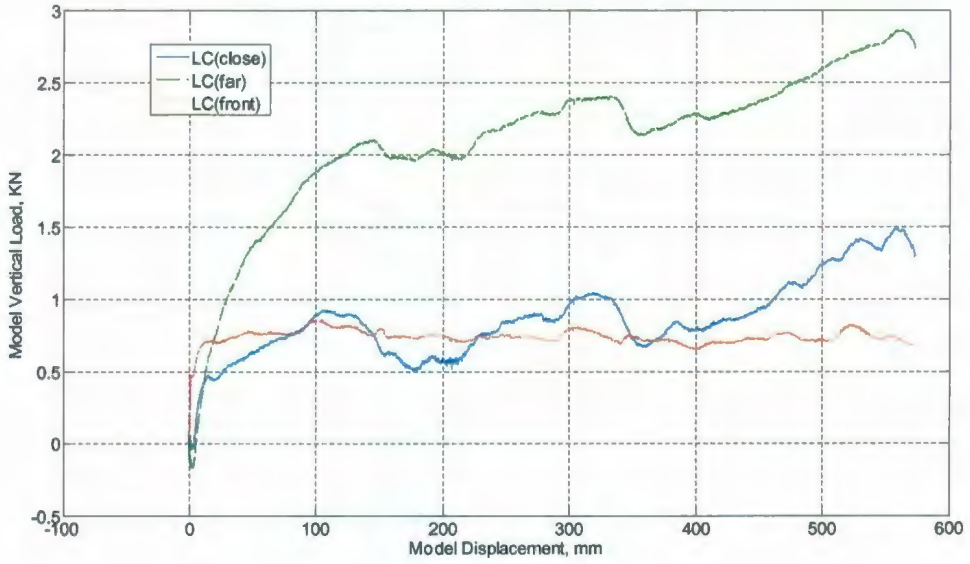

Figure 5-5 Model vertical load versus ice keel displacement for test P06

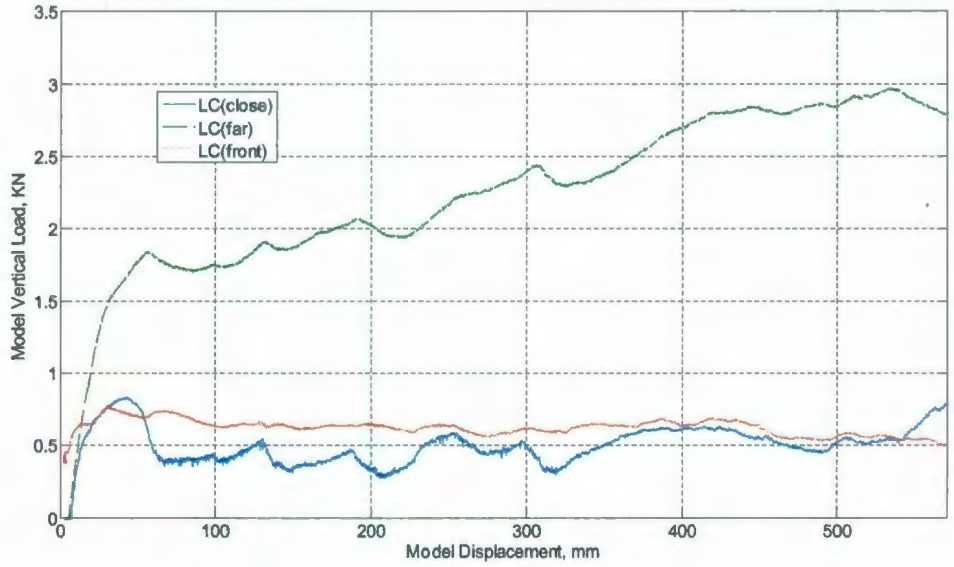

Figure 5-6 Model vertical load versus ice keel displacement for test P07

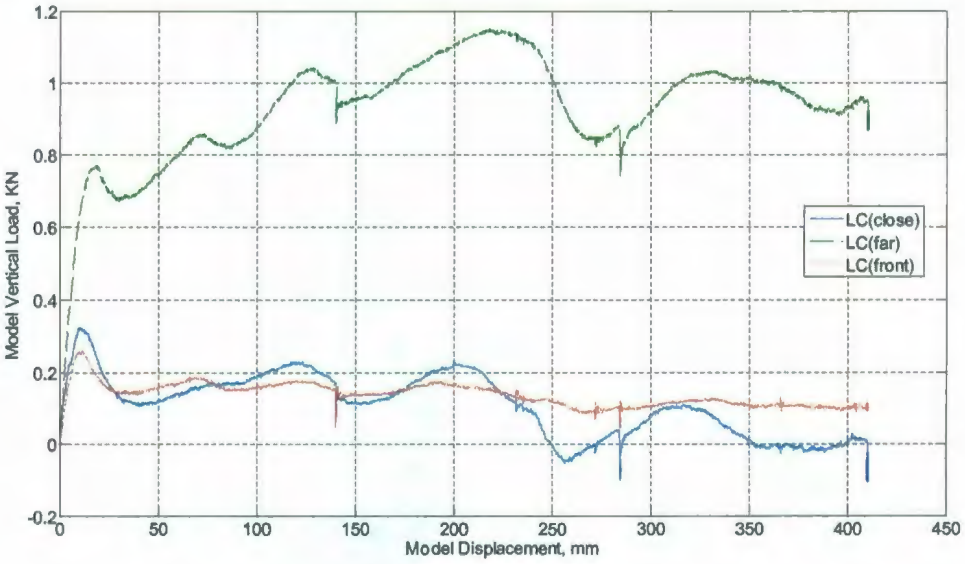

Figure 5-7 Model vertical load versus ice keel displacement for test P08

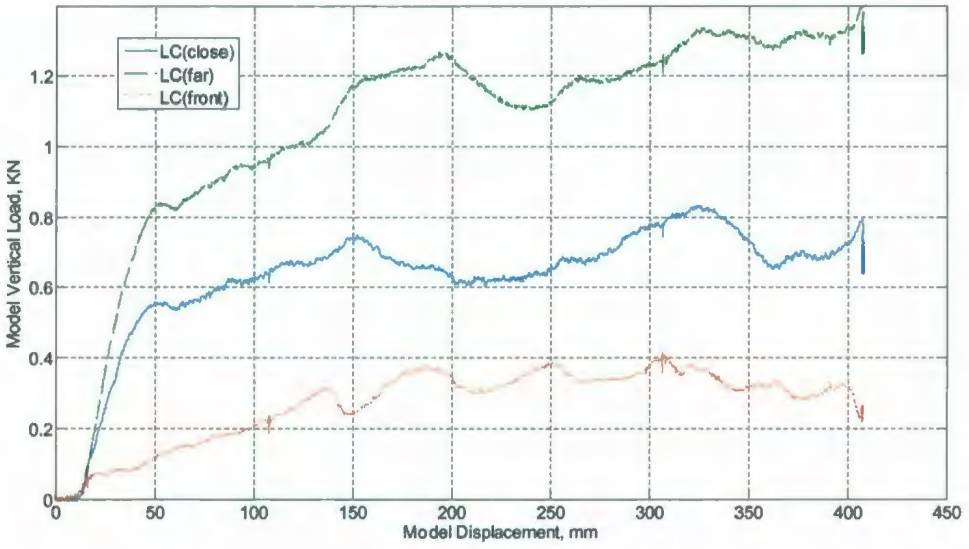

Figure 5-8 Model vertical load versus ice keel displacement for test P09

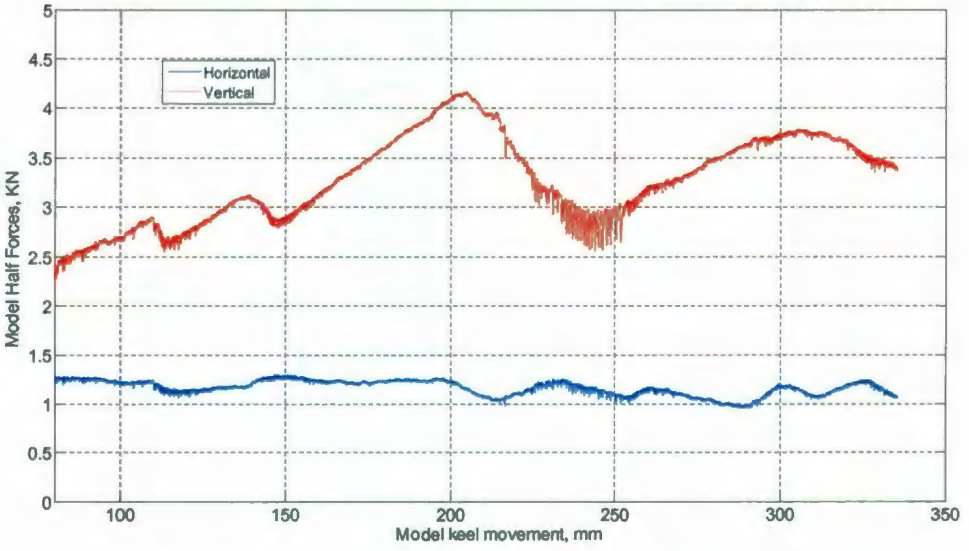

Figure 5-9 Model total vertical and horizontal loads versus ice keel displacement for test P02

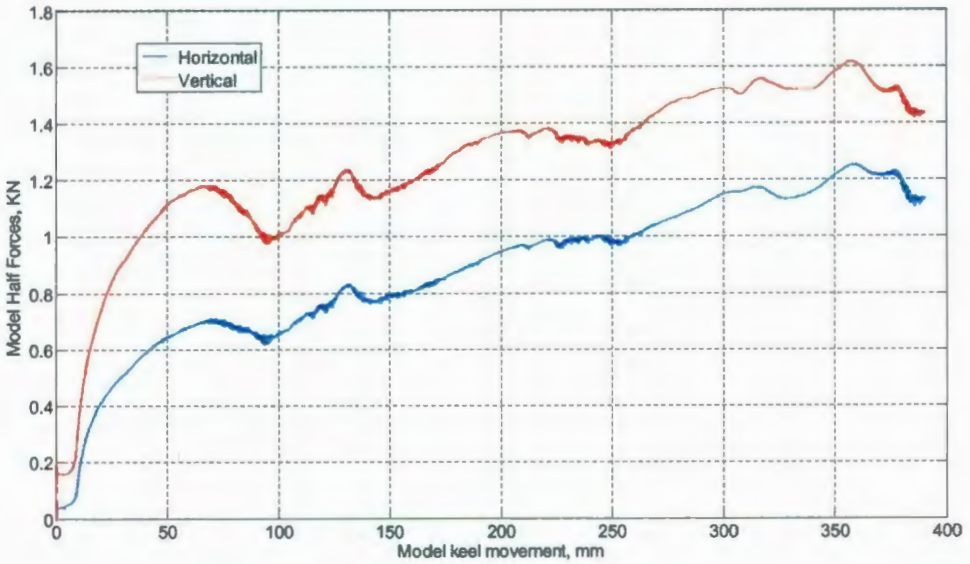

Figure 5-10 Model total vertical and horizontal loads versus ice keel displacement for test P03

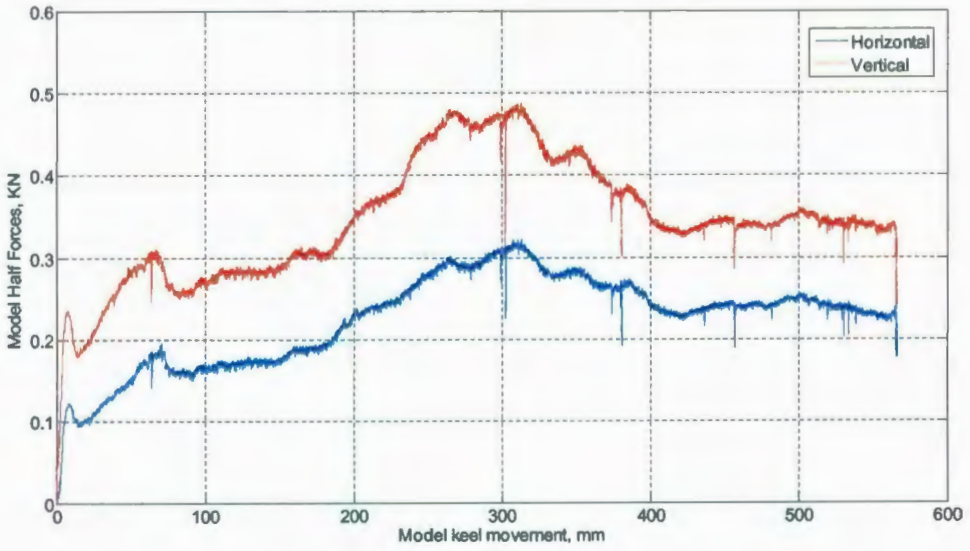

Figure 5-11 Model total vertical and horizontal loads versus ice keel displacement for test P05

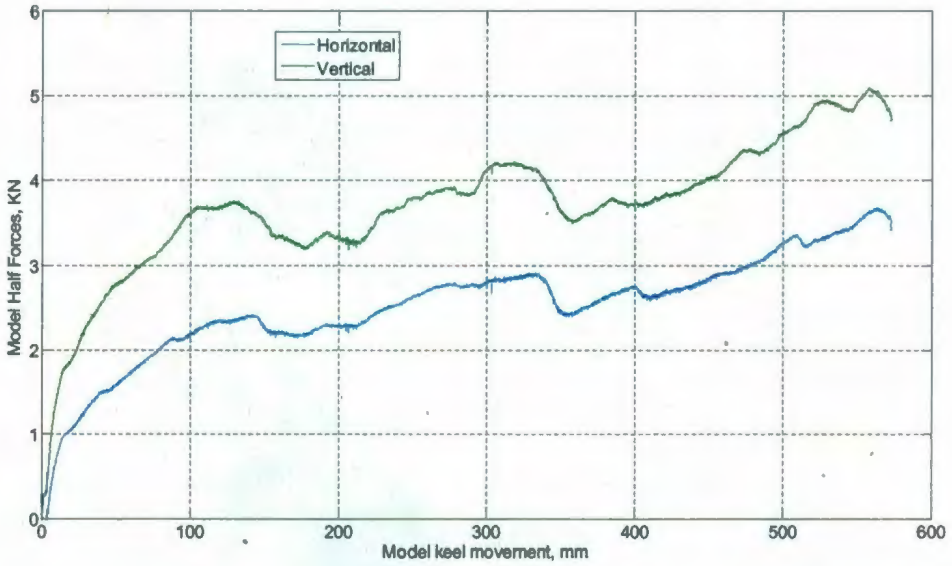

Figure 5-12 Model total vertical and horizontal loads versus ice keel displacement for test P06

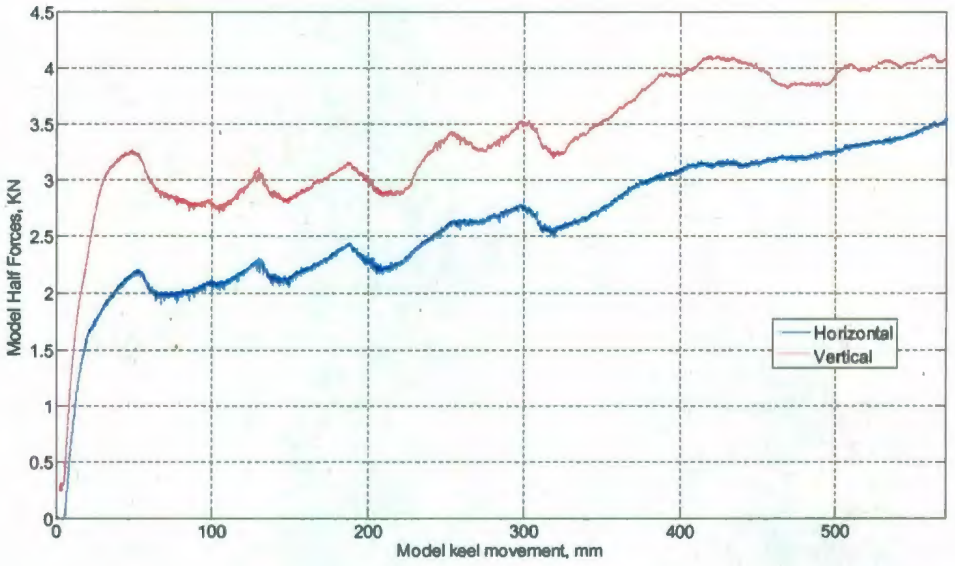

Figure 5-13 Model total vertical and horizontal loads versus ice keel displacement for test P07

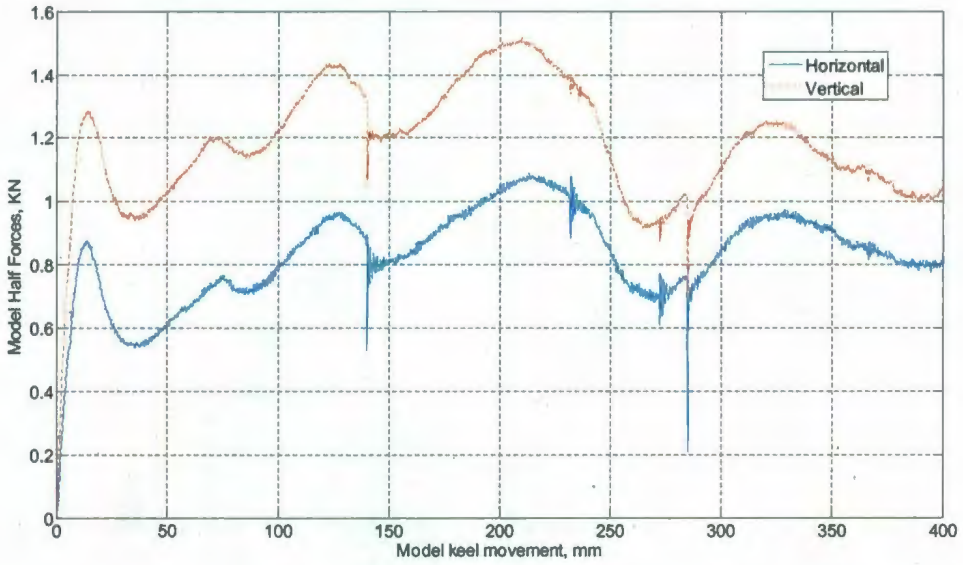

Figure 5-14 Model total vertical and horizontal loads versus ice keel displacement for test P08

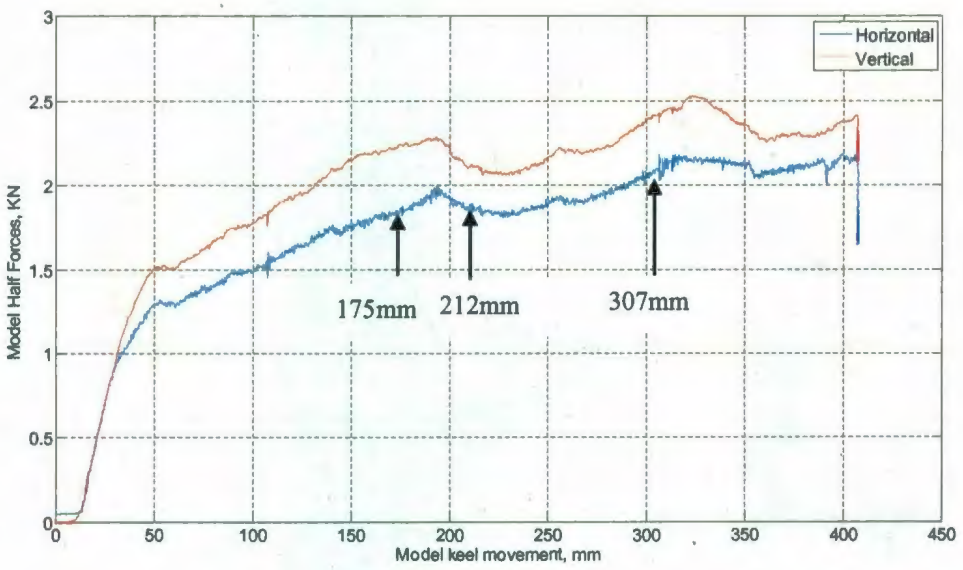

Figure 5-15 Model total vertical and horizontal loads versus ice keel displacement for test P09

5.3 Subgouge Deformation

The subgouge deformations of a series of seven centrifuge tests were tracked using Particle Image Velocimetry (PIV techniques) adopted by White et al. (2003). The PIV technique can track well as low as 0.2mm displacements below the keel. As the model ice keel is driven in the sand, the soil reaction force increase and cause the development of a deep seated bearing failure mechanism. As the keel advances, this mechanism is overridden and the load decrease corresponds with the clearing process. This cyclic process continues with continued displacement. These load cycles have been correlated in all tests to the failure mechanism.

Figure 5-16 shows the forces and maximum horizontal deformation with keel movement. The maximum horizontal deformation is also seen to be cyclic in nature. The peaks in the horizontal deformation curve (A', B') correspond to the peaks in the load curve (A, B) with a 120mm geometric offset which means that the maximum horizontal deformations are 120mm ahead of the basal corner of the keel where load resistance were measured. (A maxima in forces associated A' maximum in SGD accumulation). Figure 5-30 to Figure 5-32 shows the clear three failure surface at different stage of keel movement for test P09. Figure 5-18 to Figure 5-29 shows some of the selected subgouge deformation fields for the other conducted tests. The units are in mm, and the deformation vectors are magnified by 10-20.

Figure 5-33 to Figure 5-39 show the maximum horizontal subgouge displacement at different keel positions. Comparing Figure 5-33 to Figure 5-39, the maximum horizontal

subgouge deformation usually appears under the final position of the keel base. Figure 5-40 to Figure 5-46 present the form of the subgouge displacement. The distance x represent the distance from the right side of the box to the keel. Large displacements occurred at the base of the keel decreasing with depth.

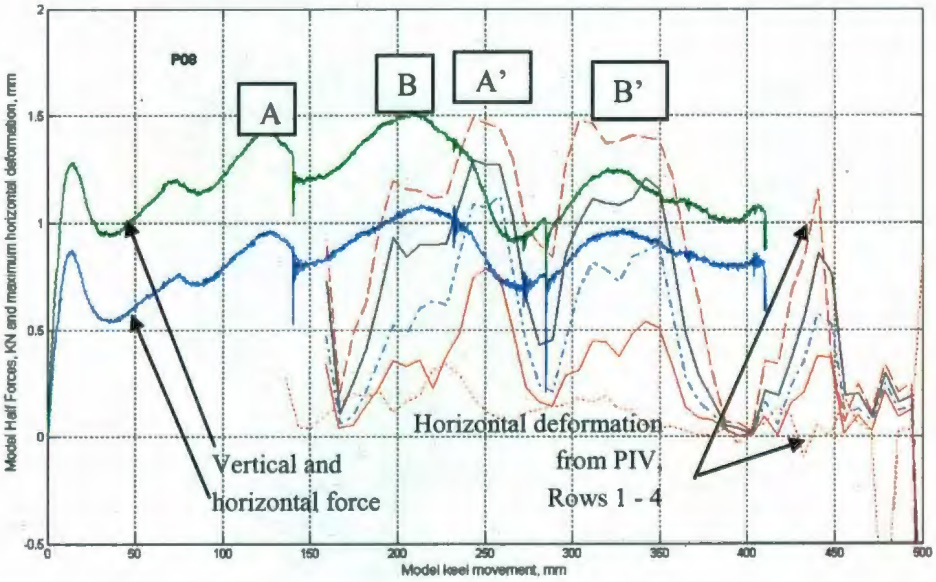

Figure 5-16 Forces and horizontal deformation accumulation with keel movement for P08

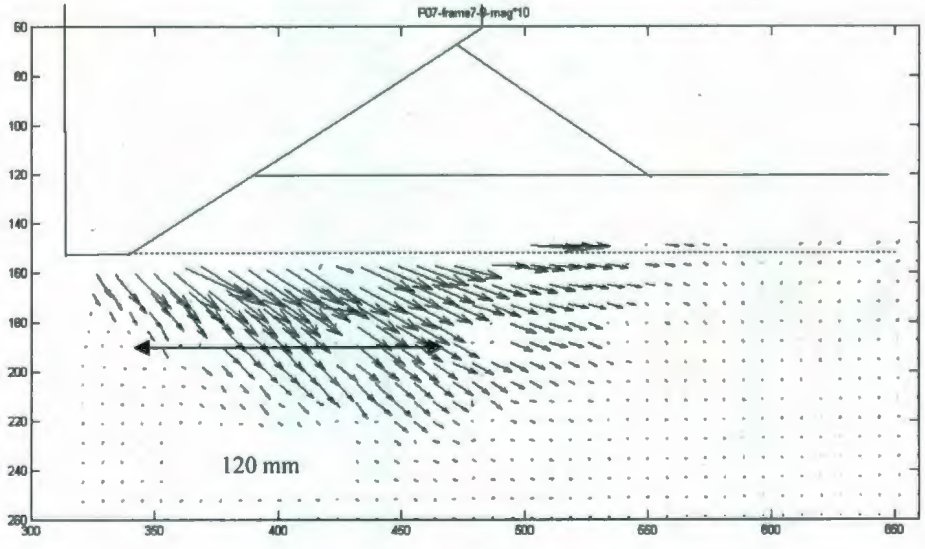

Figure 5-17 Tyoical SGD accumulation ahead of basal keel corner

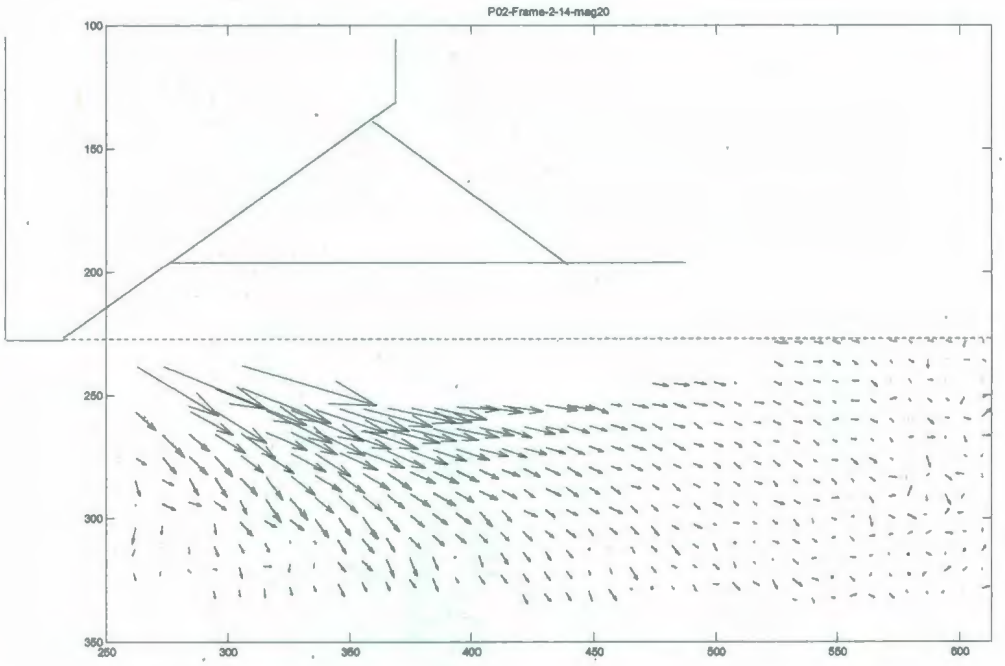

Figure 5-18 PIV subgouge deformation for frame 2-14, displacement of 67.5 mm, Magnification x10, P02

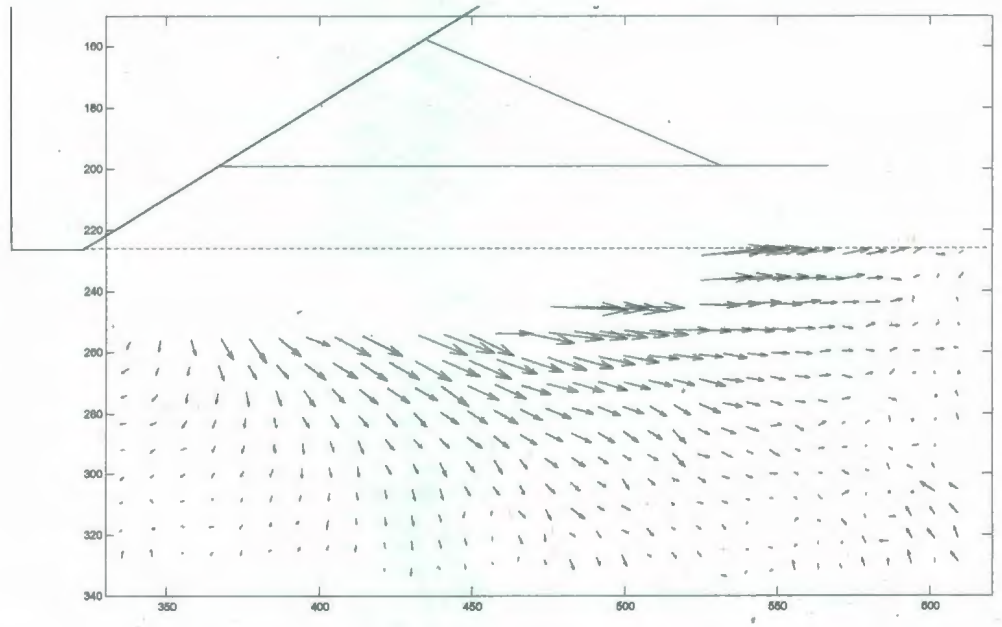

Figure 5-19 PIV subgouge deformation for frame 26-32, displacement of 154.2 mm, Magnification x10, P02

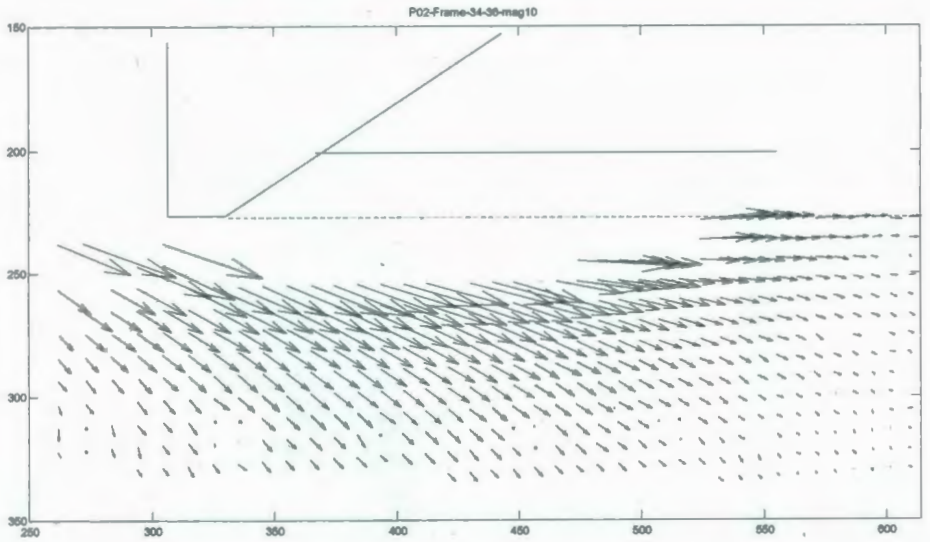

Figure 5-20 PIV subgouge deformation for frame 34-36, displacement of 173.5 mm, Magnification x10, P02

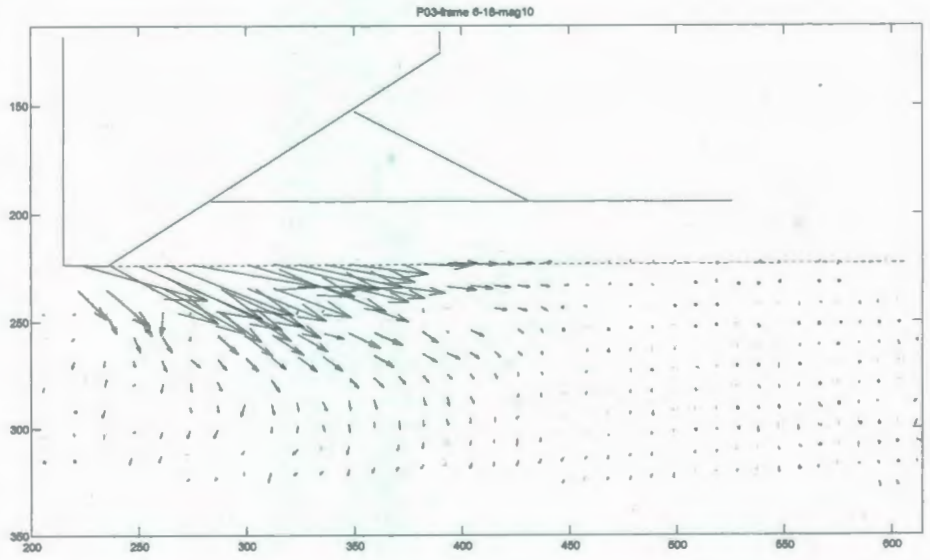

Figure 5-21 PIV subgouge deformation for frame 6-18, displacement of 93.6 mm, Magnification x10, P03

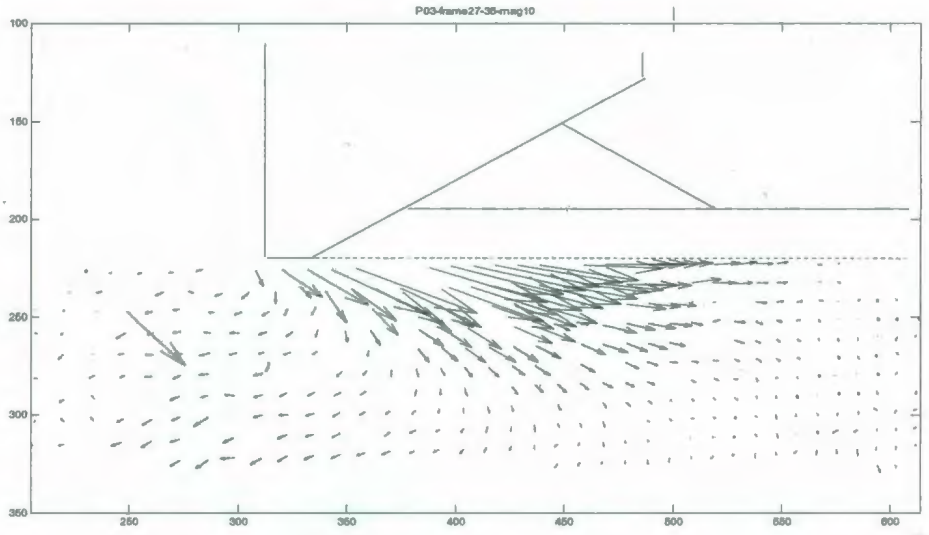

Figure 5-22 PIV subgouge deformation for frame 27-36, displacement of 187.2 mm, Magnification x10, P03

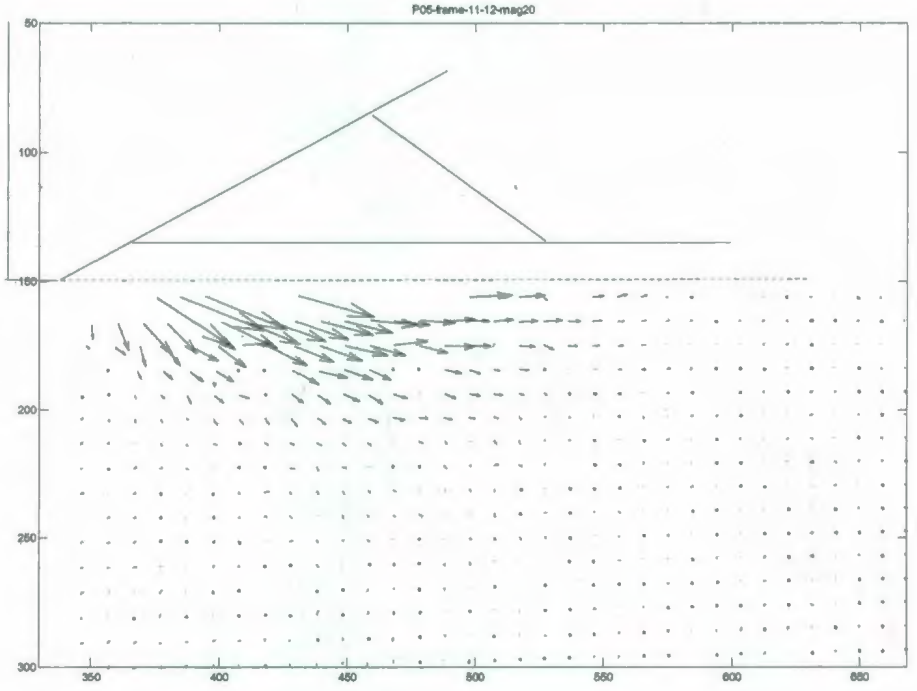

Figure 5-23 PIV subgouge deformation for frame 11-12, displacement of 198 mm, Magnification x20, P05

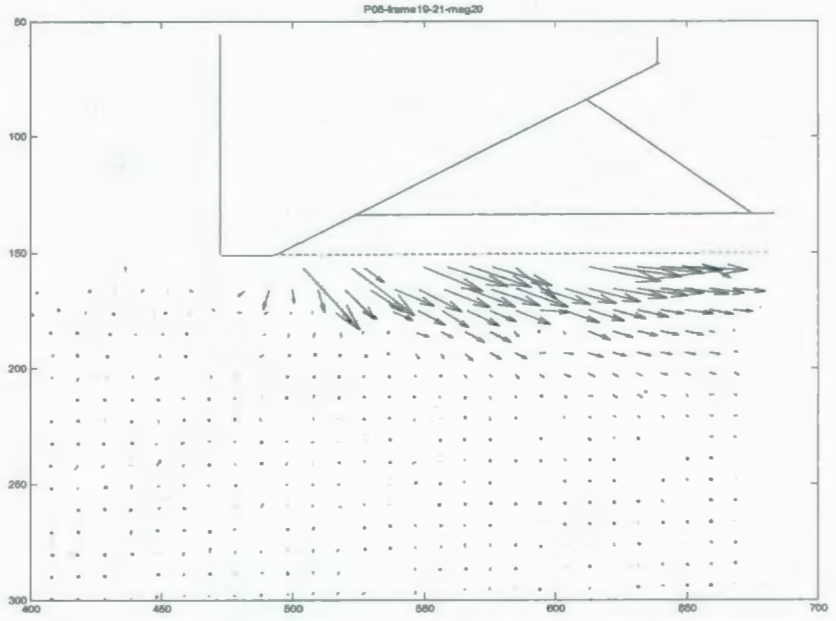

Figure 5-24 PIV subgouge deformation for frame 19-21, displacement of 346.5 mm, Magnification x20, P05

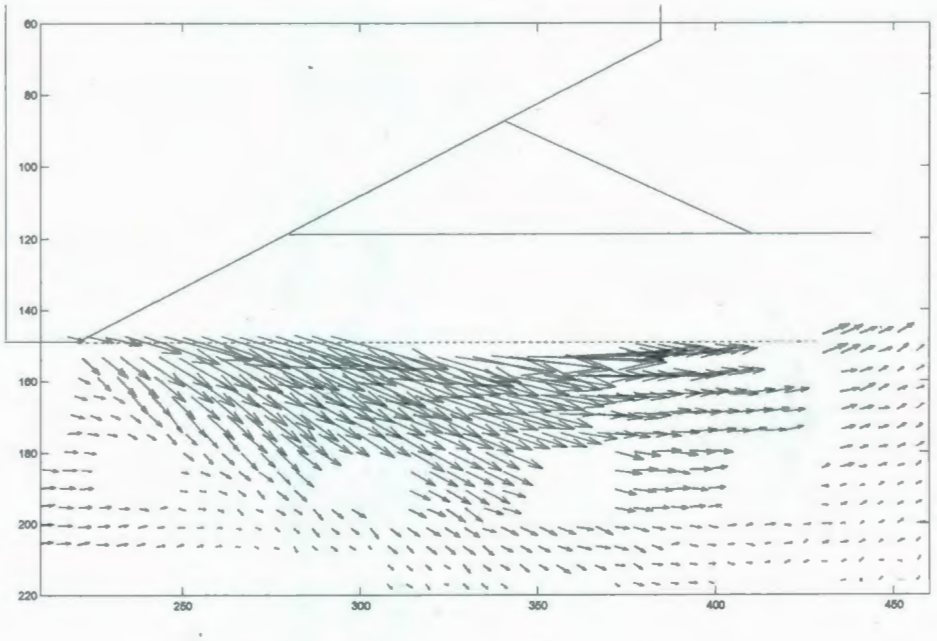

Figure 5-25 PIV subgouge deformation for frame 19-21, displacement of 178.1 mm, Magnification x20, P06

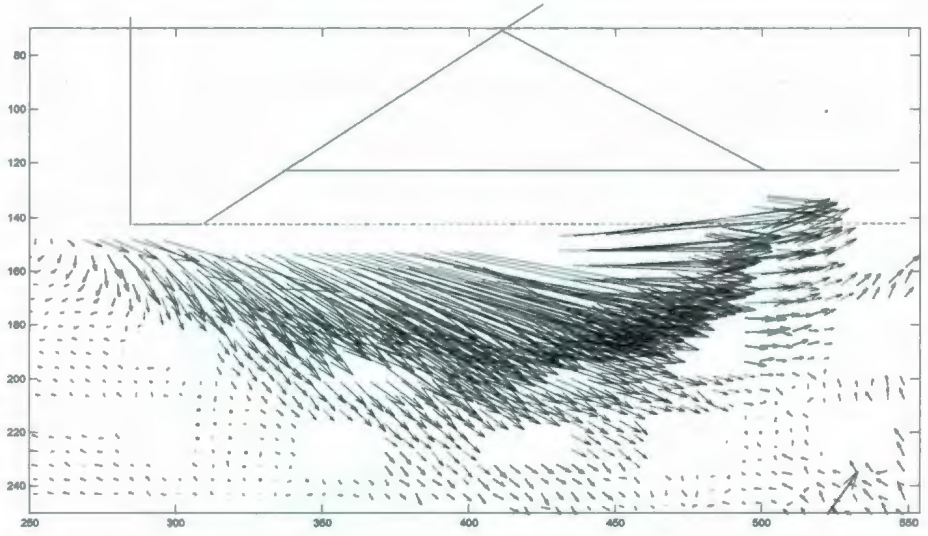

Figure 5-26 PIV subgouge deformation for frame 24-31, displacement of 262.9 mm, Magnification x20, P06

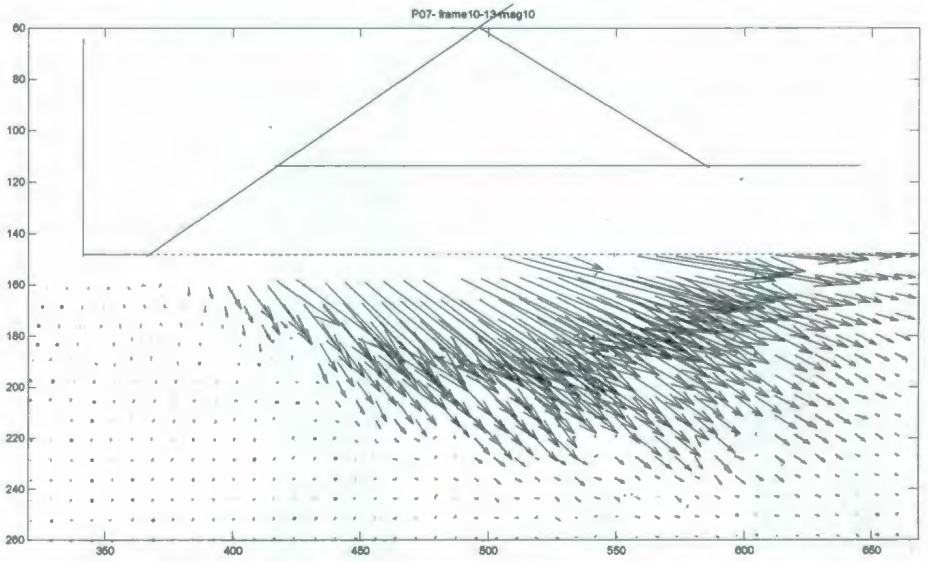

Figure 5-27 PIV subgouge deformation for frame 7-9, displacement of 246.9 mm, Magnification x10, P07

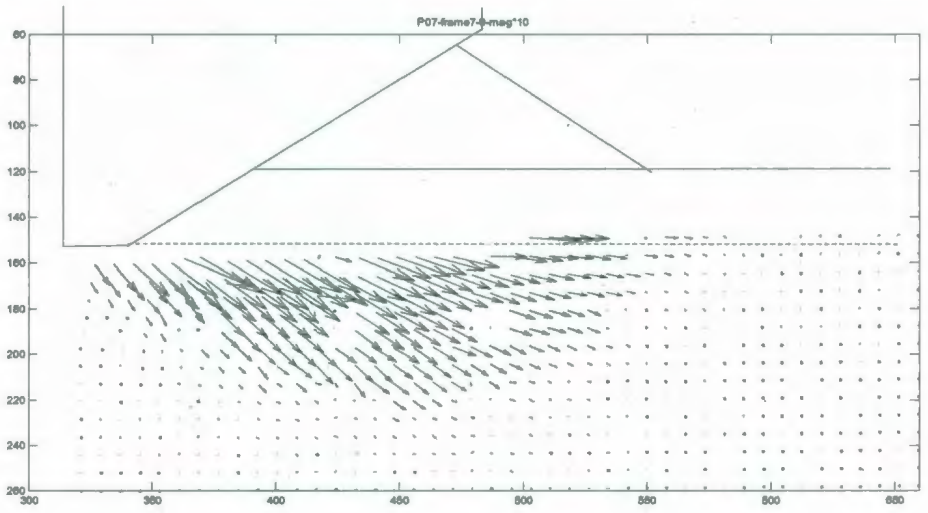

Figure 5-28 PIV subgouge deformation for frame 10-13, displacement of 356.7 mm, Magnification x10, P07

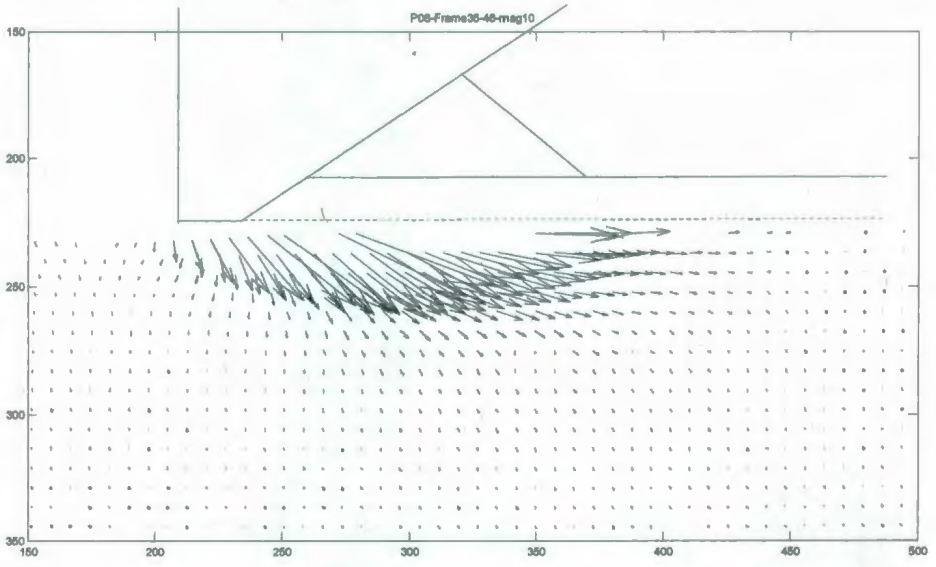

Figure 5-29 PIV subgouge deformation for frame 35-46, displacement of 209.9 mm, Magnification x10, P08

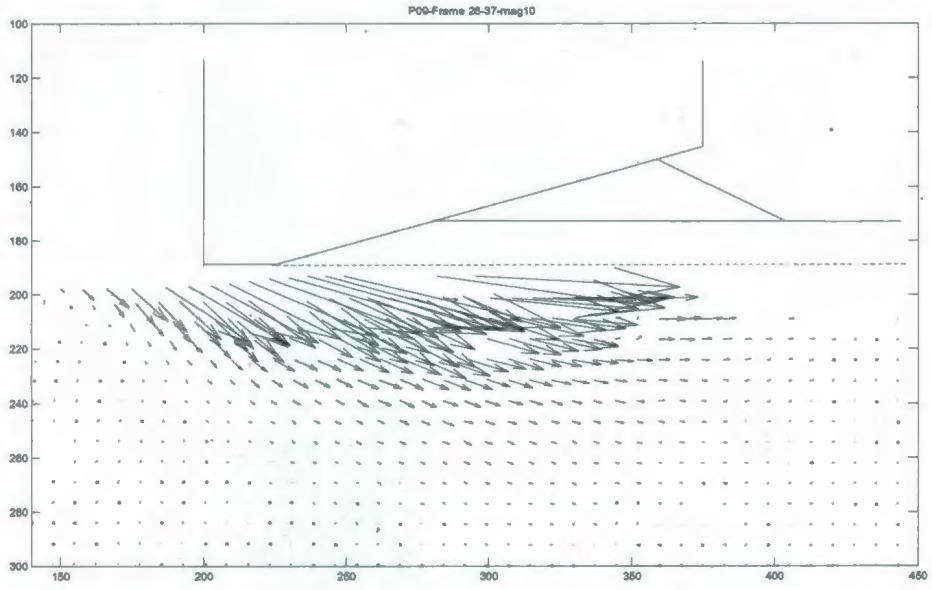

Figure 5-30 PIV subgouge deformation for frame 28-37, displacement of 175 mm, Magnification x10, P09

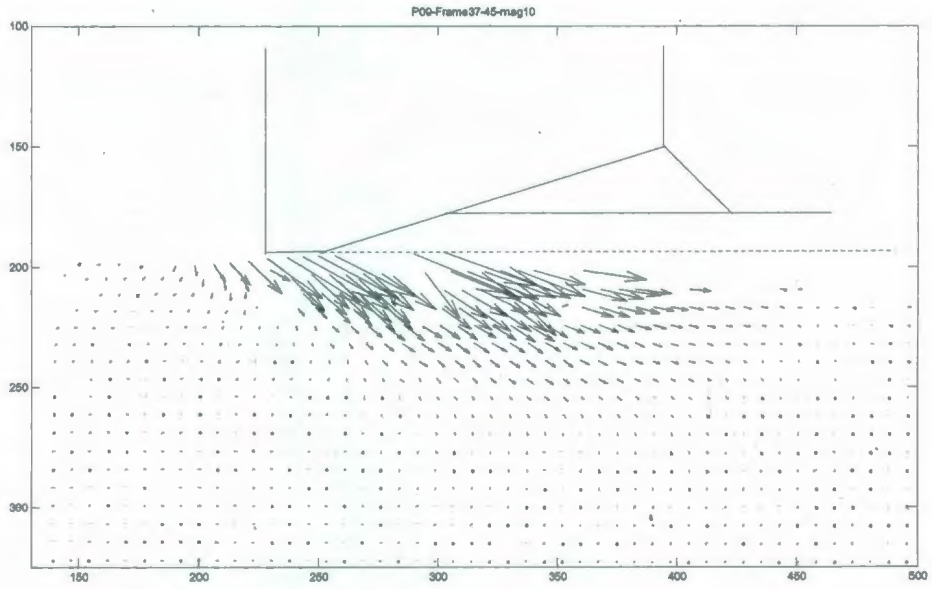

Figure 5-31 PIV subgouge deformation for frame 37-45, displacement of 212.8 mm, Magnification x10, P09

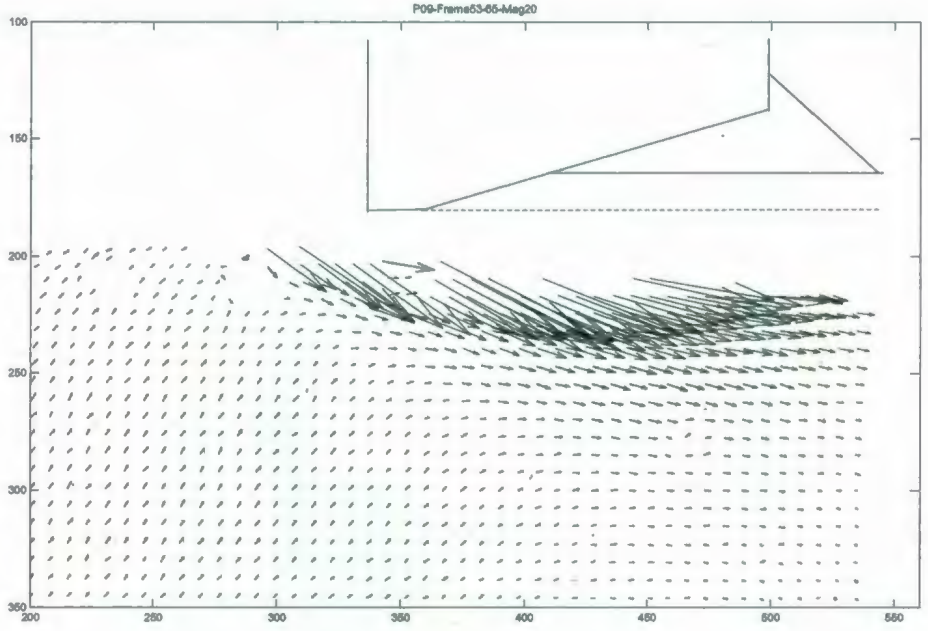

Figure 5-32 PIV subgouge deformation for frame 53-65, displacement of 307.4 mm, Magnification x20, P09

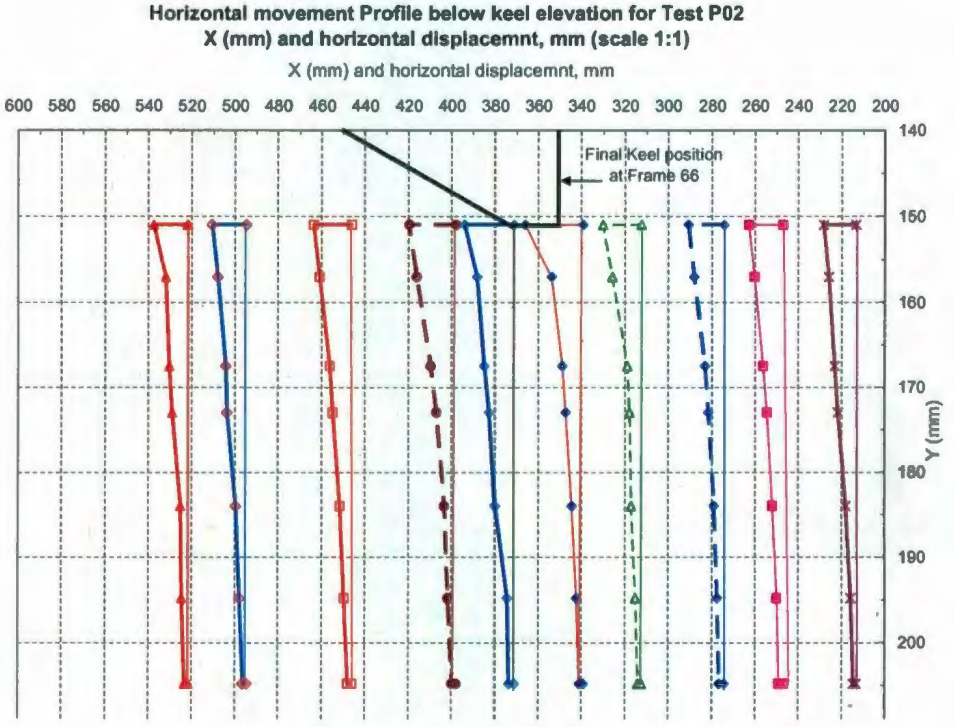

Figure 5-33 Horizontal movement profile below keel elevation for test P02

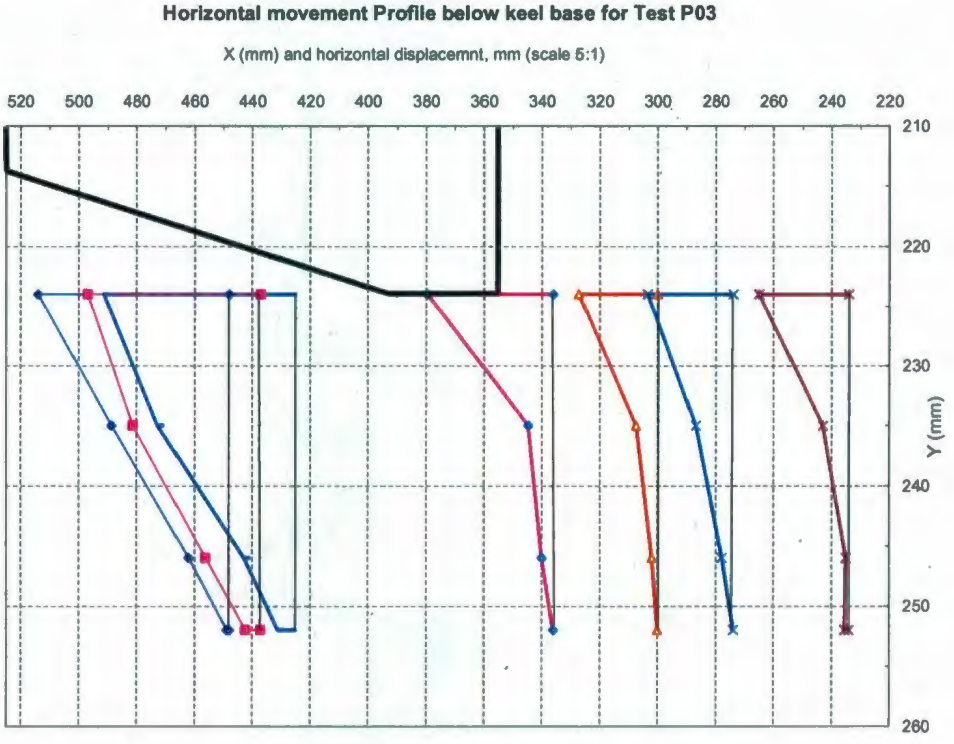

Figure 5-34 Horizontal movement profile below keel elevation for test P03

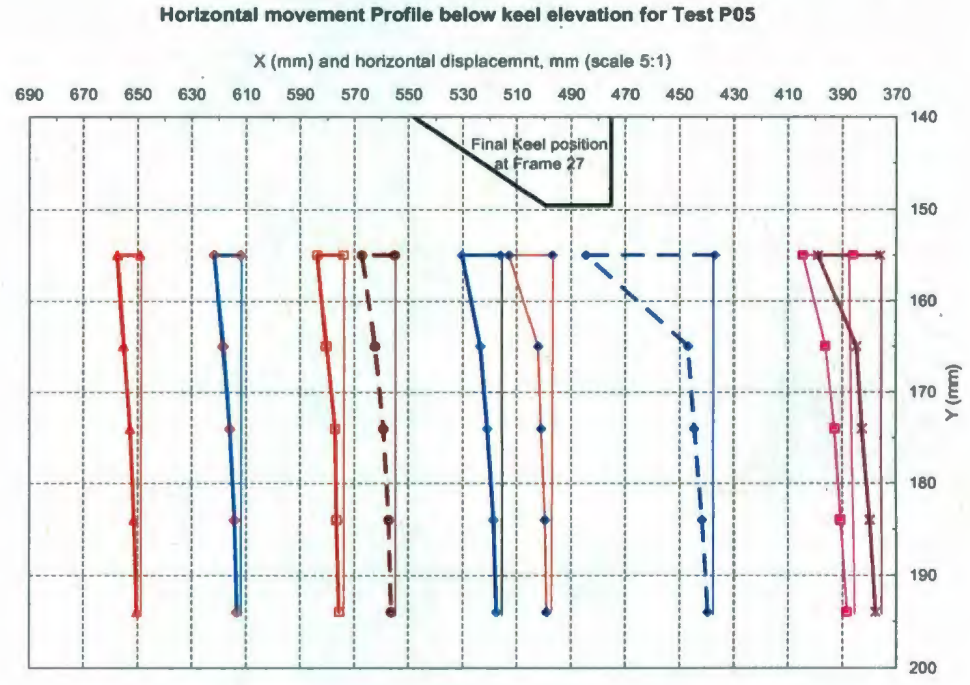

Figure 5-35 Horizontal movement profile below keel elevation for test P05

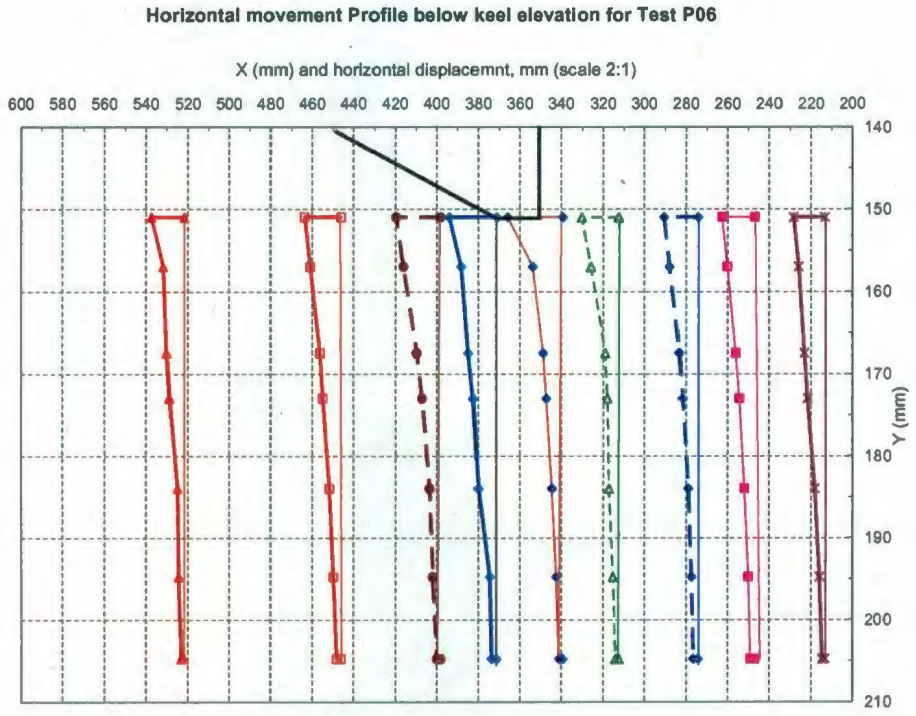

Figure 5-36 Horizontal movement profile below keel elevation for test P06

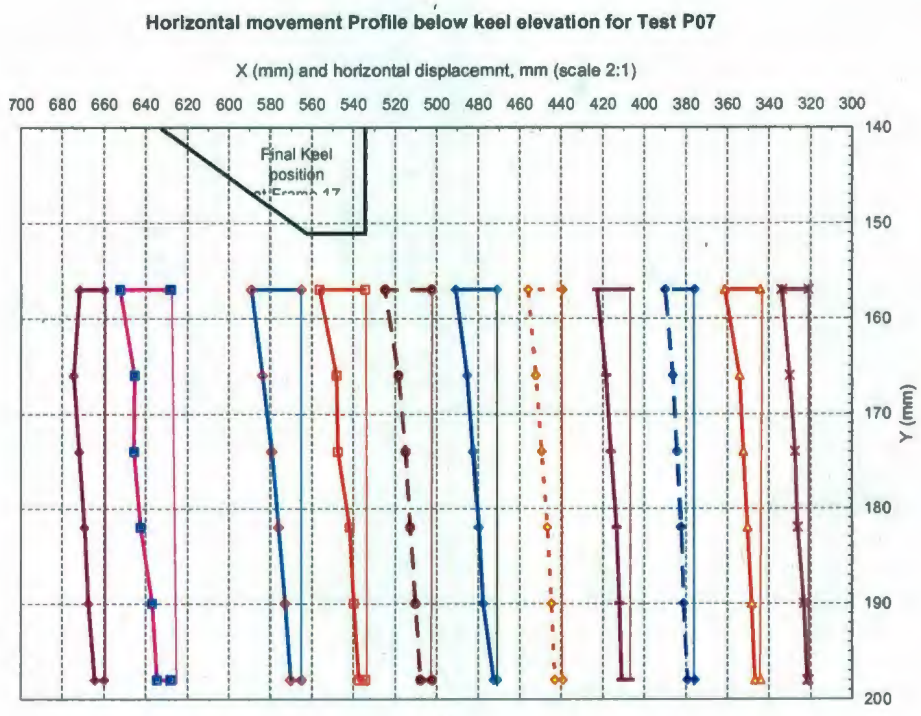

Figure 5-37 Horizontal movement profile below keel elevation for test P07

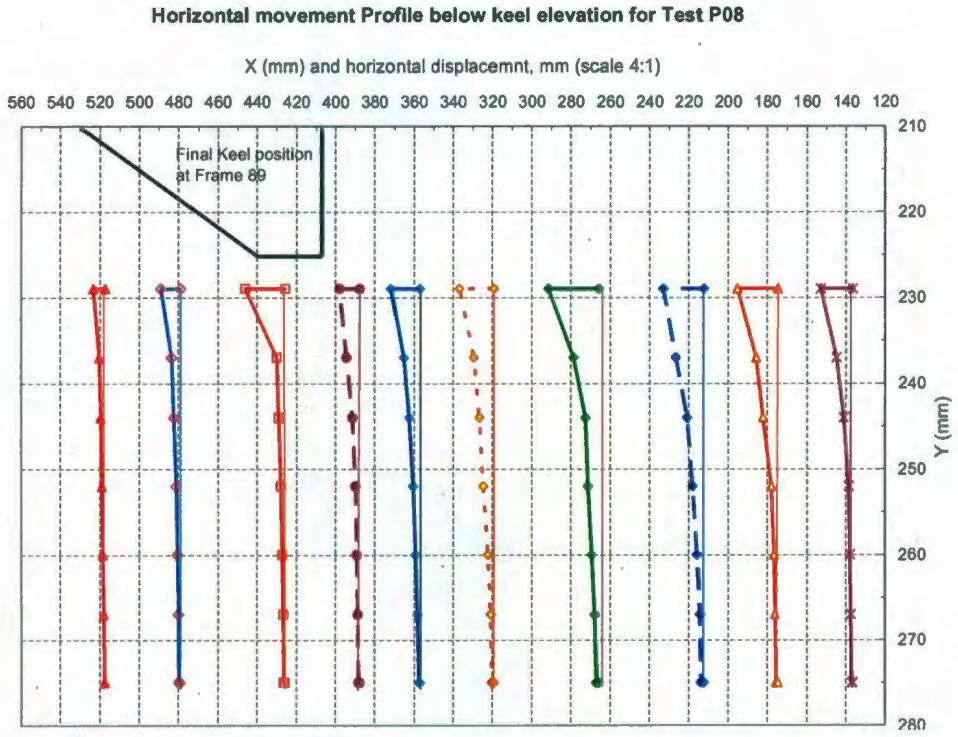

Figure 5-38 Horizontal movement profile below keel elevation for test P08

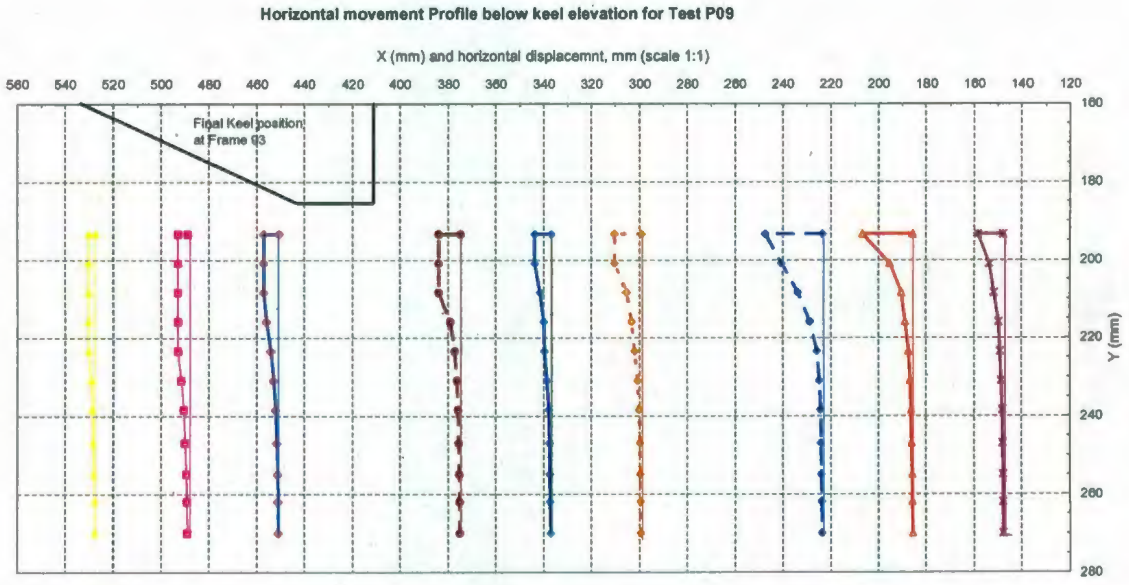

Figure 5-39 Horizontal movement profile below keel elevation for test P09

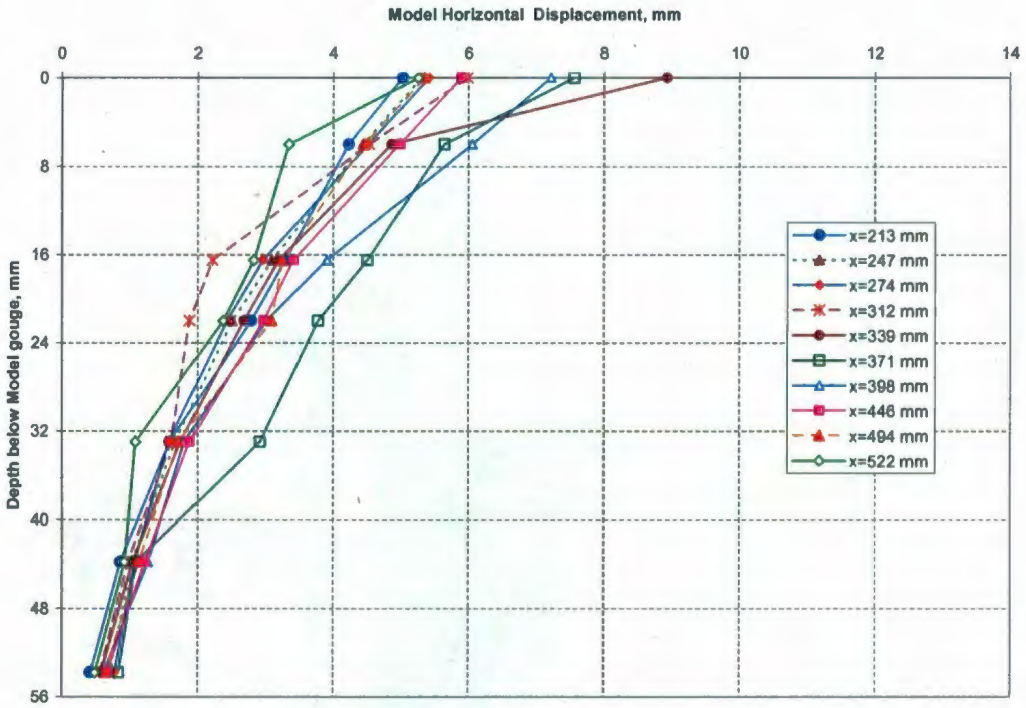

Figure 5-40 Subgouge horizontal displacement for P02

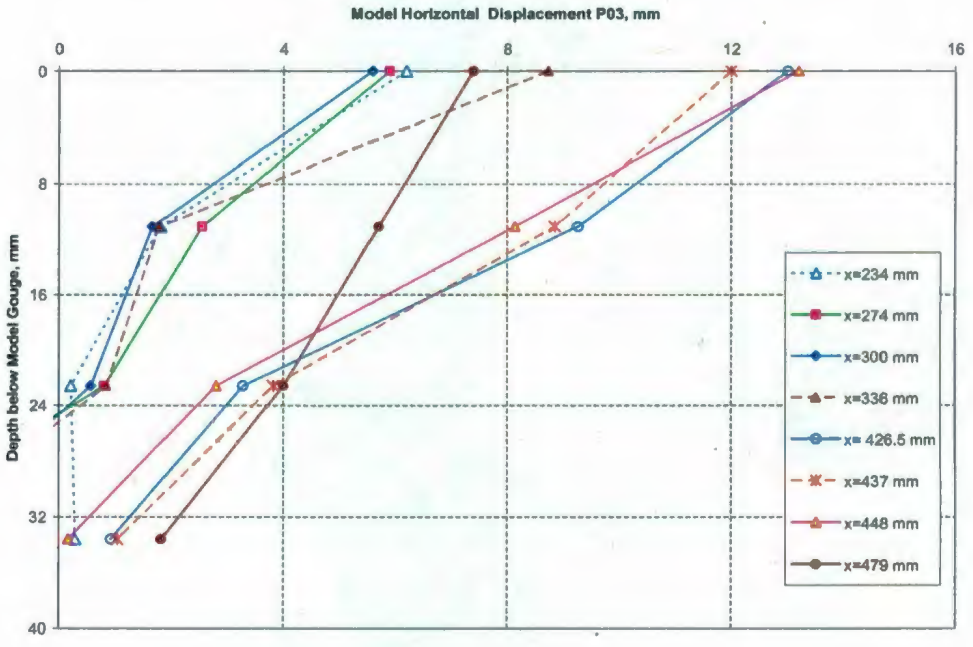

Figure 5-41 Subgouge horizontal displacement for P03

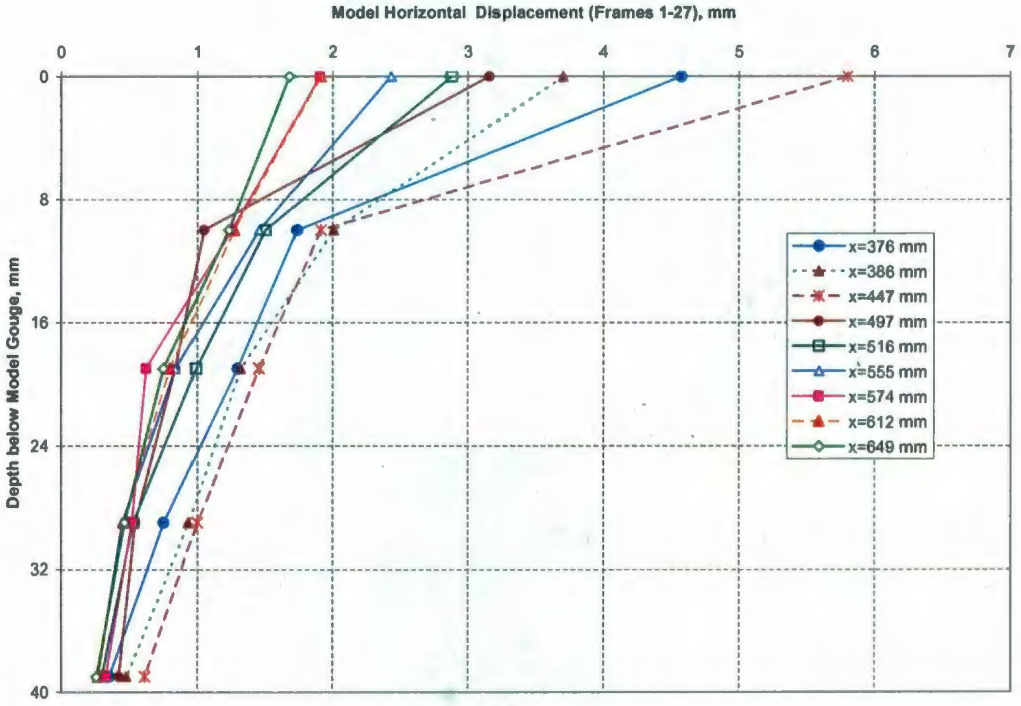

Figure 5-42 Subgouge horizontal displacement for P05

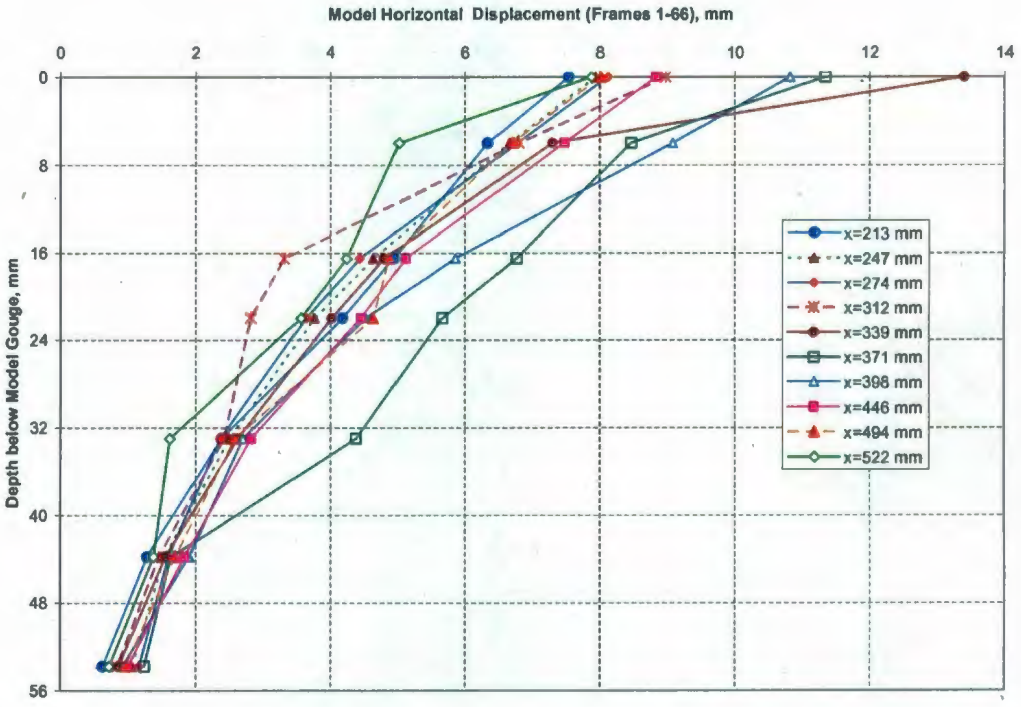

Figure 5-43 Subgouge horizontal displacement for P06

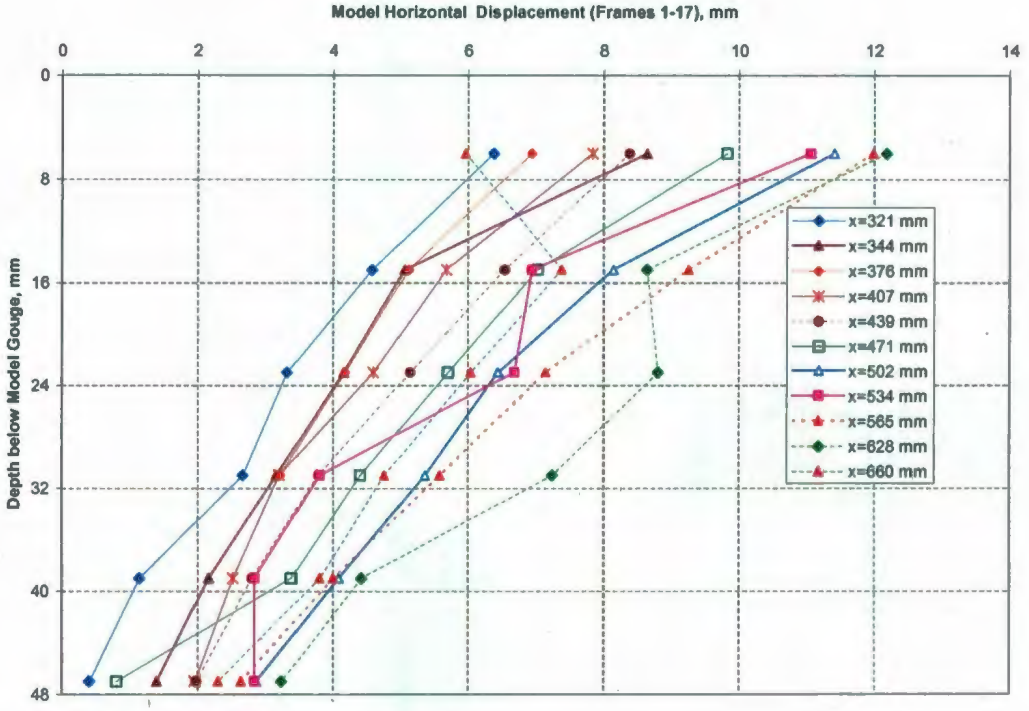

Figure 5-44 Subgouge horizontal displacement for P07

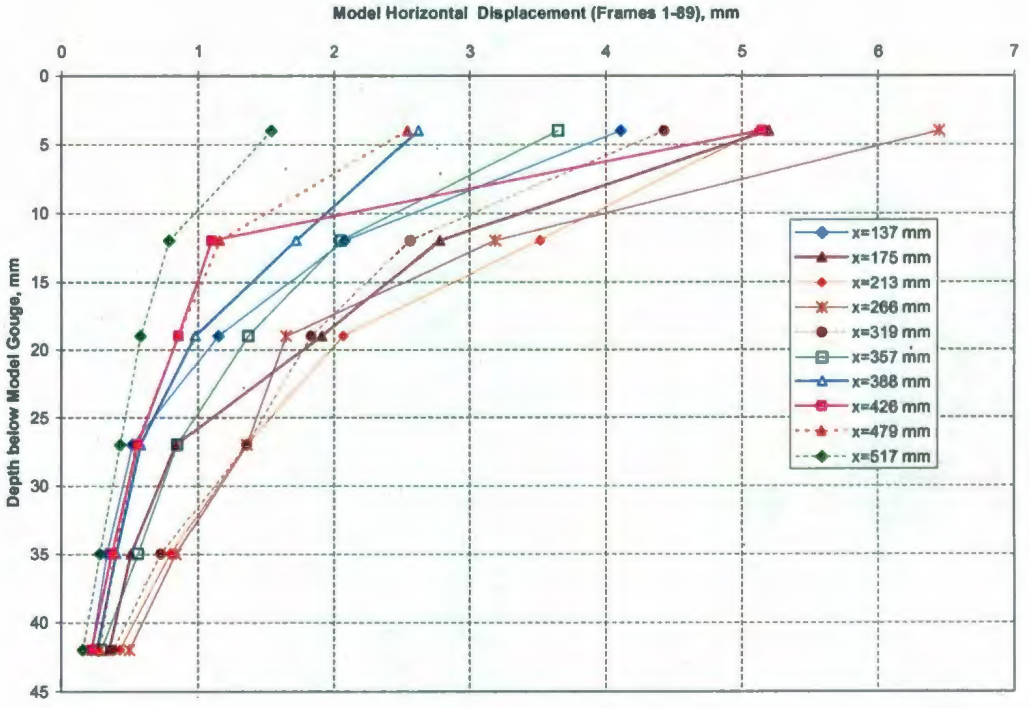

Figure 5-45 Subgouge horizontal displacement for P08

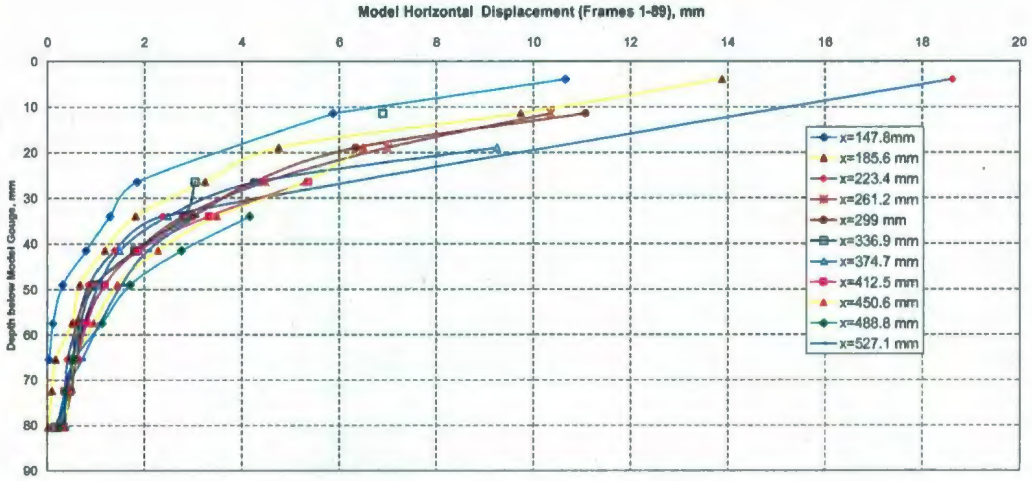

Figure 5-46 Subgouge horizontal displacement for P09

5.4 Gouge Form and Mound

Before each centrifuge test, a soil mound was placed in front of the model ice keel to reduce the require gouge length required to reach the steady state. When the keel is moving in the sand, sand accumulates to the side of the keel and in front of the keel. After the keel has passed, some of the sand mound at the side of the keel falls down back into the gouge path, so the gouge width will be smaller than the width of the keel. As the keel is moving in the sand, the mound will increase in height until reaching its maximum height . Figure 5-47 and Figure 5-48 show the side view and the top view of the gouge for P05 and P06 as an example. The other top and side views of the gouge are in Figure A.21 to Figure A.27. Figure 5-49 to Figure 5-53 show the measured dimension of the gouge and the mound in front of the keel at the end of the test.

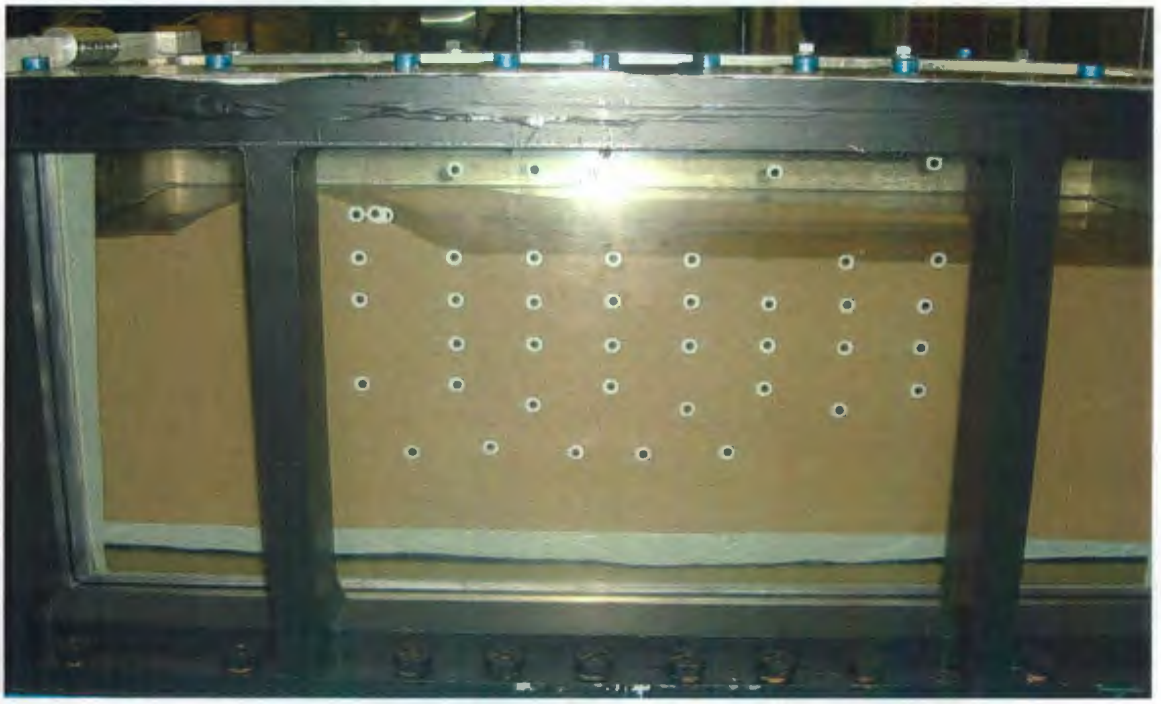

Figure 5-47 Side view of gouge shape for test P05

Figure 5-48 Top view of gouge shape for test P06

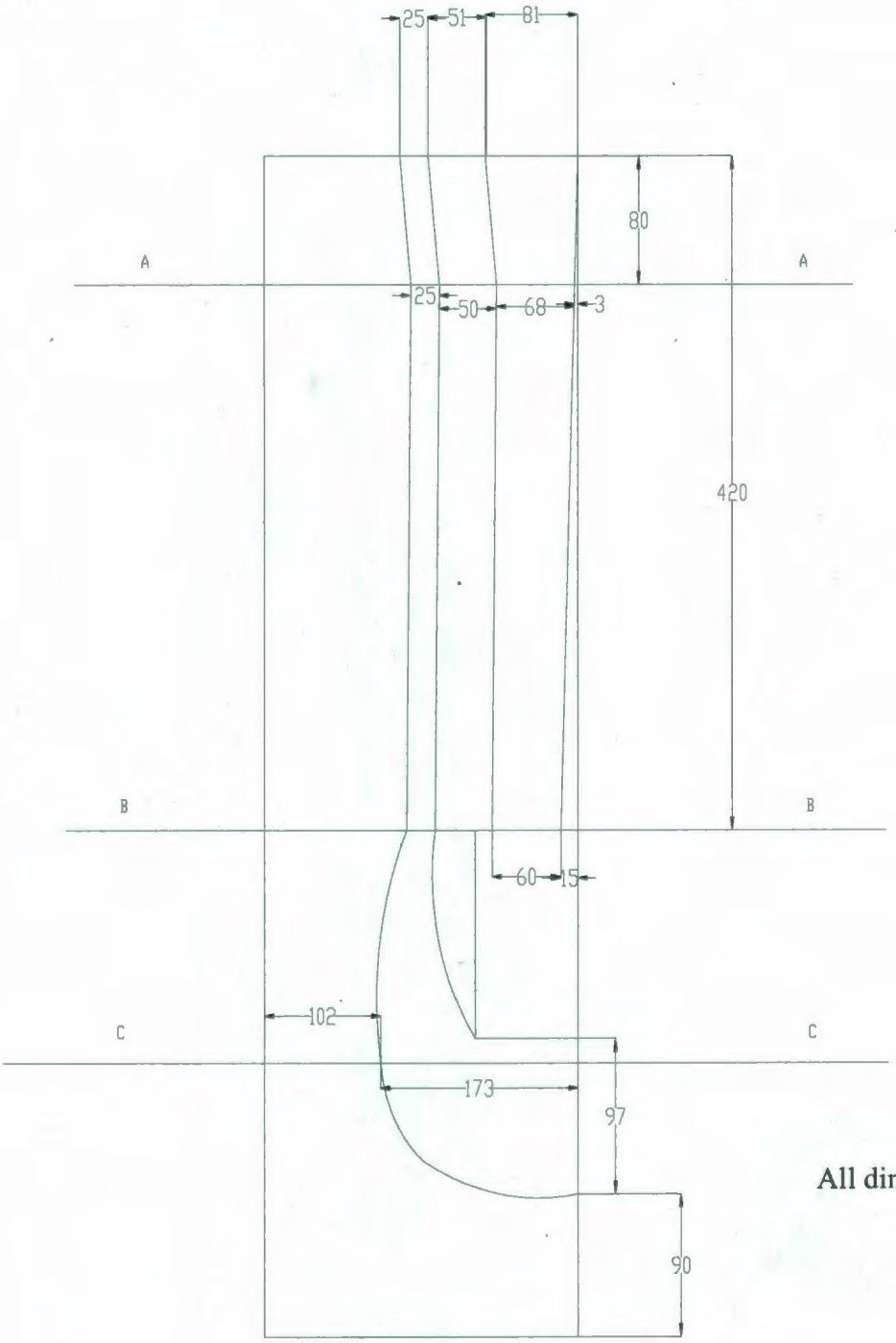

All dimentions are in mm

Figure 5-49 Top view of gouge shape and dimension for test P03

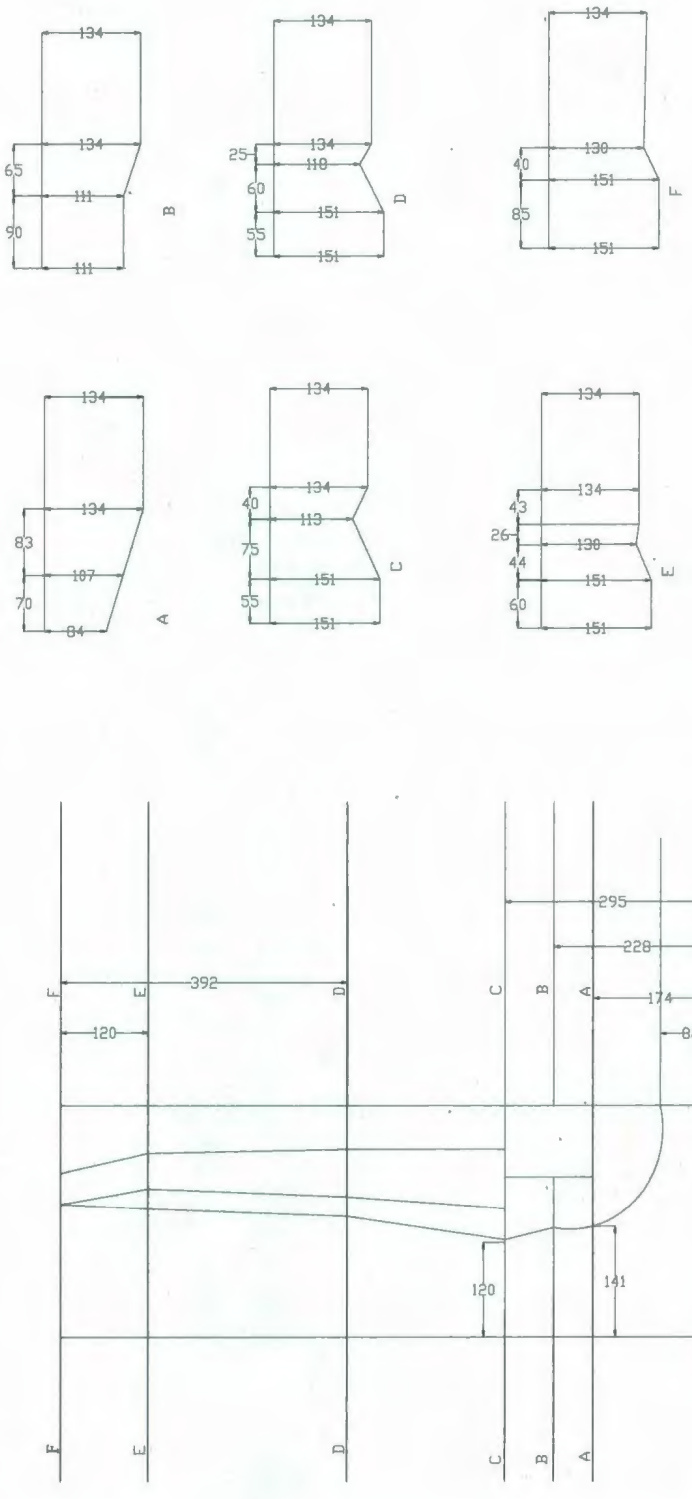

Figure 5-50 Top view of gouge shape and dimension for test P05

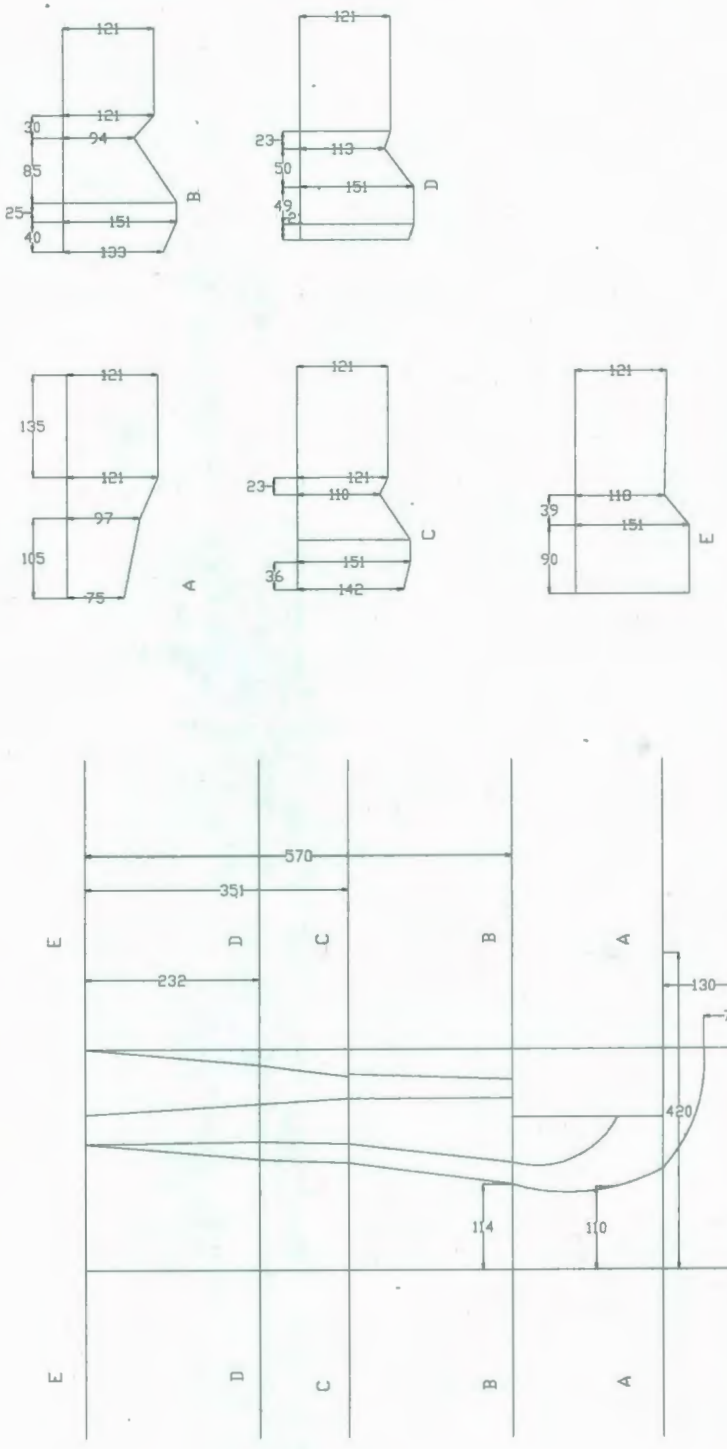

All dimentions are in mm

Figure 5-51 Top view of gouge shape and dimension for test P06

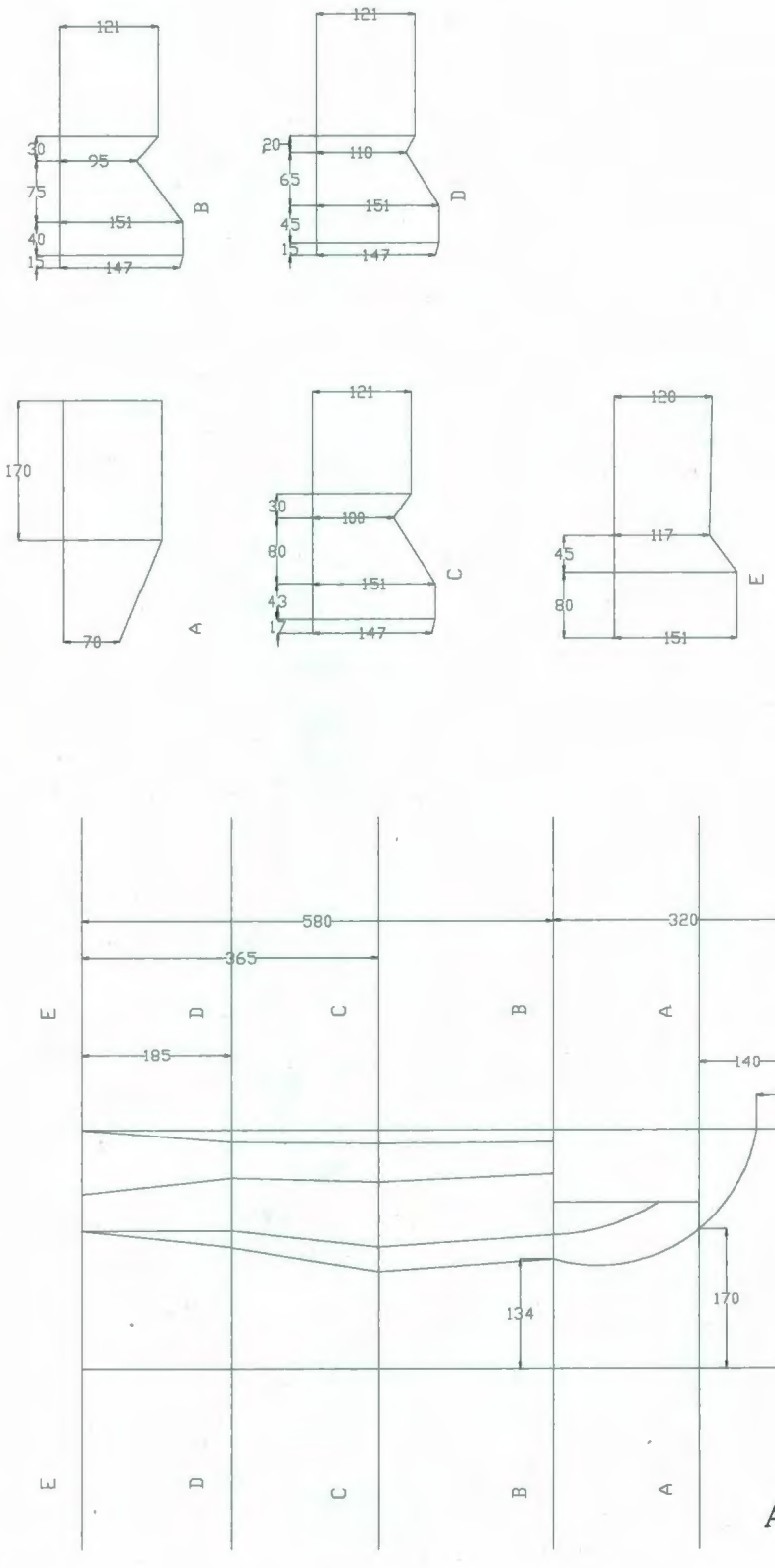

Figure 5-52 Top view of gouge shape and dimension for test P07

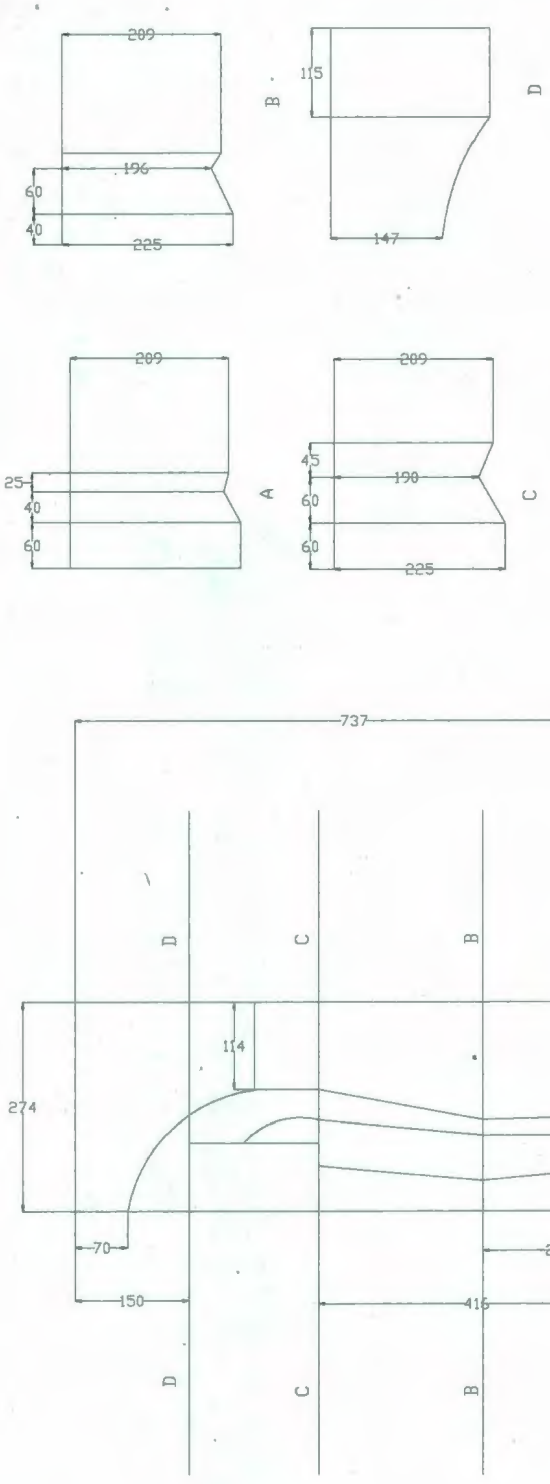

All dimentions are in mm

Figure 5-53 Top view of gouge shape and dimension for test P08

6 ANALYSIS

6.1 Introduction

A total of seven tests were conduced. For the seven tests, all the parameters and both horizontal and vertical forces that were measured from the centrifuge tests are shown in Table 6-1. The parameters were different between the seven tests. A 30 degrees attack angle for the model ice keel was used for tests, P02 through to P08. A 15 degrees attack angle for the model ice keel was used for test P09. The gouge depth ranged from 0.18 m to 2.4 m in prototype terms for the seven tests; P05 and P08 had the smallest gouge depth. The keel speed ranged from 0.5 to 55 mm/s.

Table 6-1 Sand test results for vertical and horizontal loads in prototype parameters

Gouge	P02	P03	P05	P06	P07	P08	P09
Angle(degrees)	30	30	30	30	30	30	15
Depth(m)	1.3	1.43	0.18	2.3	2.4	0.19	1.2
Width(m)	10	10	2.2	14.4	14.4	2.2	16
Dr	93.6	51.5	58	50.8	39	68.1	38.6
Fv(MN)	25.3	9.9	0.14	65.2	52.5	0.45	32.4
Fh(MN)	8	7.7	0.095	47	45.4	0.32	28.2
Fv/Fh Ratio	3.15	1.28	1.5	1.39	1.28	1.3	1.15
Speed (mm/s)	0.5	0.5	1.1	1.1	5.5	54.6	56.8
Mound height(m)	3.38	2.145	0.648	3.749	4.032	0.739	3.132
Combined height(m)	4.68	3.575	0.828	6.049	6.432	0.929	4.332

P02 was conducted in dry dense sand and P03 was in water saturated medium density sand. These two tests were aimed at proving the equipment and techniques. Tests P07, P08 and P09 were conducted with a fast gouge rate using a 30 cst viscous pore fluid to retard excess pore pressure dissipation. The subgouge deformation was determined by a PIV analysis for all PIRAM tests. All the deformation for different layers below keel is determined with the largest horizontal deformation of the layer in the period.

6.2 Vertical Settlement during Centrifuge Test

During the spin up of the centrifuge test, the model sand will be compressed by the acceleration level acting on the model, thus reducing the soil depth, which means that the gouge depth and the density of the model sand will change during the centrifuge spin up. For this reason, LVDT'S are necessary for measuring the exact settlement during the centrifuge test (Figure A. 14 to Figure A. 20).

Table 6-2 presents the settlement of model sand during sand preparation and centrifuge testing which shows that usually the settlement of model sand will increase when the g level is higher or the density is lower.

Table 6-2 Model sand settlement during preparing and centrifuge testing

Test I.D.	Original Ds (mm)	Density after sand raining (kg/m^3)	Settlement during saturation and loading (mm)	Settlement during centrifuge spin up (mm)	Density during centrifuge test (kg/m^3)	Actual Ds during centrifuge test (mm)	G level
P02	25	1587		1.3	1592	23.7	55.6
P03	29	1443	1.0	2.2	1457	25.7	55.6
P05	17	1470	1.3	0.7	1481	15.0	12.2
P06	33.5	1432	2.8	1.9	1455	28.8	80.0
P07	35.4	1396	2.6	2.6	1421	30.2	80.0
P08	17.2	1502	0.6	0.6	1507	15.9	12.2
P09	21.5	1397	2.0	4.4	1420	15.1	80.0

6.3 Frontal Berm

In all tests it was observed that the height of the berm which is measured from the ground surface to the top of the sand mound increases with the keel moving forward until it reaches a maximum height as the keel reaches the end of the test position. The frontal berm height has a significant effect on the force and subgouge deformation. Kappa value was introduced to describe the frontal berm height. Kappa value is the frontal berm height as multiple of gouge depth as shown in Figure 6-1. Table 6-3 is shown the Kappa value that estimated when the height of the berm is reaching the maximum level.

Figure 6-1 Frontal berm height as multiple of gouge depth, k

Because of the limit space in the box, the keel displacement was limited. There was an initial berm made for each test during preparation to reduce the distance required for the frontal berm reaching the steady state. The berm grows until reaching steady state condition. The growth of the berm is also associated with the growth of the gouge force. Figure 6-2 is the comparison of the kappa value from the three different test programs. The kappa value seems to increase with the increasing of the attack angle of the ice keel for all the tests. There are other differences between the three programs which may cause the differences in kappa value between programs. Test P02 which is in dry sand is not included in the plot.

Table 6-3 Sand test results and kappa value in prototype parameters

Test I.D.	Attack angle, α (deg)	W/Ds	Speed (mm/sec)	Kappa	Maximum Fv, MN during steady state	Maximum Fh, MN during steady state	Average Fv/Fh during steady state
P02	30	7.6	0.5	2.6	25.3	8.0	3.15
P03	30	7.0	0.5	1.5	9.9	7.7	1.28
P05	30	12	1.1	3.6	0.14	0.095	1.5
P06	30	6.25	1.1	1.63	65.2	47.0	1.39
P07	30	5.96	5.5	1.68	52.5	45.4	1.28
P08	30	11.3	54.6	3.89	0.45	0.32	1.3
P09	15	13.3	56.8	2.61	32.4	28.2	1.15

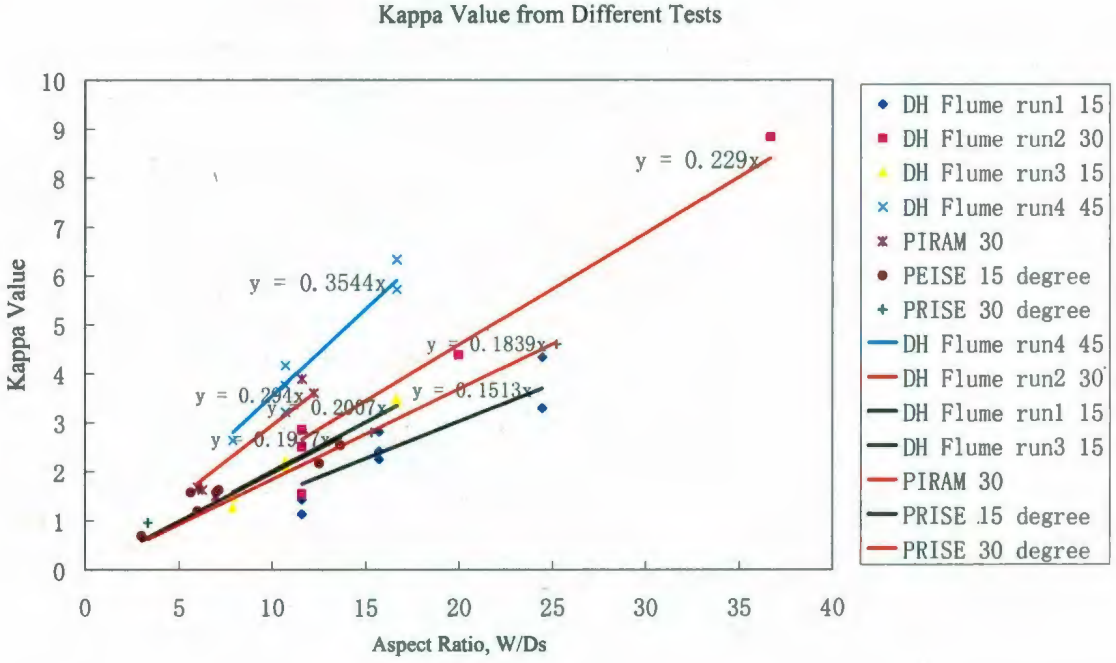

Figure 6-2 Kappa value from different test program

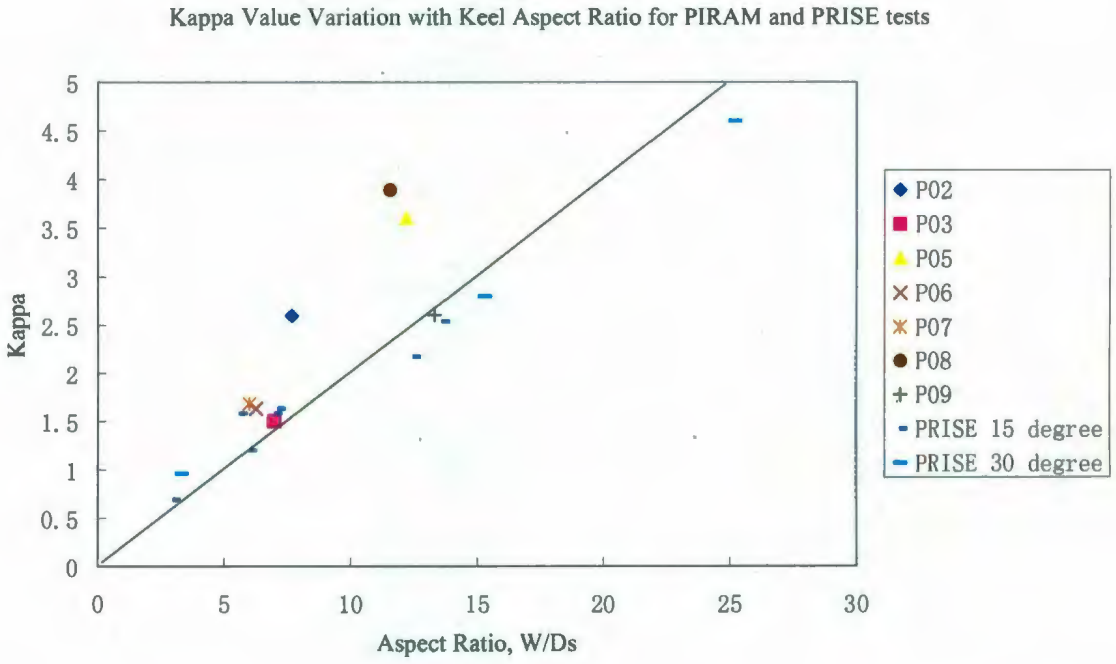

Figure 6-3 Kappa value versus aspect ratio for PIRAM and PRISE tests

Figure 6-3 is the plot of kappa value versus aspect ratio for PRISE and PIRAM tests which have the larger gouge depth. It indicated that the frontal berm height normalized by gouge depth linearly corresponds with the aspect ratio. The relationship between kappa value and aspect ratio can be expressed as kappa=W/5Ds. P02, P05 and P08 are significant outliers. P02 was conducted in dry sand; P05 and P08 had smaller gouge depth. Figure 6-3 indicated that there is no significant effect for kappa value between 15 degree and 30 degree for deep gouge depth.

6.4 Bearing Pressure

Bearing pressure is the normal bearing force on the face over a bearing area which is the inclined keel face including the frontal berm. For the bearing pressure, σ_b, C-CORE (2008) developed an empirical equation for bearing pressure as $\sigma_b(\text{MPa}) = 0.09\ D_s\ (\text{m})^{1.5}$ as shown in Figure 6-4 C-CORE (2009b). Figure 6-5 shows the bearing pressure at steady state for PIRAM test and the empirical equation line. It can be seen from the figure that the PIRAM tests are capture well with the empirical equation line. P02, P05 and P08 are higher than the empirical equation line. This may because of an increased soil dilation under lower effective stress and the reduced soil self weight which decrease the gouge resistance in these 3 tests. The reason of the discrepancy between P06 and empirical equation line is unknown.

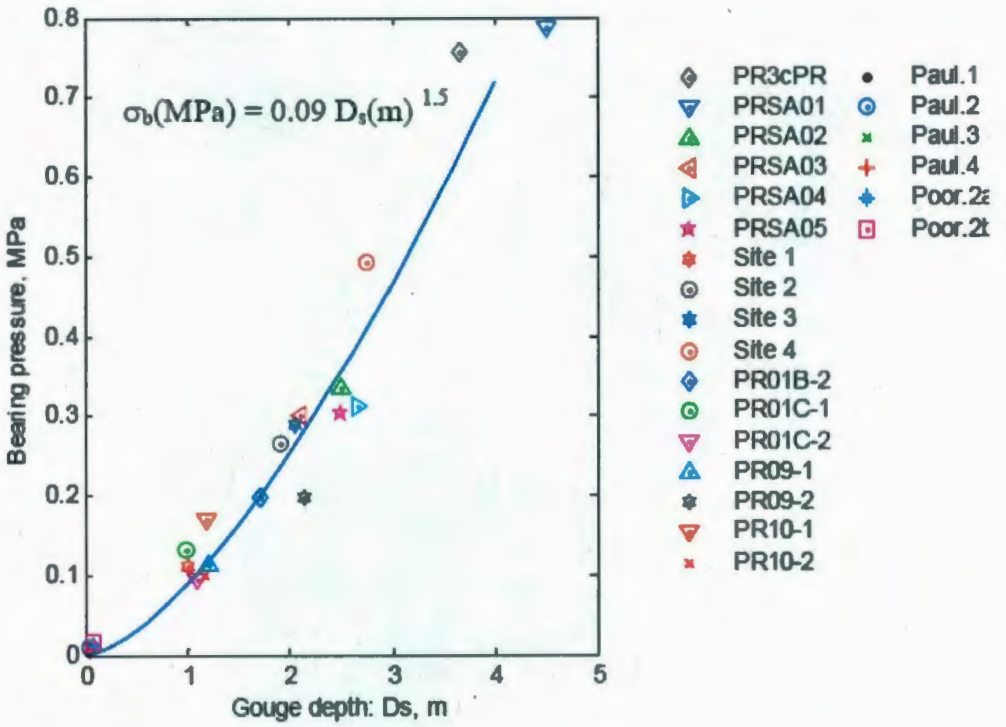

Figure 6-4 Keel bearing pressure on gouge and berm surcharge C-CORE (2009b)

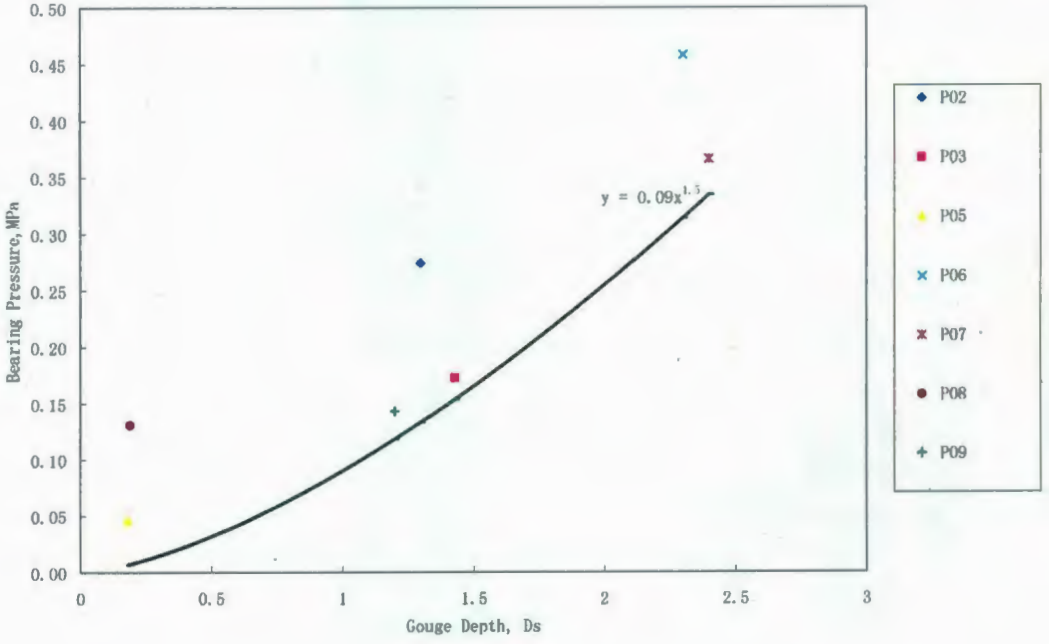

Figure 6-5 Bearing pressure versus gouge depth

6.5 Gouge Force Variation

6.5.1 Gouge Force with Aspect Ratio

The sand test results for vertical and horizontal loads in prototype parameters are shown in Table 6-5. As the frontal berm grows, the gouge force increases with keel displacement until it reaches a cyclic steady state which explained in section 5.3. Figure 6-6 shows the force per unit width versus the combined gouge depth which shows clear tendency that the force increase with the increasing of the combined depth.

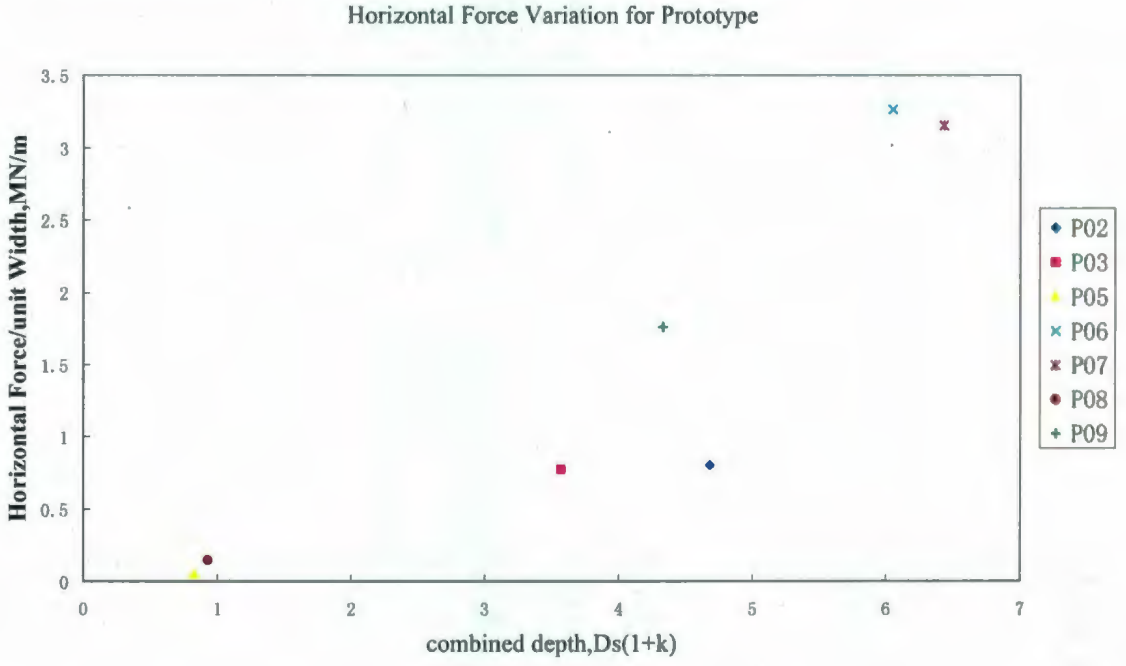

Figure 6-6 Prototype horizontal force per unit width versus combined depth

Figure 6-7 C-CORE(2009) is the model test horizontal gouge force normalization versus the aspect ratio. The data plotted in the figure contains PIRAM test, PRISE test Phase 3a and Phase 3c, Memorial University 1 g test and Site test (Table A 1). The combined

depth trend line is considered by normalizing force per width by the square of the combined depth and the submerged unit weight of the sand. There are four groups of data in Figure 6-7. One comprises 7 shallow gouge tests which are P05, P08 and Memorial 1 g tests. The second group contains P02 and P10. P02 is conducted in dry sand and P10 is using a double-keel. The other two groups are for deeper gouge depth greater than 0.3m with attack angle of 15 and 30 degrees.

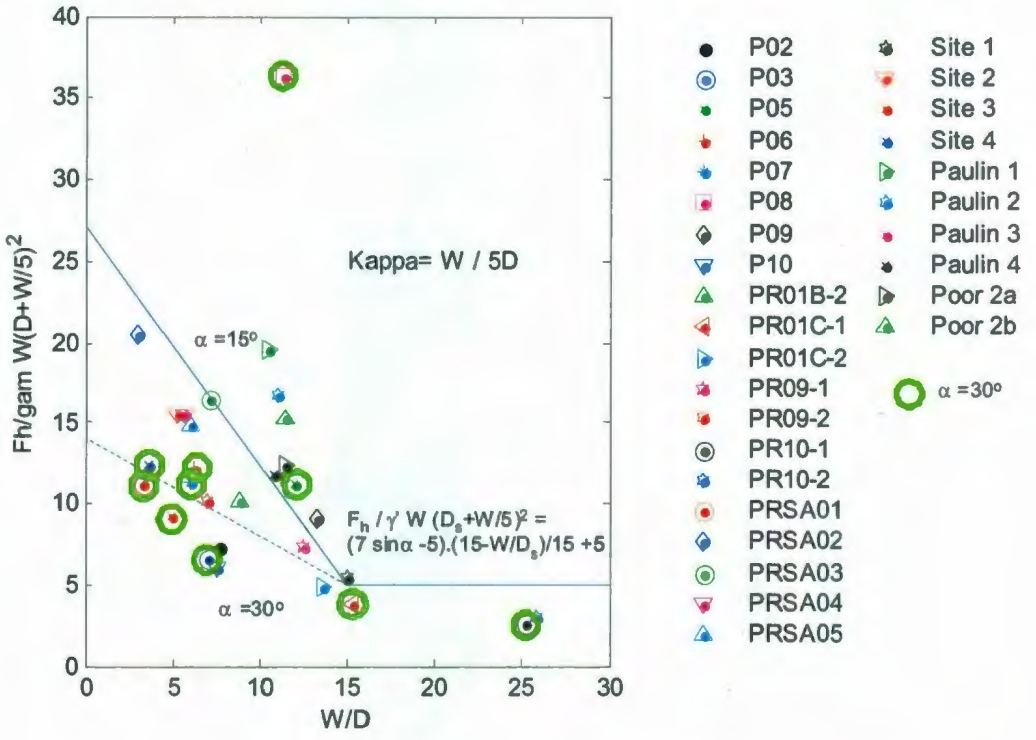

Figure 6-7 Horizontal gouge force normalisation C-CORE(2009b)

An empirical relation was fitted to these two groups of data. These empirical relations are compared with the analytical solution of Walter and Phillips (1998) with the PRISE JIP for sand with a submerged unit weight of 10 KN/m^3 and gouge depth of 0.2, 0.5, 1.0, 2.0 and 3.0m. The peak and critical state friction angles are 37 and 35 degrees in Figure

6-8. The empirical relation is consistent with the analytical force model where the empirical relation is:

$$F_h / \gamma' W (D_s+W/5)^2 = (7\sin\alpha - 5)(15-W/D_s)/15 + 5 \quad \text{for } W/D_s < 15, \text{ and}$$

$$= 5 \quad \text{for } W/D_s > 15$$

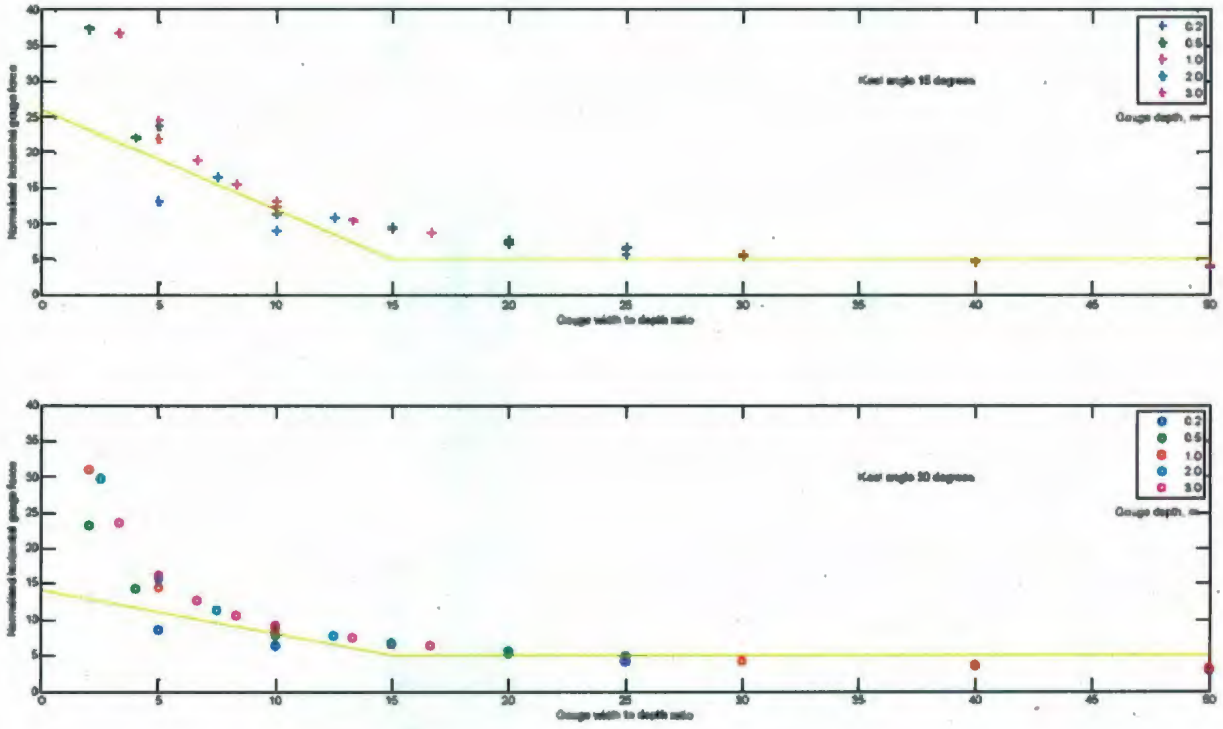

Figure 6-8 Lateral gouge force comparison of empirical and analytical functions

6.5.2 Force Ratio

As shown in Figure 6-9, all the tests that used saturated sand are in a narrow area which can be expressed as F_v/F_h = 1.15 to 1.5. P02 is a dry sand test with a force ratio to aspect ratio of 3.15. This higher ratio for P02 may because it does not have excess pore pressures and water resistance for horizontal force. It may also because of the lack of buoyancy force in vertical force. From P03 to P08 with an attack angle of 30 degrees, the

force ratio to aspect ratio is 1.28 to 1.5 with an average of 1.39. The force ratio to aspect ratio for P09 is 1.15, which is the lowest, as the attack angle is 15 degrees.

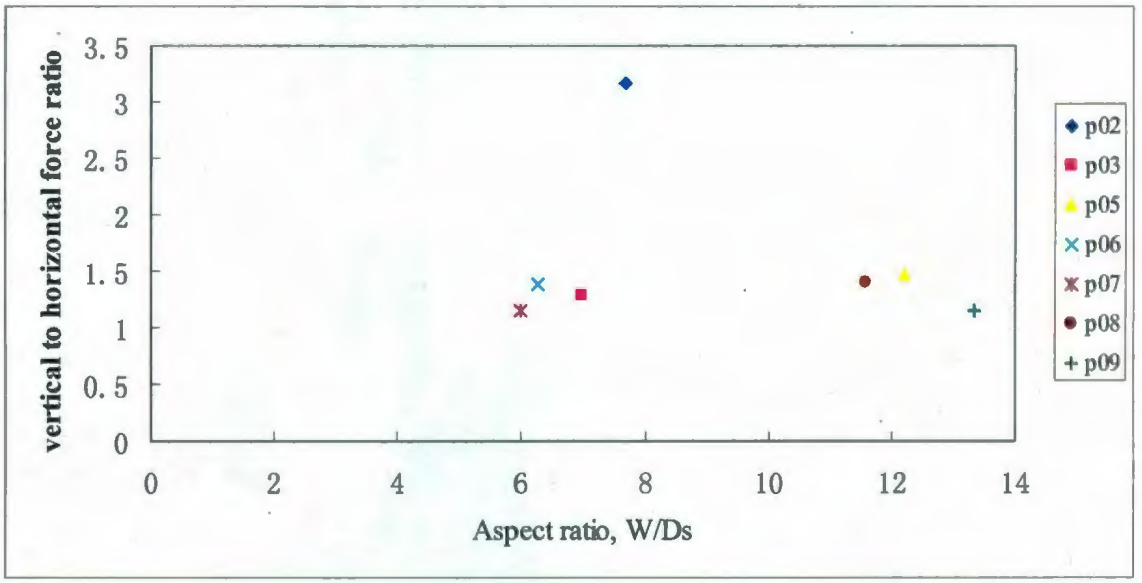

Figure 6-9 Prototype force ratio to the aspect ratio

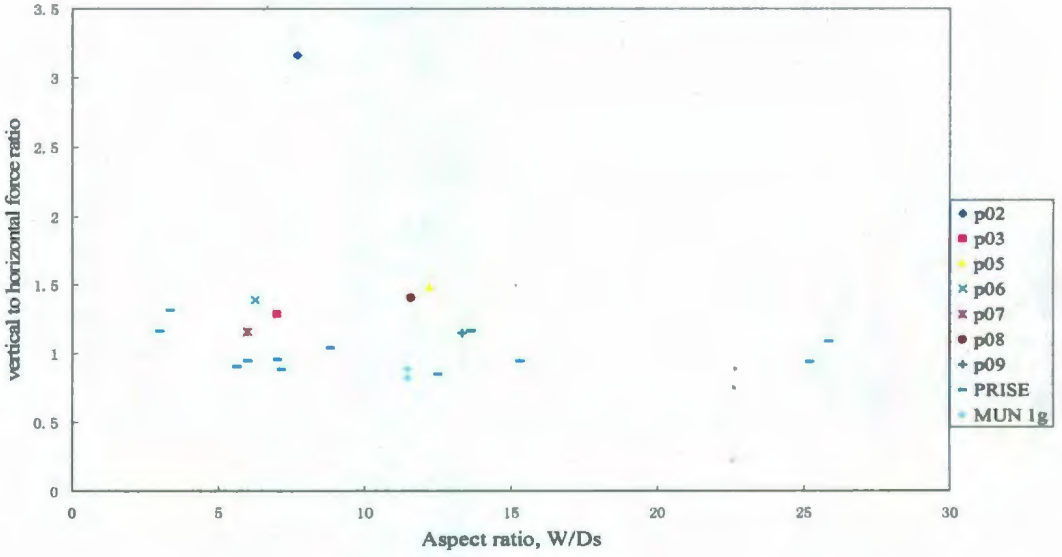

Figure 6-10 Comparing force ratio to the aspect ratio with PRISE and MUN 1g test 1990

Compared with the PRISE centrifuge sand test and Memorial University 1g Physical Model Sand Test, Figure 6-10, the average force ratio of test P03 through to P09 is higher than the average force ratio of the PRISE test and the MUN test. All the data are plotted in a narrow area in Figure 6-10, which indicated that there is no effect of the aspect ratio on the force ratio and the attack angle. The high density dry sand test, P02 shows about double force ratio that for other tests.

6.6 Comparison with Medium Scale Tests

Table 6-4 compares the Delft Hydraulic (DH) flume tests, Vershinin et al. (2007), with PIRAM tests P05 and P08. The gouge depths of the DH tests are around 0.2m which is shallower than most of the PIRAM and PRISE tests. Comparing P05, P08 and DH Run2 tests, the attack angle are all 30 degrees. All equivalent gouge depths and widths are the same. The DH tests were in water saturated fine sand. P05 and P08 used the viscous fluid. Figure 6-11 is the comparison of the maximum horizontal deformation for prototype between P05, P08 and DH Run2 tests. Although the subgouge deformations have the consistent shape, P05 and P08 have a deeper extent. This difference may be partly because of the smaller ice keel displacement which means DH Run2 tests may not reach the steady state and the limit of 9 gouge depths of sand below the keel in DH tests.

Table 6-4 Comparison of the DH test Run 2 and PIRAM test P05 and P08

Test I.D.	Attack angle, α (deg)	Dr%	Gouge Depth, Ds (m)	Gouge Width, W (m)	Speed, mm/sec	F_v/F_h	kappa	Bearing pressure kPa	Max SGD m	SGD extent m
Run 2 -1	30	55	0.19	2.2	13	1.39	1.55	64	0.02	0.4
Run 2 -2	30	55	0.19	2.2	12	1.27	2.51	75	0.085	0.25
Run 2 -3	30	65	0.19	2.2	20	1.45	2.85	147	0.03	0.25
P05	30	58	0.18	2.2	1.1	1.5	3.6	46	0.07	0.7
P08	30	68.1	0.19	2.2	55	1.3	3.89	123	0.08	0.7

Figure 6-12 shows the forces ratio versus the combined depth. The depth values increased during the 3 stages of the DH Run2 tests which indicated that the frontal mound were accumulated during the 3 stages of the DH Run2 tests. It means that steady state conditions were not achieved in each DH tests step which can explain the lower subgouge deformation than P05 and P08. PIRAM tests have a significant initial frontal berm before gouging and have higher gouge length to depth ratios.

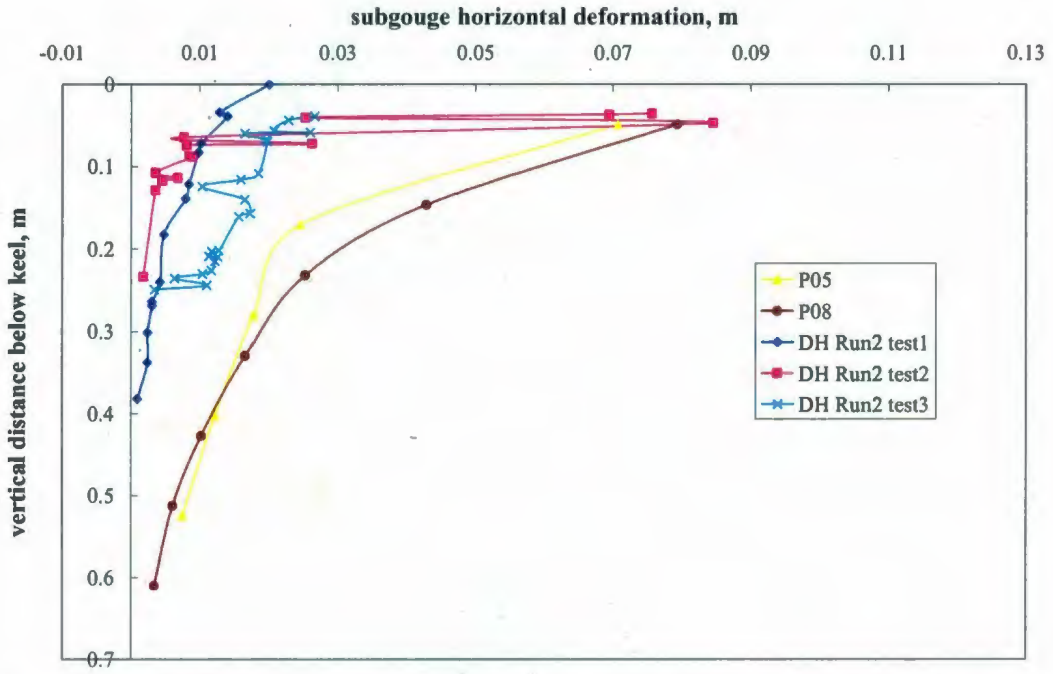

Figure 6-11 Horizontal subgouge deformation of the DH test Run 2 and PIRAM test P05 and P08

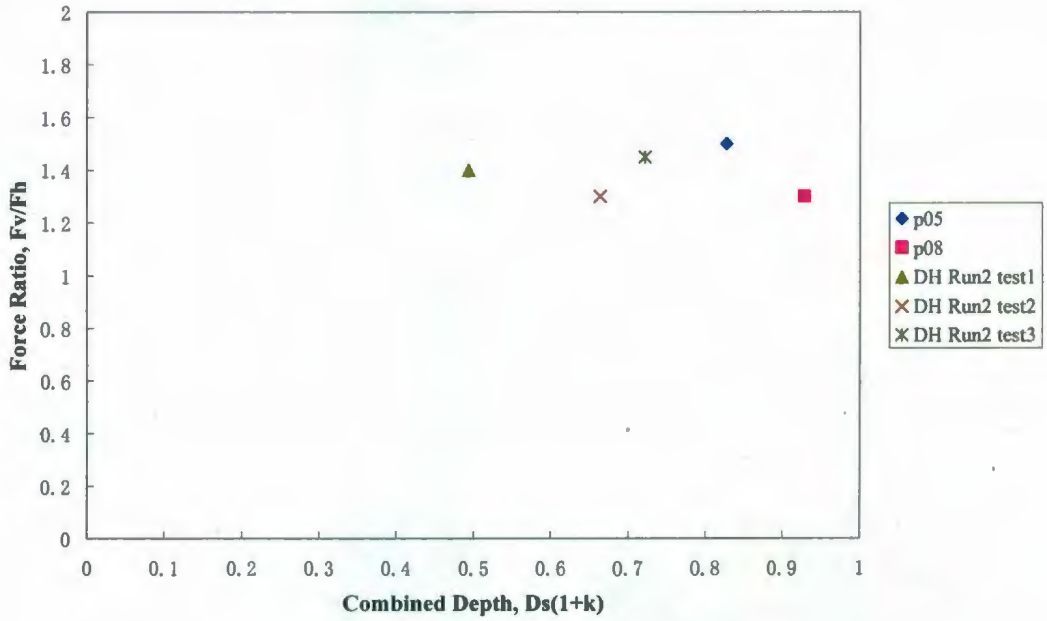

Figure 6-12 Force ratios of the DH test Run 2 and PIRAM test P05 and P08

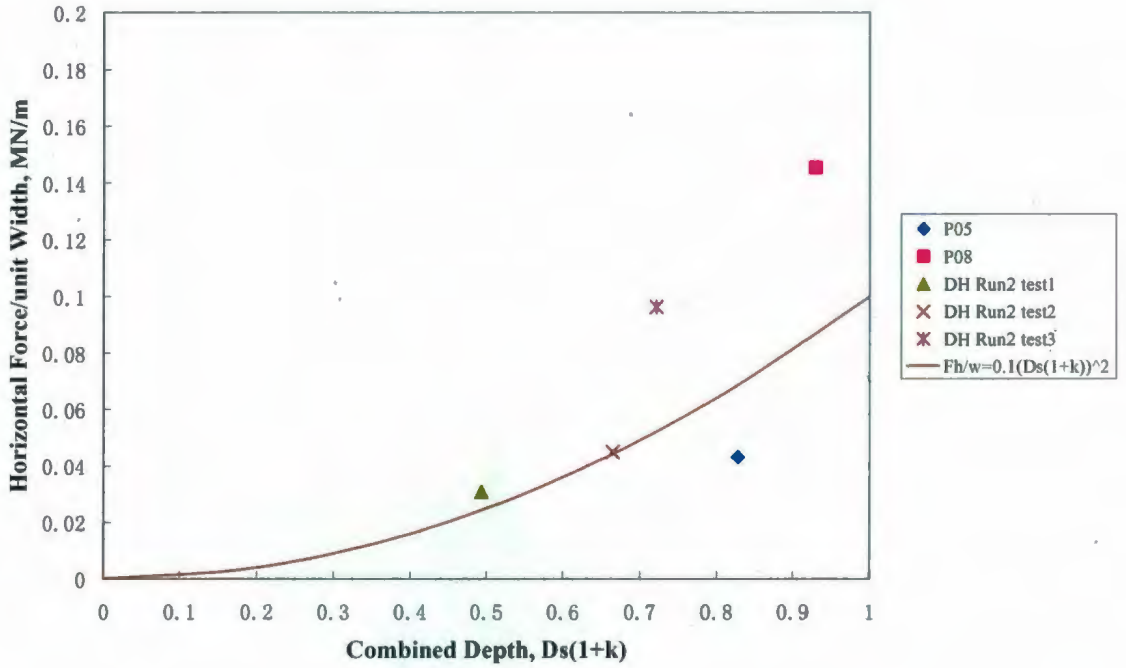

Figure 6-13 Gouge force per unit width versus combined depth between DH Run2 and PIRAM tests P05 and P08

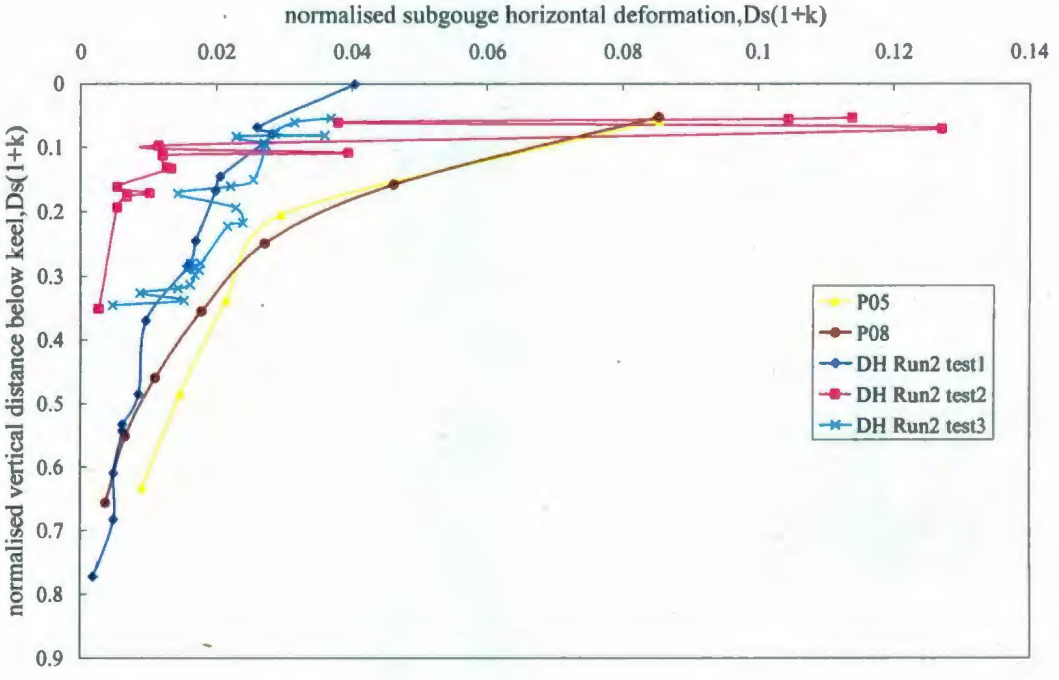

Figure 6-14 Normalized horizontal subgouge deformation of the DH Run 2 and PIRAM test P05 and P08

Figure 6-13 is the gouge force per unit width versus the combined depth which shows that the combined depths have a significant influence on the gouge forces. The horizontal gouge force seems to increase with combined depth squared. As the combined depth is an important parameter in assessing the gouge force and the subgouge deformation. Figure 6-14 is the normalized horizontal subgouge deformation by combined depth between DH Run2 tests and PIRAM tests P05 and P08. It shows that the subgouge deformations have the consistent profile. The vertical extent for both PIRAM tests and DH Run2 tests are up to 0.8 as the vertical extent is related to the combined depth.

6.7 Subgouge Deformation

Figure 6-15 shows the maximum horizontal subgouge deformation profile of all the PIRAM tests. Figure 6-16 is the maximum horizontal subgouge deformation profile in prototype. Figure 6-17 is the subgouge deformation normalized by the combined depth. All the three figures shows that the tests have consistent profile. P09 has the larger horizontal deformation because the attack angle is 15 degree.

Figure 6-18 is the comparison of the normalized horizontal subgouge deformation of PIRAM tests and PRISE tests. The tests profiles are all consistent. Most of the PIRAM tests have the attack angle of 30 degree except P09 is 15 degree. Most of the attack angle of PRISE test is 15 degree. The maximum horizontal subgouge deformation for PRISE tests is larger than most of PIRAM tests.

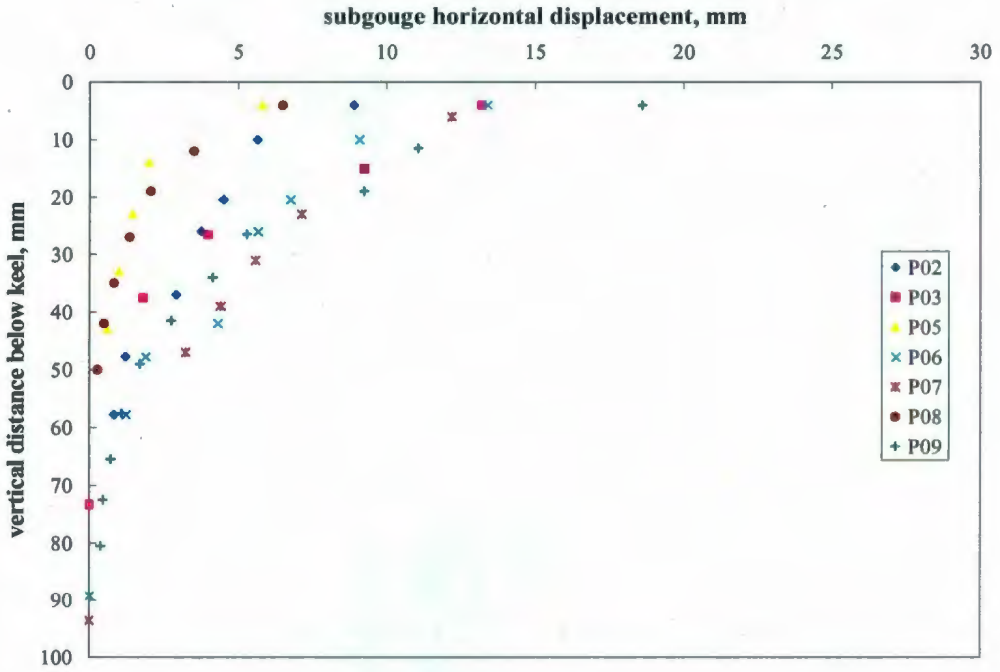

Figure 6-15 PIRAM model subgouge horizontal displacement profiles

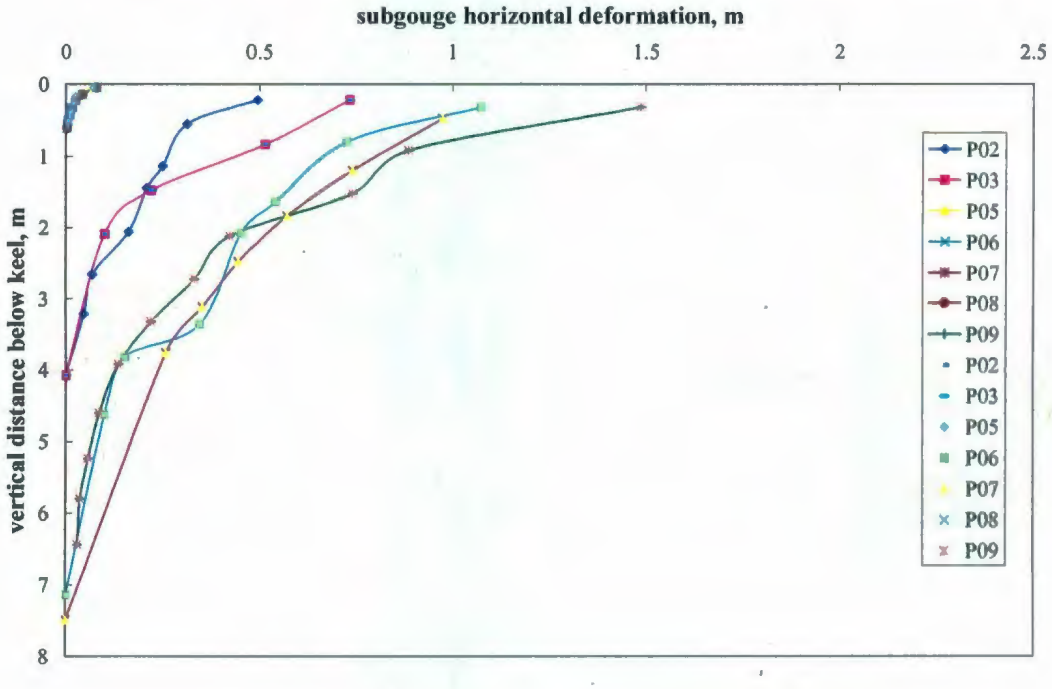

Figure 6-16 PIRAM prototype subgouge horizontal displacement profiles

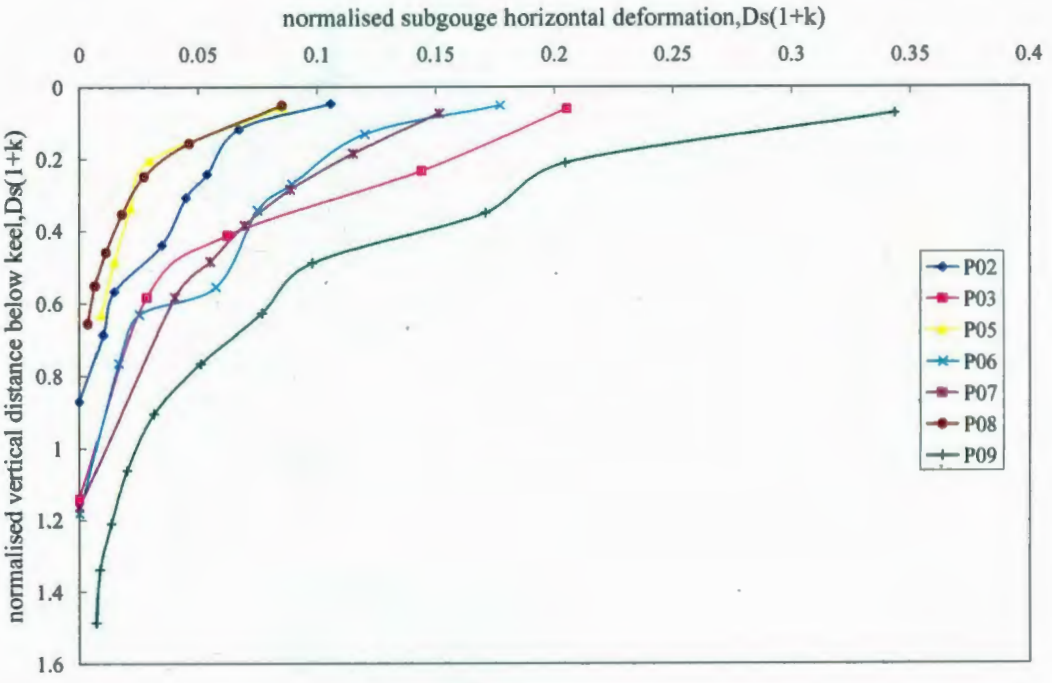

Figure 6-17 Normalized PIRAM prototype subgouge horizontal displacement profiles

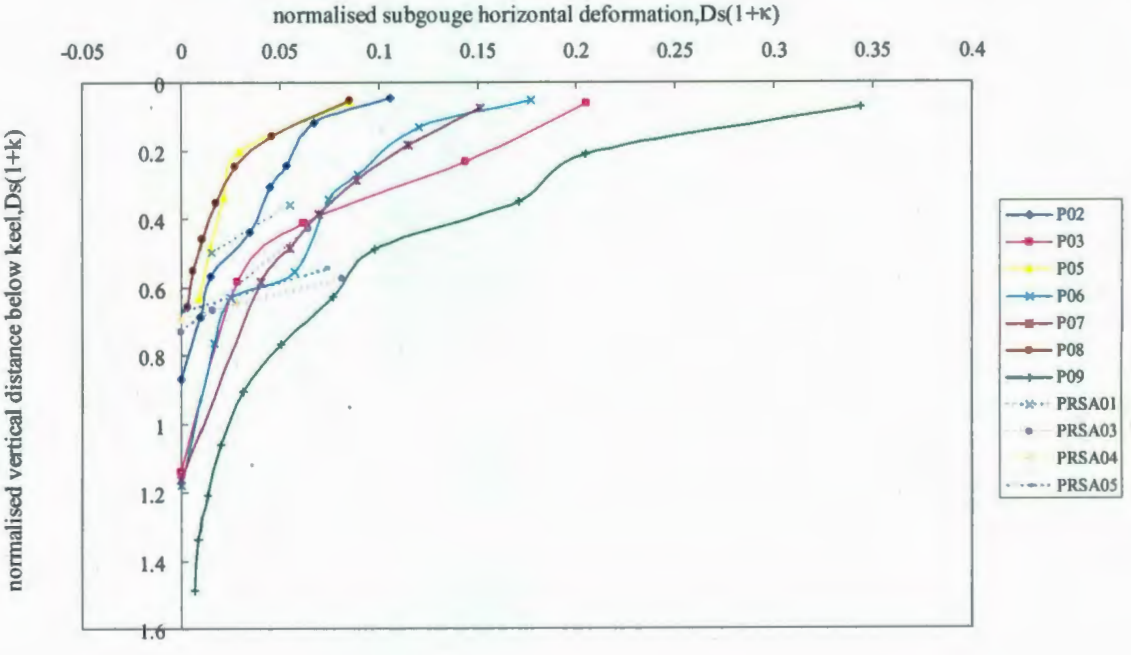

Figure 6-18 Normalized PRISE and PIRAM model subgouge horizontal displacement profiles

Phillips et al. (2005) used the relative dilation index, I_r, as an approximate descriptor for the sand state during the gouging event. The dilation index is defined as:

$$I_r = D_r \cdot (10 - \ln \sigma_b) - 1$$

where, σ_b is the bearing pressure in MPa and D_r is the relative density. The vertical extent of the subgouge deformation, Table 6-5, is related to the combined depth and the soil state.

Figure 6-19 considers the vertical extent of subgouge deformation with dilatancy index, I_r for previous tests C-CORE (2008). The maximum vertical extent is around a dilation index of 1. Figure 6-20 C-CORE (2008) is the normalized subgouge horizontal displacement by measured vertical extent with the dilation index. The normalized displacement value represents the shear strain of the subgouge deformation. It indicated that the tests with higher attack angle of 30 degree have the lower magnitude of subgouge deformation than the tests with 15 degree.

C-CORE(2008) developed the empirical relationship for subgouge deformation from reduced-scale model tests with uniform soil condition. The empirical functions are used to define the magnitude and spatial extent of subgouge deformation. The subgouge relationship parameters are shown in Table 6-6. Equations 6.1 are the empirical functions for sand C-CORE (2008). To accommodate the PIRAM tests, equation 6.1 has been revised to equation 6.2, C-CORE (2009e).

Table 6-5 Sand test results in prototype parameters

Gouge	P02	P03	P05	P06	P07	P08	P09
Angle(degrees)	30	30	30	30	30	30	15
Depth(m)	1.3	1.43	0.18	2.3	2.4	0.19	1.2
Width(m)	10	10	2.2	14.4	14.4	2.2	16
Dr	93.6	51.5	58	50.8	39	68.1	38.6
Fv(MN)	25.3	9.9	0.14	65.2	52.5	0.45	32.4
Fh(MN)	8	7.7	0.095	47	45.4	0.32	28.2
Fv/Fh Ratio	3.15	1.28	1.5	1.39	1.28	1.3	1.15
Speed (mm/s)	0.5	0.5	1.1	1.1	5.5	54.6	56.8
Mound height(m)	3.38	2.145	0.648	3.749	4.032	0.739	3.132
Combined height(m)	4.68	3.575	0.828	6.049	6.432	0.929	4.332
Vertical extent(m)	4.07	3.86	0.53	7.14	7.49	0.54	6.51
Ir	3.1	1.5	2.6	0.97	0.6	2.5	0.94

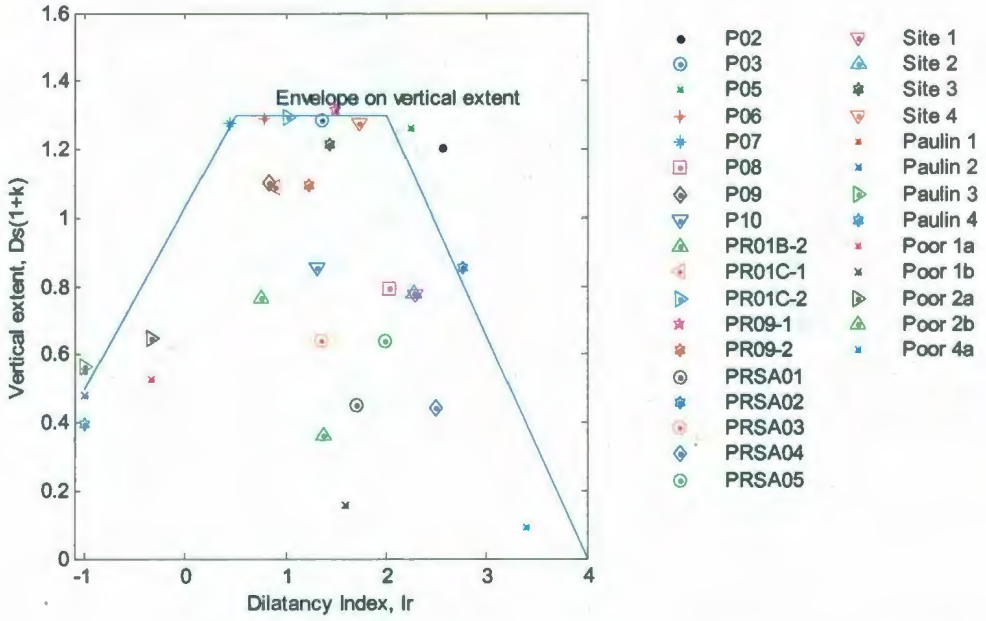

Figure 6-19 PIRAM model subgouge horizontal displacement profiles C-CORE (2008)

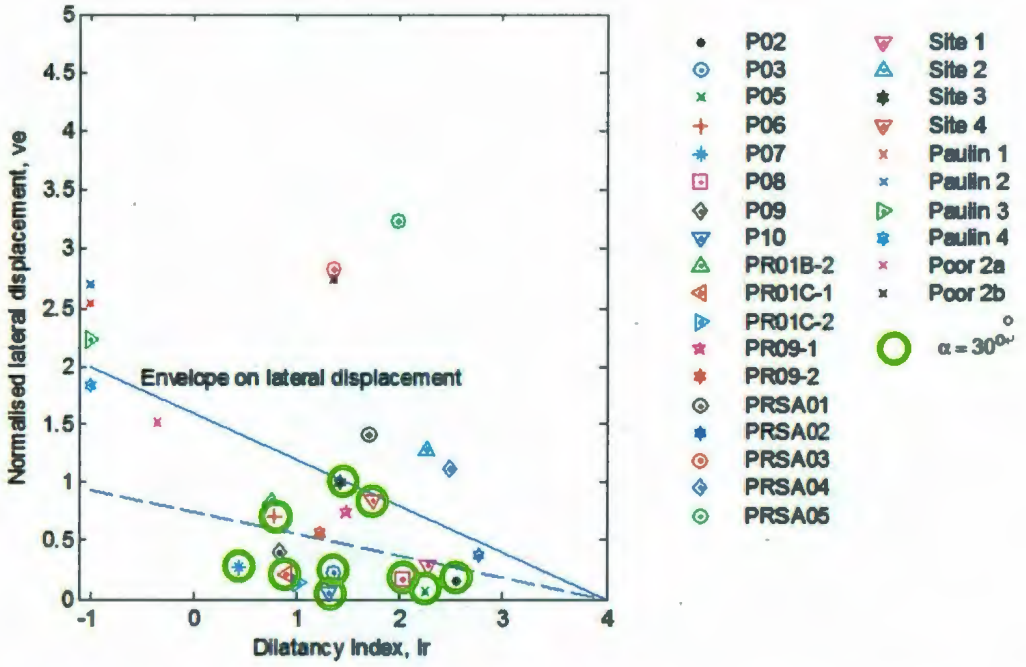

Figure 6-20 PIRAM model subgouge horizontal displacement profiles C-CORE (2008)

Table 6-6 Subgouge relationship parameters

Parameter	**Symbol**	**Units**
Gouge width	W	M
Gouge depth	D_s	M
Gouge angle	α	Deg
Sand relative density	RD	0-1
Soil displacement magnitude	D	M
Soil displacement on ice gouge centerline at ice keel base	d_o	M
Horizontal soil displacement on ice gouge centerline at ice keel base	d_{ho}	M
Vertical soil displacement on ice gouge centerline at ice keel base	d_{vo}	M
Vertical extent of subgouge deformations	V	M
Maximum vertical extent of subgouge deformations	v_e	M
Transverse horizontal distance from ice gouge centreline	Y	M
Atmospheric pressure	p_a	MPa

Equation: 6.1 C-CORE(2008)

$$\sigma_b(MPa) = 0.09\ D_s^{1.5}$$

$$I_r = RD^*(10 - \ln(\sigma_b^*1000)) - 1$$

$$v_e = \min[(1+ v_{ds}(I_r-2))\ (D_s + W/3),\ 5D_s] \text{ or } 0 \text{ if } I_r > 4$$

$$v_{ds} = -0.5 \text{ for } I_r > 2 \text{ and } = 0.2 \text{ for } I_r < 2$$

$$d_{ho}\ \text{sqrt}(\sigma_b/p_a)\ /v_e = 2-0.4\ (I_r+1) \quad > 0$$

$$d_{vo} = \min[D_s, W/6]$$

$$d/d_o = [1- v/v_e]^2$$

p_a = atmospheric pressure, 0.1 MPa

Equation 6.2 C-CORE(2009e)

$$\sigma_b(MPa) = 0.09\ D_s^{1.5}$$

$$I_r = RD^*(10 - \ln(\sigma_b^*1000)) - 1$$

$$v_e = \min[(1+0.5I_r)\ (D_s + W/5),\ 1.3\ (D_s + W/5),\ 5D_s] \text{ if } I_r < 2$$

$$\min[(2.6+0.65(I_r-4))\ (D_s + W/5),\ 5D_s] \text{ if } 2 < I_r < 4 \quad , 0 \text{ if } I_r > 4$$

$$d_{ho}\ \text{sqrt}(\sigma_b/p_a)\ /v_e = (0.54\ /\ \tan\alpha)\ (1 - 0.2\ (I_r+1)) > 0$$

$$d_{vo} = \min[0.3(D_s +W/5), D_s, W/6]$$

$$d/d_o = [1- v/v_e]^2$$

p_a = atmospheric pressure, 0.1 MPa

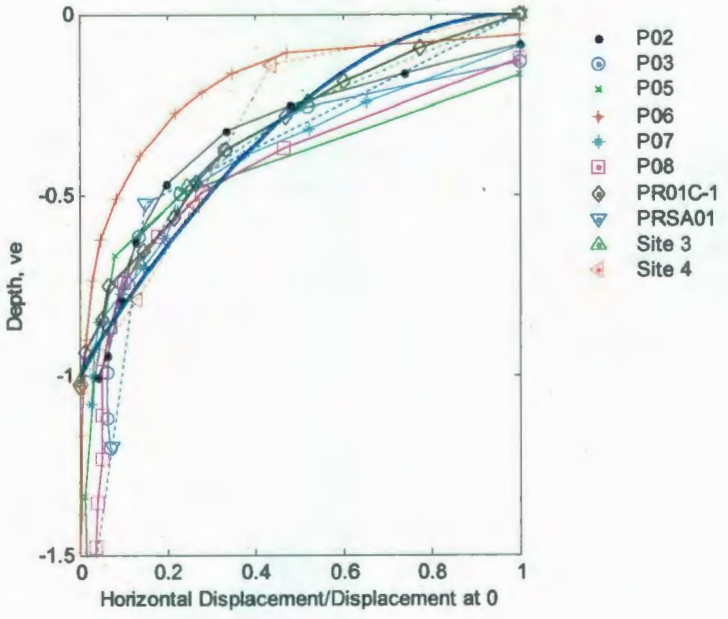

Figure 6-21 PIRAM model subgouge horizontal displacement profiles C-CORE (2009e).

Subgouge deformation for 30 degree tests are presented in Figure 6-21 C-CORE (2009e). The non-zero depth values for displacement of unity indicate those tests where SGD were not measured directly at the gouge base. These non-zero value profiles should be considered accordingly in evaluating the quadratic fit.

6.8 Gouge Rate

As shown in Table 6-4, P05 and P08 have the same attack angle of 30 degrees. Both the gouge depth and gouge width are about the same. The differences for P05 and P08 are the density (P08 is denser than P05) and the keel speed. Vertical and horizontal forces for P08 are about three times larger than those in P05. Force ratios for P05 and P08 are all around 1.45. The combined depth for P08 is higher than P05. The normalized subgouge deformation by combined depth for P08 has the same extent but smaller maximum horizontal subgouge deformation than P05, Figure 6-14. This difference may because of the sand dilatancy which is 2.5 for P08 and 2.6 for P05. Dilatancy is smaller in P08 because of the higher stain rate. This higher stain rate causes the smaller subgouge deformation and higher gouge forces from shear induced negative excess pore pressures ahead of the advancing keel.

Another comparison is between P09 in PIRAM tests and PR01C-2 in PRISE tests,

Table 6-7. P09 was using 30 cst viscous pore fluid and PR01C2 was using water saturated sand. The gouge depth, gouge width and soil condition are similar for P09 and

PR01C-2. The different gouge rates and pore fluids give normalized velocities, V*, of 1,100 and 25,500 mm^2/s using a non dimensional fluid viscosity for tests PR01C2 and P09 respectively. The dimensional relationship of normalized velocities was adopted to fconsider ice keel gouge rate in the experiments: V* = v D ν. In the above, D and v are the gouge depth and keel velocity, respectively, and ν is the pore fluid viscosity.

Gouge forces for P09 are 2.3 times larger than PR01C-2. Subgouge deformation for P09 and PR01C-2 is shown in Figure 6-22. P09 has smaller subgouge deformation than PR01C-2 which proves that higher gouge rate resulting smaller subgouge deformation and higher gouge forces. The two comparisons indicated that the faster gouge rate may result in larger gouge forces by a factor of 2 or 3 and smaller subgouge deformation but similar vertical extent.

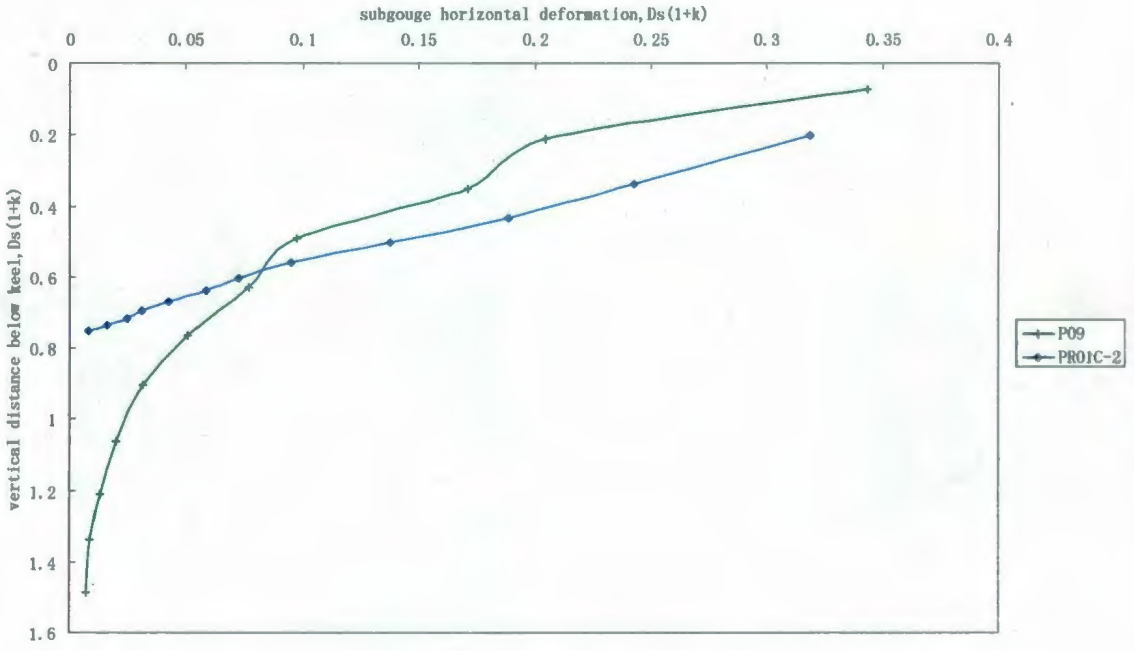

Figure 6-22 Subgouge deformation of the PIRAM test P09 and PRISE test PR01C-2

Table 6-7 Comparison of the PIRAM test P09 and PRISE test PR01C-2

Test I.D.	Attack angle Deg	Ir%	Gouge Depthm	Gouge Width M	Speed, mm/sec	F_v/F_h	Kappa	Bearing pressure kpa	Max SGD m	SGD extent m	Fh MN	Fv MN
P09	15	0.94	1.2	16	57	1.15	2.6	195	0.02	0.4	28.2	32.4
PR01C2	15	0.95	1.1	15	10	1.16	2.5	97	0.085	0.25	12.2	14.2

7 CONCLUSION AND RECOMMENDATIONS

When the base of an iceberg or pressure ridge ice keel is in contact with the seabed, an ice keel gouge may be formed. Researchers indicate some of the important factors that affect ice keel gouge such as soil resistance, ice strength, keel geometry and driving force. The ice gouge event can pose a significant threat on sub-sea facilities such as pipelines, cables, wellheads and also templates.

The experiment program is progressed by towing model ice keel across a model testbed at a set gouge depth in a geotechnical centrifuge. A large amount of data regarding ice keel gouge in sand was acquired from the experiment program and analysis described in this thesis.

A total of seven tests were conduced in this experiment program. The two first model tests were conducted relatively slowly in dry, dense, and water-saturated medium density sand to prove the new equipment and techniques. Two tests are included to compare with previous Delft Hydraulics flume medium scale gouge tests. Three tests are conducted with faster gouge rates using a viscous pore fluid to retard excess pore pressure dissipation.

As the model ice keel is driven in the sand, the soil reaction force increase with the development of a deep seated bearing failure mechanism. As the mechanism is overridden, the load decreases with a corresponding clearing process. These load cycles have been correlated in all tests to the failure mechanism using PIV.

The combined gouge depth has a significant effect on the force and subgouge deformation. The force per unit width increases as the combined gouge depth becomes larger. The vertical to lateral gouge force ratio seems independent of aspect ratio or attack angle. The kappa value which is the frontal bern height normalized by gouge depth is linear with the aspect ratio for deep gouge depth. It seems there is no significant effect for the kappa value between 15 degree and 30 degree for deep gouge depth. Kappa value has the significant effect of gouge force and subgouge deformation.

PIV techniques were successfully used to track the evolution of subgouge deformation for all 7 tests. The maximum horizontal subgouge displacement happens at the base of the keel and decreases with depth. The associated maximum gouge forces are a function of the keel attack angle and the gouge geometry.

As compared with previous tests, the vertical extent of subgouge deformation is a function of combined depth and the soil state, but independent of the attack angle. The lateral SGD deformations are influenced by the attack angle and the soil state. The faster gouge rate may result in larger gouge forces by a factor of 2 or 3 and smaller subgouge horizontal deformation but similar vertical extent.

As there are only 7 tests presented in this thesis, it has limitations in comparing between tests to evaluate the effect from some parameters. Such as the soil condition, soil strength parameters, parametric correlations and ice keel attack angle. More tests can be taken in order to validate the conclusions and provide more comparisons. As all the tests are using

the same fine sand, other soil condition and soil strength could be considered in future tests which may effect the attenuation of subgouge deformation and plastic strain of soil. There are 6 of 7 tests using model ice keel with attack angle of 30 degree. Ice gouging tests with other attack angles and keel shapes can be conducted to have more comparisons with 30 degree attack angle keel. Faster gouging rate tests can also be taken to evaluate the effect of gouge rate on subgouge deformation. The correlations between parameters should also be considered in future work. As combined depth has the significant effect on gouge force and sebgouge deformation, future studies should examine the extent of the dead wedge within the frontal berm, as well as the magnitude and rate of SGD attenuation.. Maximum vertical extent of subgouge deformations should be examined. Single keel versus multiple fingered keel ice gouging feature on the subgouge deformation should be examined in the future studies.

8 REFERENCES

[1]. Chari, T.R. (1979) "Geotechnical Aspects of Iceberg Gouges on Ocean Floors", Canadian Geotechnical Journal, Vol. 16, No. 2: 379-390.

[2]. Chari, T. R. (1975) "Some Geotechnical Aspect of Iceberg Grounding", PhD Thesis to the Faculty of Engineering and Applied Science, Memorial University of Newfoundland.

[3]. Clark, J.I., Paulin, M.J., Poorooshaab, F. (1990). "Pipeline Stability in an Ice-Scoured Seabed", EUROMS-90, August 20-22, 1990, Trondheim, Norway, pp. 533-549.

[4]. C-CORE (2009a) "PIRAM – Gouge Morphology Study", C-CORE Report R -09-013-490 v1, June 2009.

[5]. C-CORE (2009b) "PIRAM – Draft Final Report", C-CORE Report R -09-019-490 v1, June 2009.

[6]. C-CORE (2008) "PIRAM – Review of Subgouge Deformation", C-CORE report R-07-045-491 v2, December 2008.

[7]. C-CORE (1996) "PRISE Phase 3c: Extreme Ice Gouge Event - Modeling and Interpretation", C-CORE Report 96-C32

[8]. Comfort, G., and Graham, B. (1986) "Evaluation of Sea Bottom Ice Gouge Models", Environmental Studies Revolving Funds Report No. 037, June, 1986.

[9]. Hettiarachir, D.R.P., and Reece, A.R. (1975) "Boundary wedges in two-dimensional passive soil failure", Geotechnique 25, 197-220

[10]. Kenny, S., Phillips, R., Clark, J., and Nobahar, A. (2005) "PIRSE-Numerical Studies on Subgouge Deformations and Pipeline/Soil Interaction Analysis".J.I. Clark and Associates , ST.John's, Canada

[11]. King, T., Phillips, R. and Barrett, J. (2008) "Probabilistic Pipeline Burial Analysis for Protection against Ice Scour", ICETECH-08, July 20-23 in Banff, Canada.

[12]. Liferov, P. (2003) "First-year Ice Ridge Gouge and some Aspects of Ice Rubble Behavior", Doctoral Thesis at NTNU 2005:84

[13]. Lanan, G.A., Niedoroda, A.W., and Week, W.F. (1986) "Ice Gouge Hazard Analysis",

Proceedings, 18th Annual Offshore Technology Conference, OTC, Volume 4, Houston, TX, USA, pp.57-66.

[14]. Palmer, A. Konuk, I., Love, J., Been, K., and Comfort, G. (1989) "Ice stour mechanisms . Proceedings", Tenth International Conference on Port and Ocean Engineering under Arctic Conditions Lulea, 123-132

[15]. Palmer, A.C., Konuk, I., Comfort, G. (1990) "Ice Gouging and the Safety of Marine Pipelines", Paper OTC6371 in Proceedings, Twenty-second Offshore Technology Conference

[16]. Palmer, A.C., Kenny, J.P., Perera, M.R. and Reece, A.R. (1979) "Design and operation of an underwater pipeline trenching plough", Geotechnique, 29, 305-322

[17]. Paulin, M.J. (1992) "Physical Modeling Analysis of Iceberg Gouge in Dry Sand and Submerged Sand", M. Eng. Thesis, Memorial University of Newfoundland, St.John's, NF, Canada, 183p

[18]. Poorooshasb, F. (1990). "Analysis of Subgouge Stresses and Probability of Ice Gouge-Induced Damage for Buried Submarine Pipelines". Contract Report for Fleet Technology Ltd., C-CORE Contract Number 89-C15.

[19]. Phillips, R., Clark, J.I., and Kenny, S. (2005) "PRISE Studies on Gouge Forces and Subgouge Deformations", Proc., 18th POAC, 10p.

[20]. Rinawi, W. (2004)." Particle Image Velocimetry (PIV) applied on triaxial tests", MSc. thesis, Institut fur Geotechnik und Tunnelbau, Universitat Innsbruck.

[21]. Surkov, G. A. (1995) "Method for Determining the Optimum Burial Profile for Subsea Pipeline Facilities in Freezing Seas. Dissertation for a Degree of Candidate of Technical Services", Sakhalin Research and Design Institute.

[22]. Taylor, R.N. (1995) "Geotechnical Centrifuge Technology", Blackie Academic Press.

[23]. Timco, G.W. and Burden, R.P. (1997) "An Analysis of the Shapes of Sea Ice Ridges", Cold Regions Science and Technology, 25: 65–77.

[24]. Vershinin, S.A, Truskov, P.A, and Liferov, P.A. (2007) "The action of ice formations on the underwater objects". In Russian, 196 pages.

[25]. Weeks, W.F., Barnesr, P.W., Rearic, P.M. and Reimnitz, E. (1983) "Statistical Aspects of Ice Gouging on the Alaskan Shelf of the Beaufort Sea" U.S. Army Cold Regions Research and Engineering Lab. Report 83-21, 34 pps.

[26]. White, D.J., Take, W.A. and Bolton, M.D. (2003) "Soil deformation measurement using particle image velocimetry (PIV) and photogrammetry", Geotechnique 53 7:619-631.

[27]. Woodworth, C., Nixon, D., and Phillips, R. (1996) "Subgouge Deformations and the Security of Arctic Marine Pipelines", Offshore Technology Conference

Appendix A

Table A 1: Site centrifuge sand test program prototype parameters

Test	Soil Type	Relative Density	Attack Angle (deg.)	Gouge Depth (m)	Gouge Width (m)	Fh (MN)	Fv (MN)
Site 1	Fine Sand	62%	15	1.0	15	13	16.4
Site 2	Fine Sand	73.9%	15	1.9	10	23.6	28
Site 3	Fine Sand	56.2%	30	2.05	10	15	14
Site 4	Fine Sand	71.8%	30	2.75	10	27.8	30.3

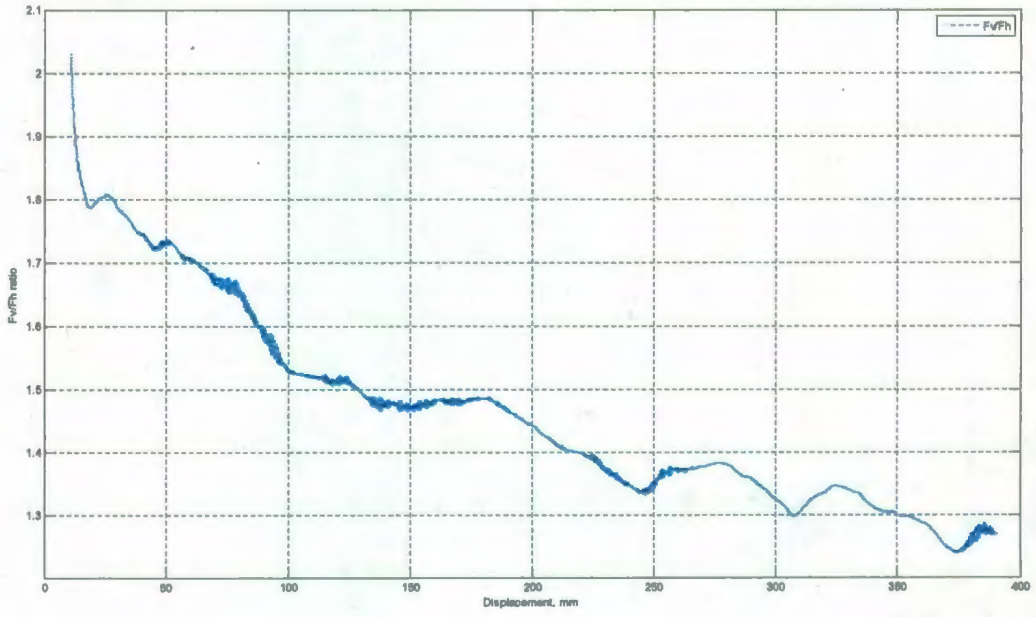

Figure A. 1 Model Fv/Fh ratio versus ice keel displacement for test P03

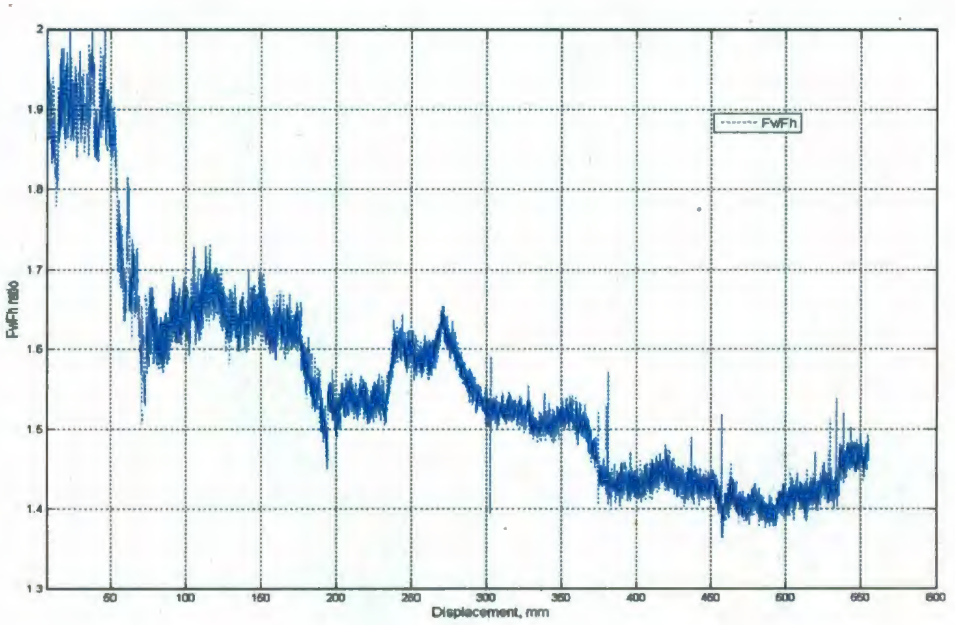

Figure A. 2 Model Fv/Fh ratio versus ice keel displacement for test P05

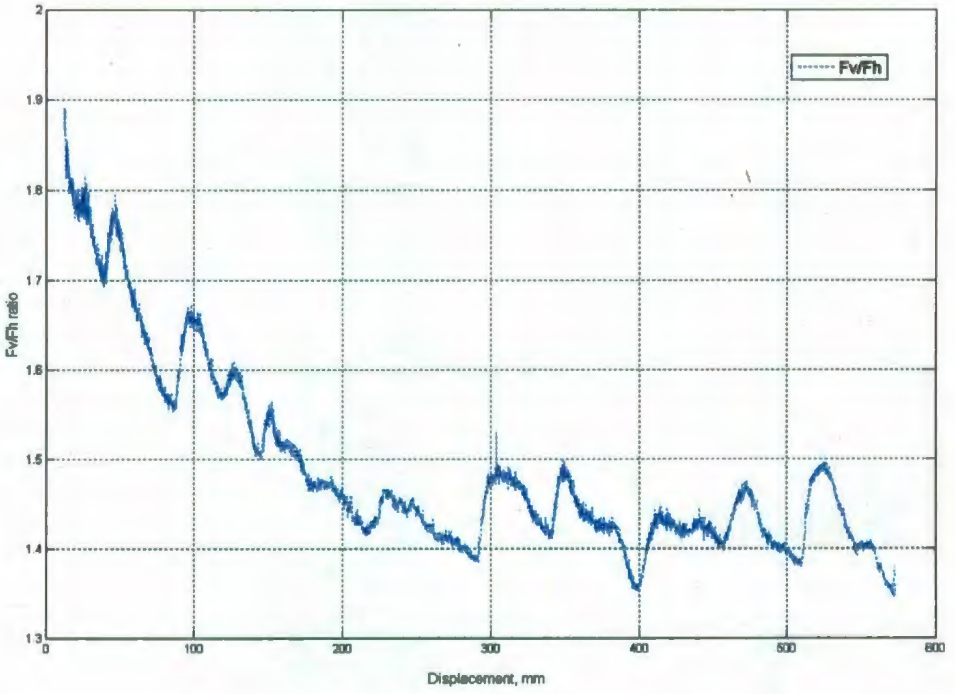

Figure A. 3 Model Fv/Fh ratio versus ice keel displacement for test P06

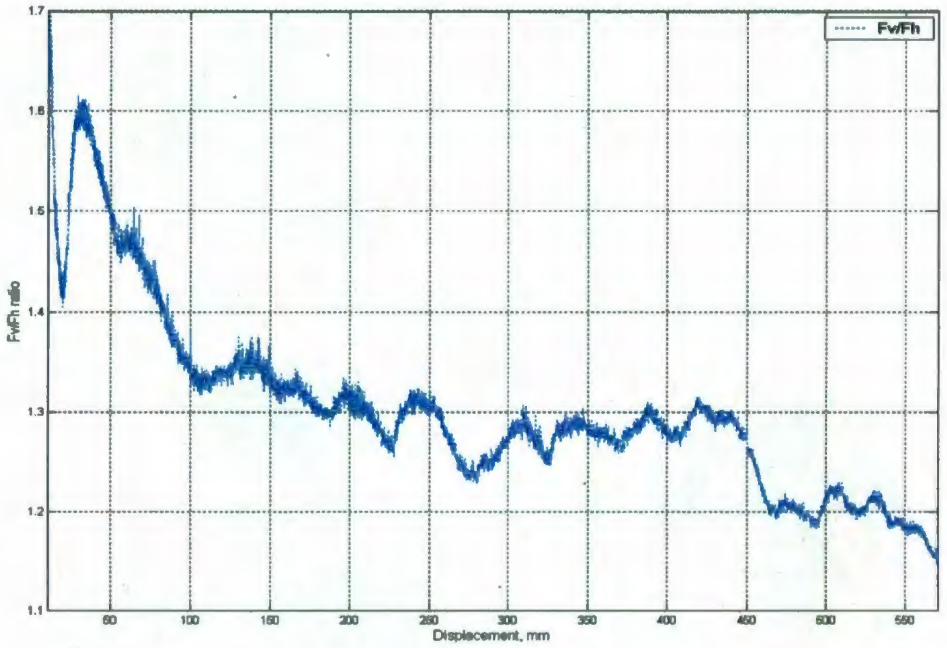

Figure A. 4 Model Fv/Fh ratio versus ice keel displacement for test P07

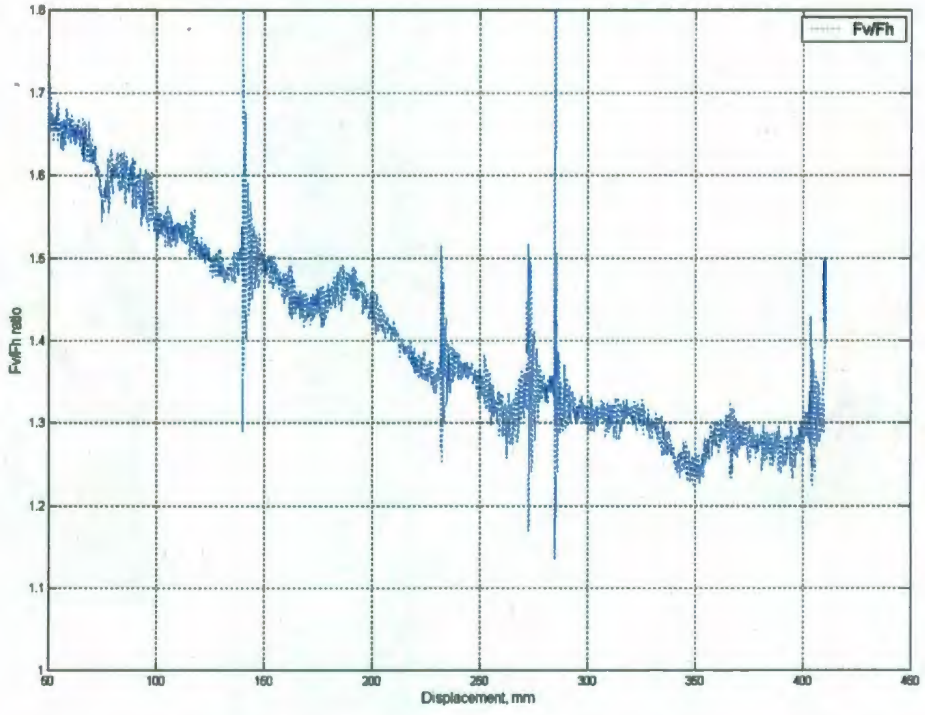

Figure A. 5 Model Fv/Fh ratio versus ice keel displacement for test P08

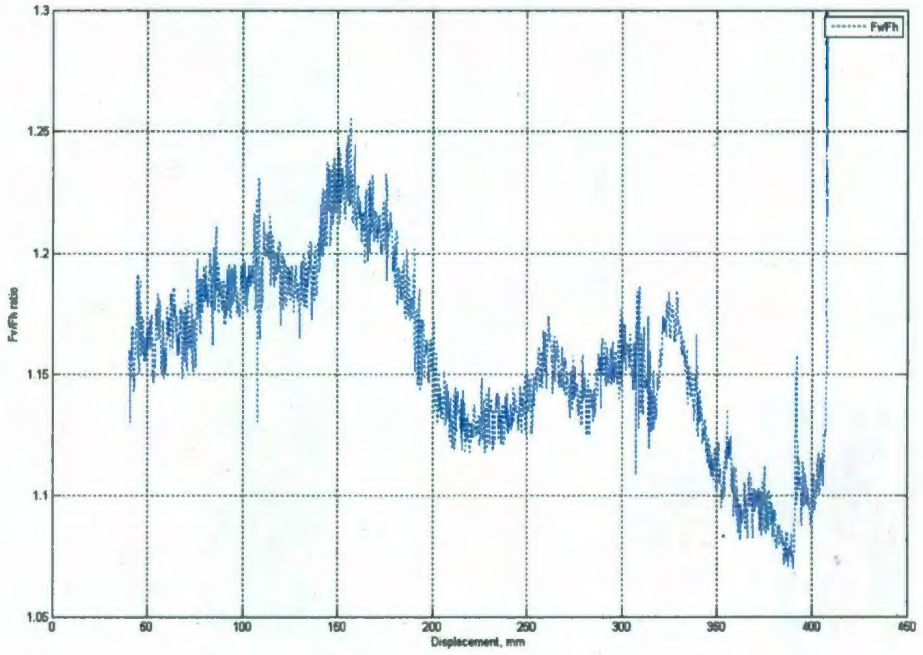

Figure A. 6 Model Fv/Fh ratio versus ice keel displacement for test P09

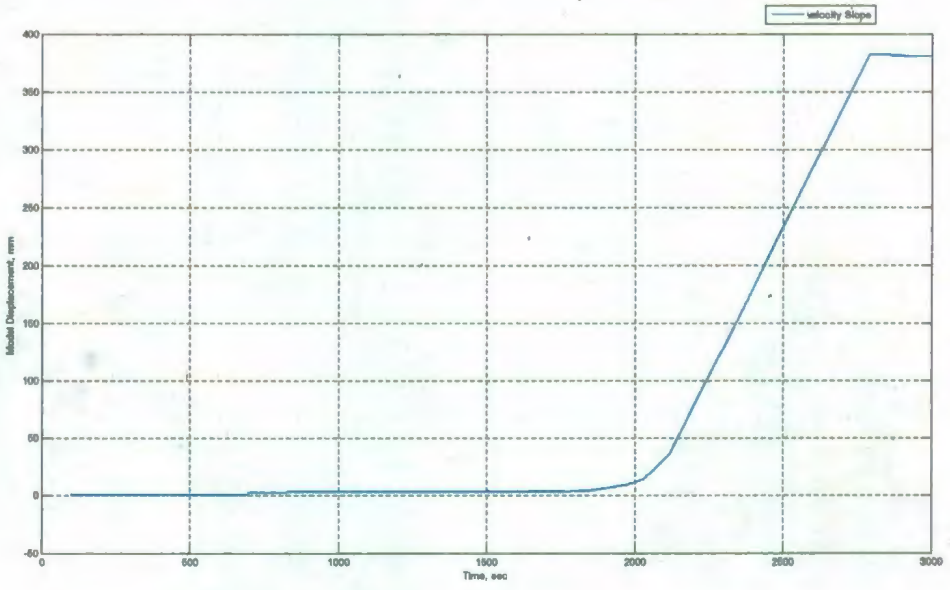

Figure A. 7 Model velocity slope for test P02

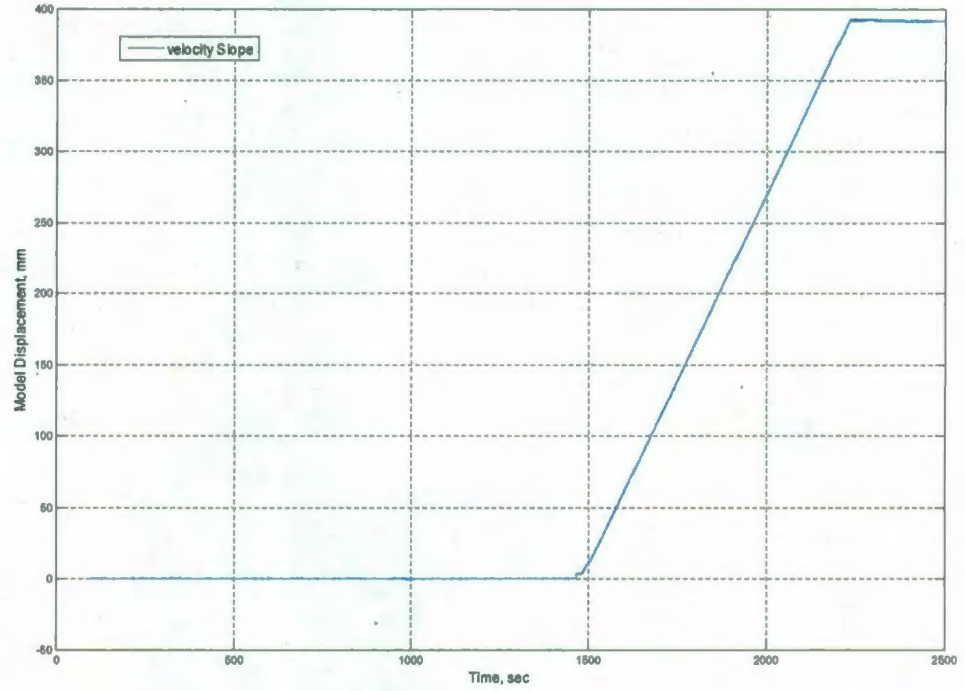

Figure A. 8 Model velocity slope for test P03

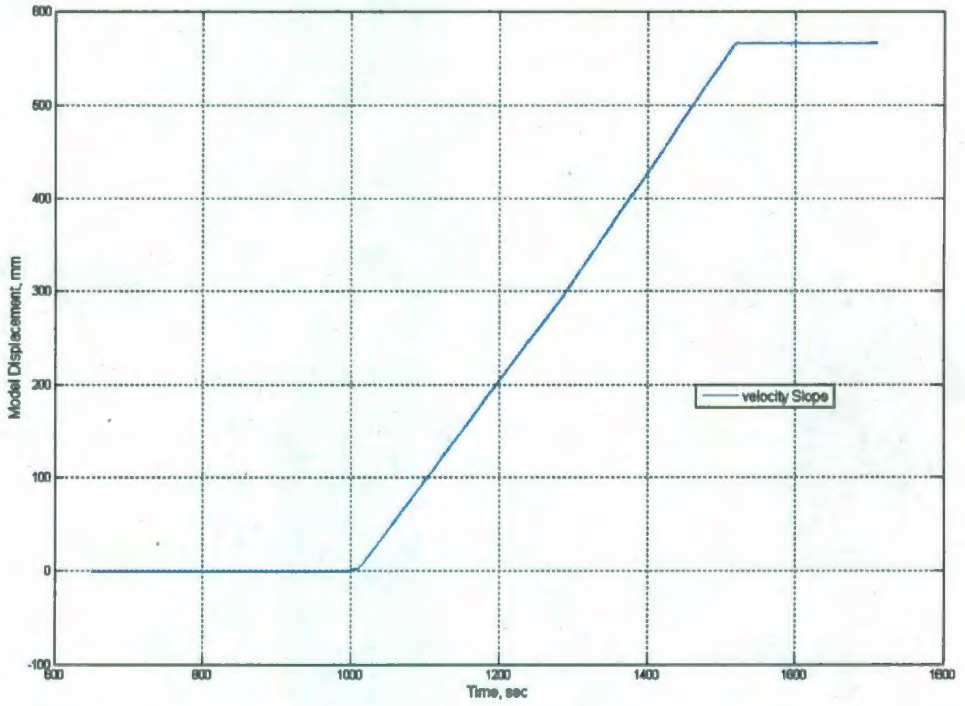

Figure A. 9 Model velocity slope for test P05

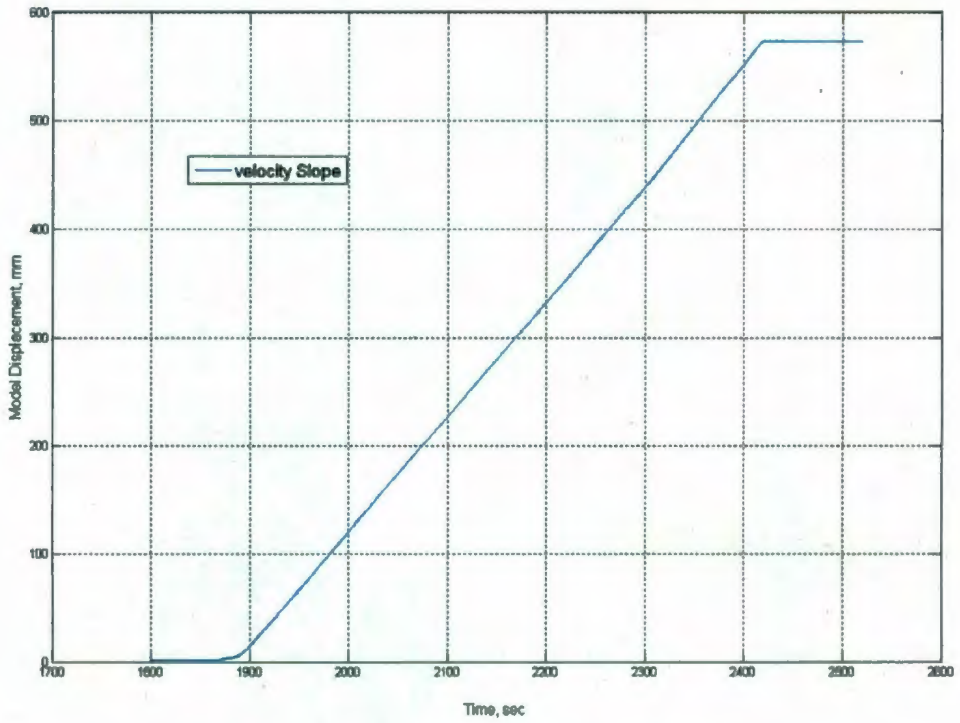

Figure A. 10 Model velocity slope for test P06

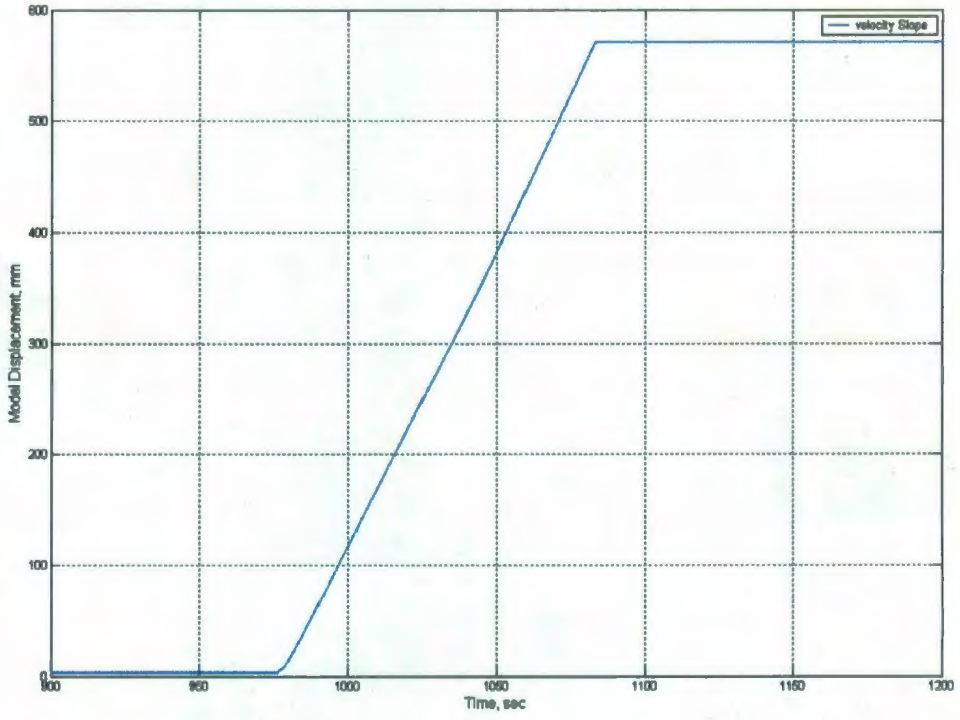

Figure A. 11 Model velocity slope for test P07

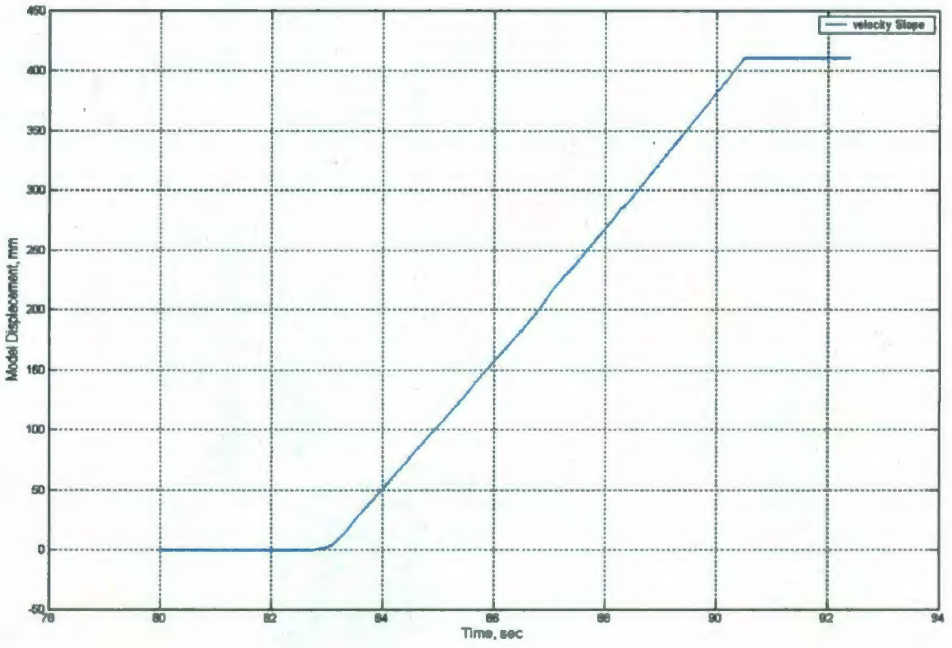

Figure A. 12 Model velocity slope for test P08

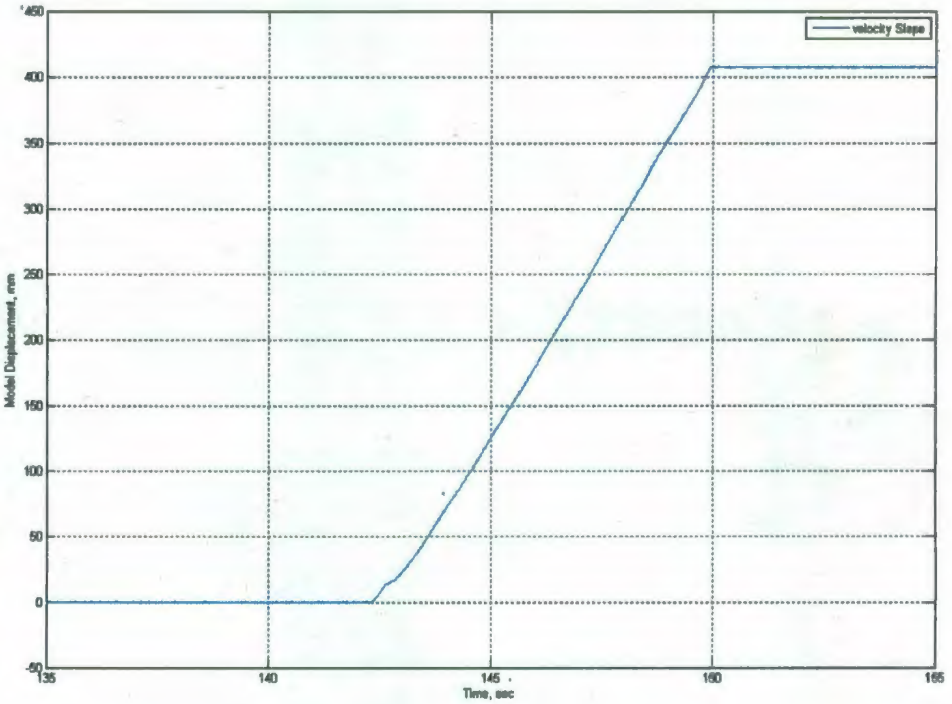

Figure A. 13 Model velocity slope for test P09

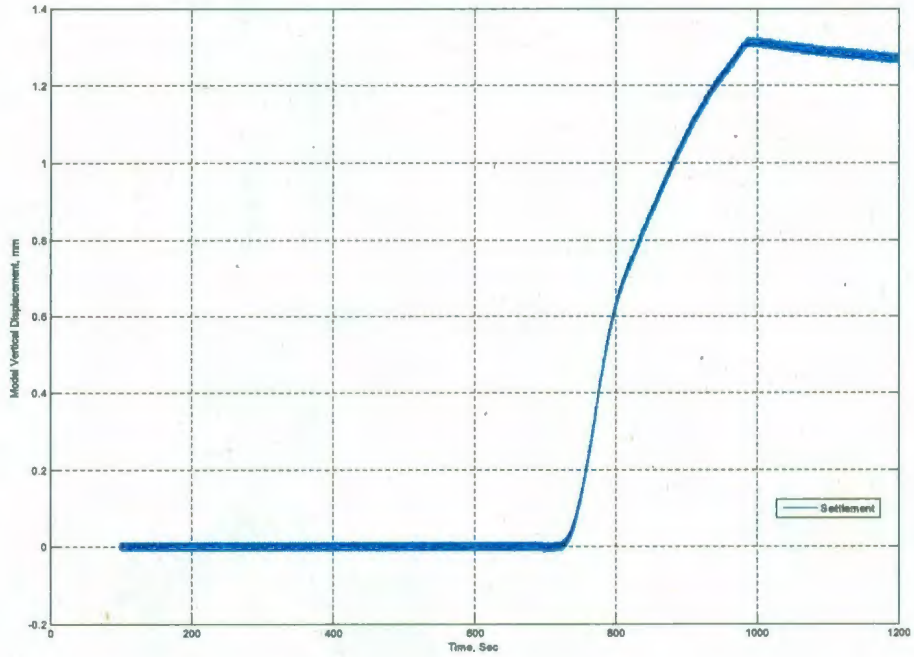

Figure A. 14 Model vertical settlement during centrifuge spin up for P02

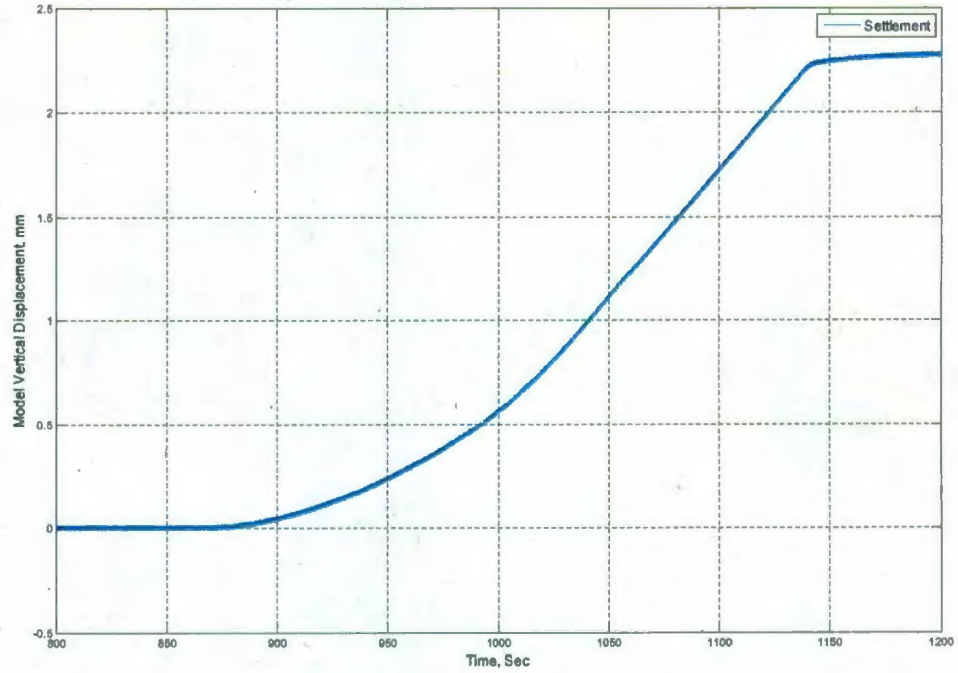

Figure A. 15 Model vertical settlement during centrifuge spin up for P03

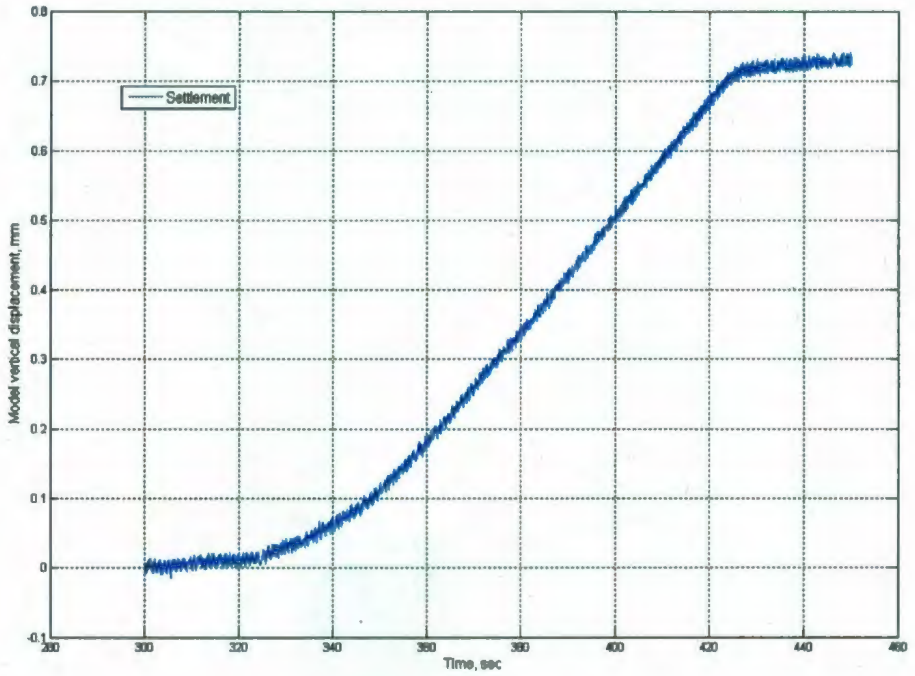

Figure A. 16 Model vertical settlement during centrifuge spin up for P05

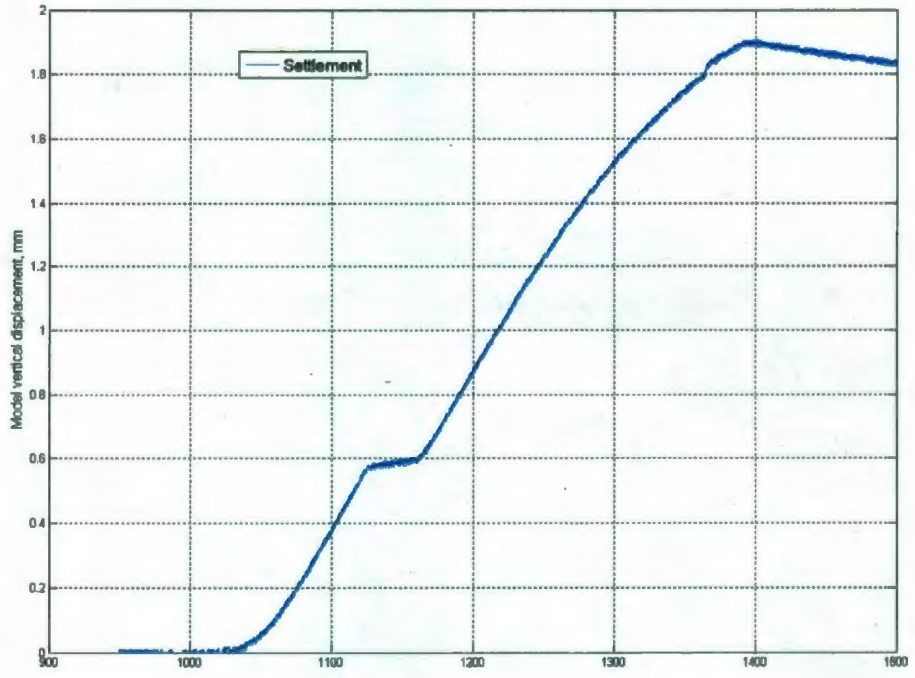

Figure A. 17 Model vertical settlement during centrifuge spin up for P06

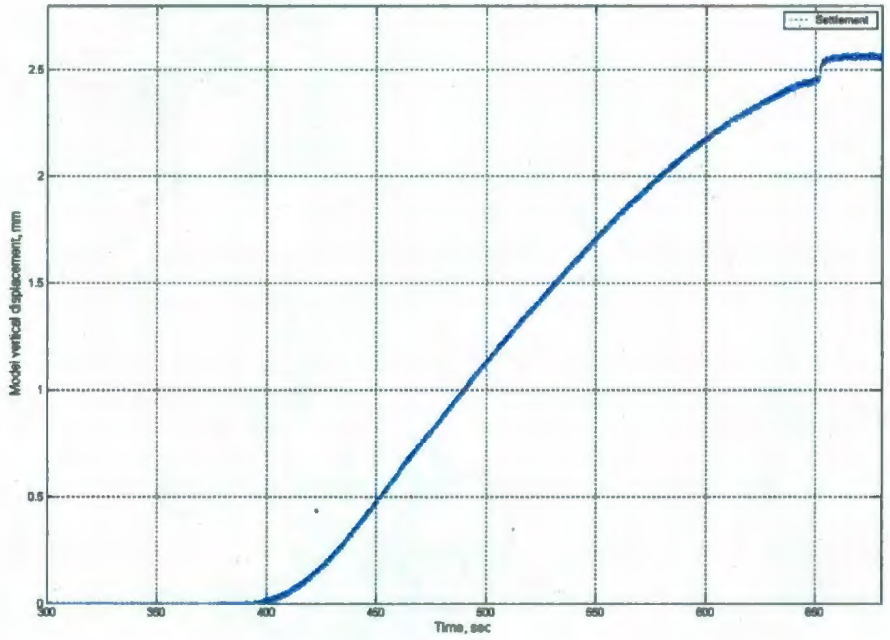

Figure A. 18 Model vertical settlement during centrifuge spin up for P07

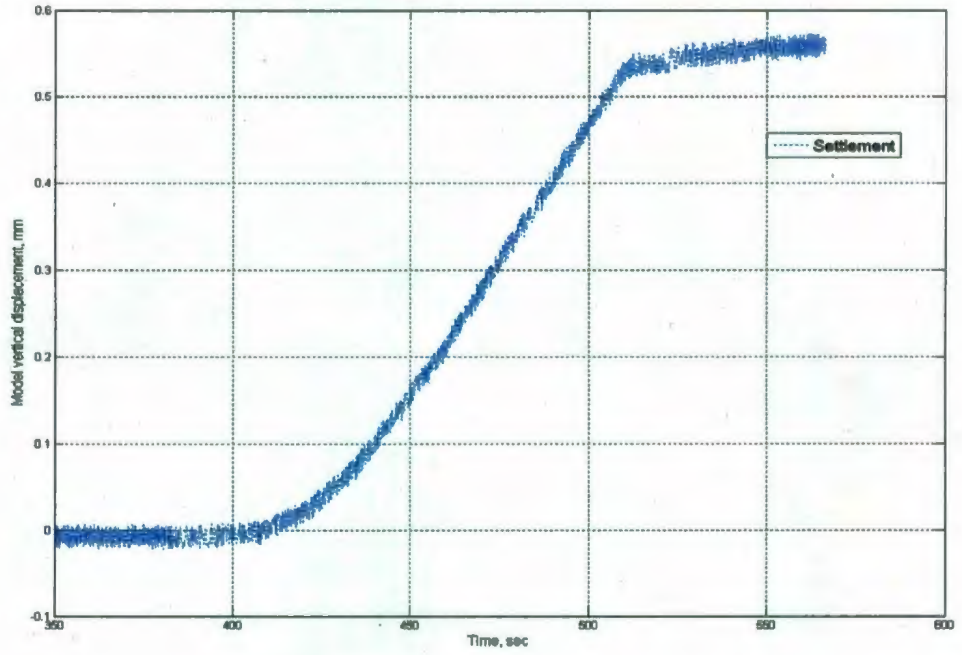

Figure A. 19 Model vertical settlement during centrifuge spin up for P08

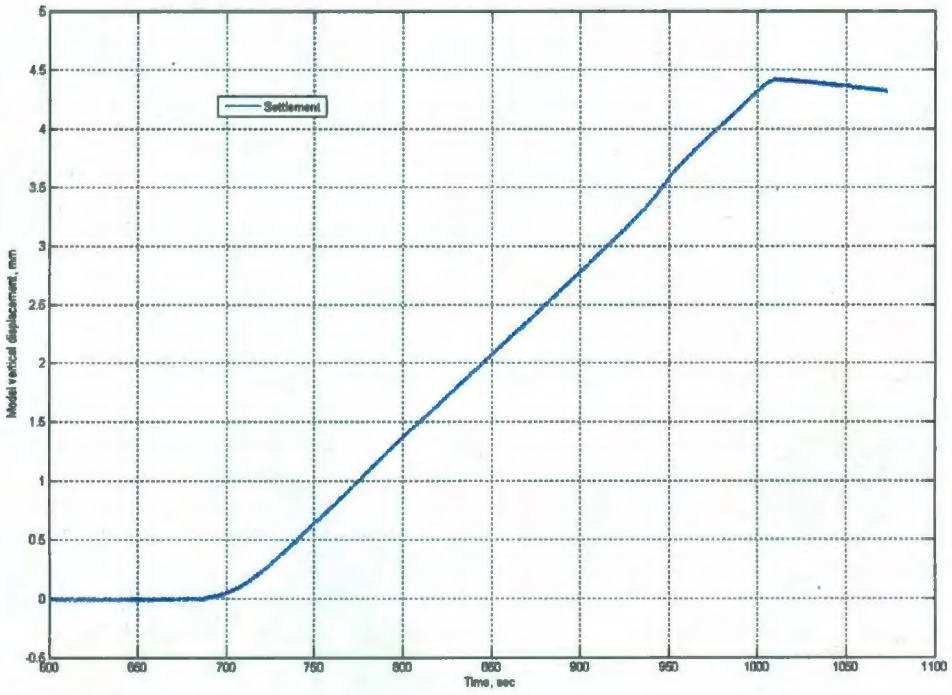

Figure A. 20 Model vertical settlement during centrifuge spin up for P09

Figure A. 21 Side view of gouge shape for test P03

Figure A. 22 Top view of gouge shape for test P05

Figure A. 23 Side view of gouge shape for test P06

Figure A. 24 Side view of gouge shape for test P07

Figure A. 25 Top view of gouge shape for test P07

Figure A. 26 Side view of gouge shape for test P08

Figure A. 27 Top view of gouge shape for test P08

Figure A. 28 Side view of gouge shape for test P09

Figure A. 29 Top view of gouge shape for test P09

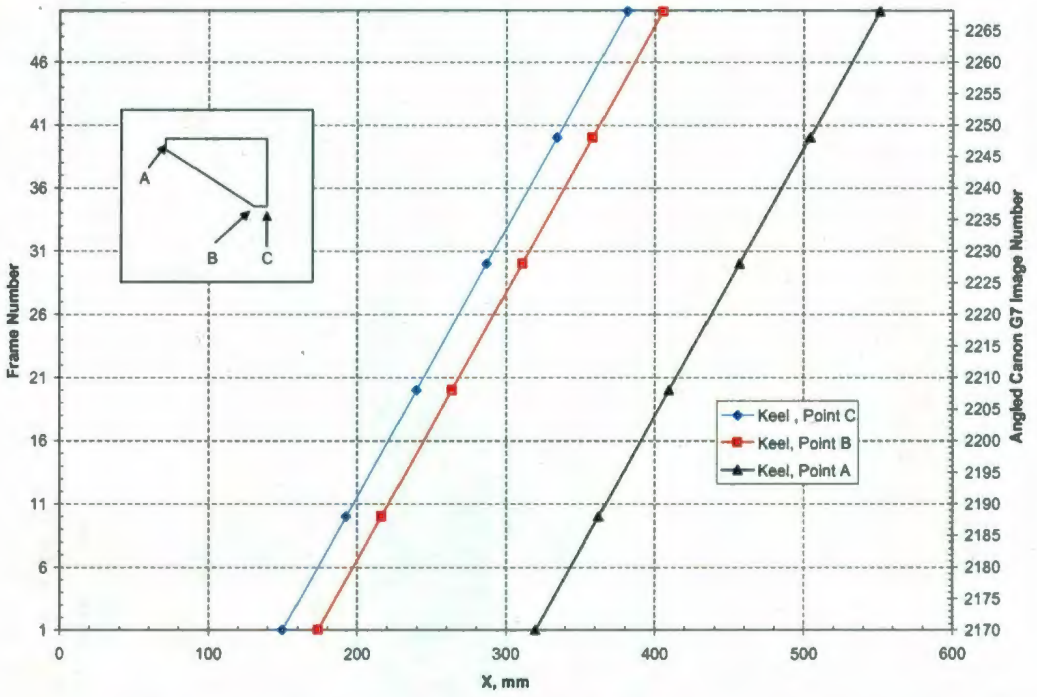

Figure A. 30 Frame number versus keel displacement for P02

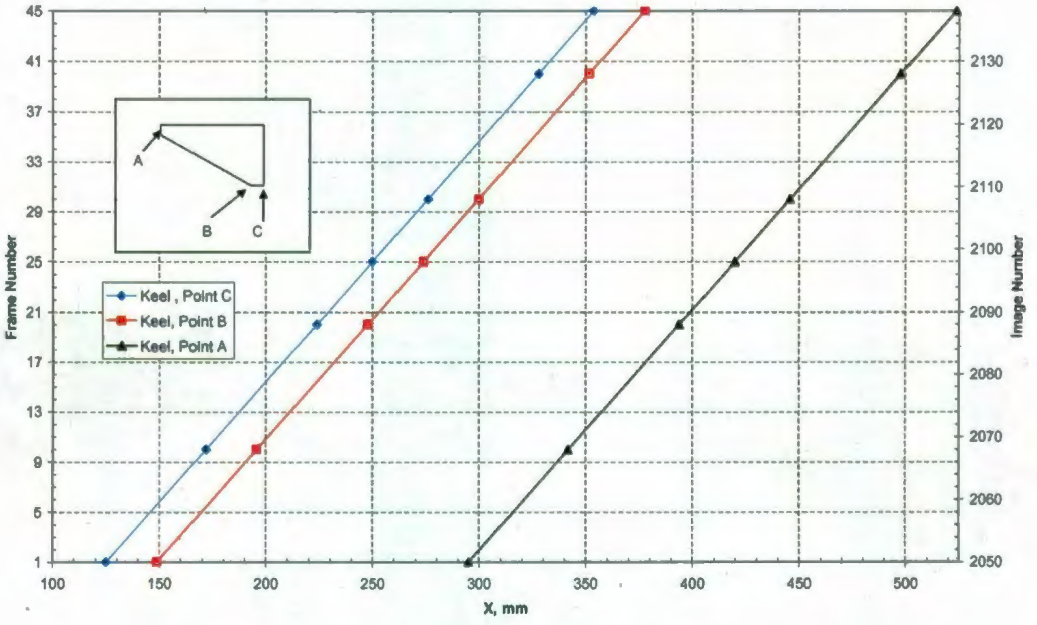

Figure A. 31 Frame number versus keel displacement for P03

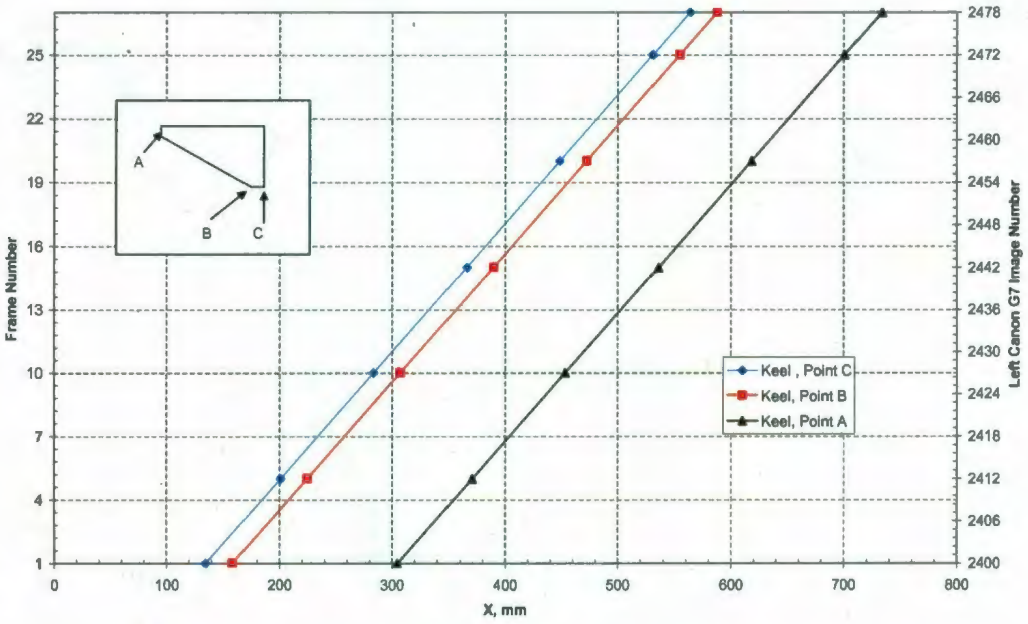

Figure A. 32 Frame number versus keel displacement for P05

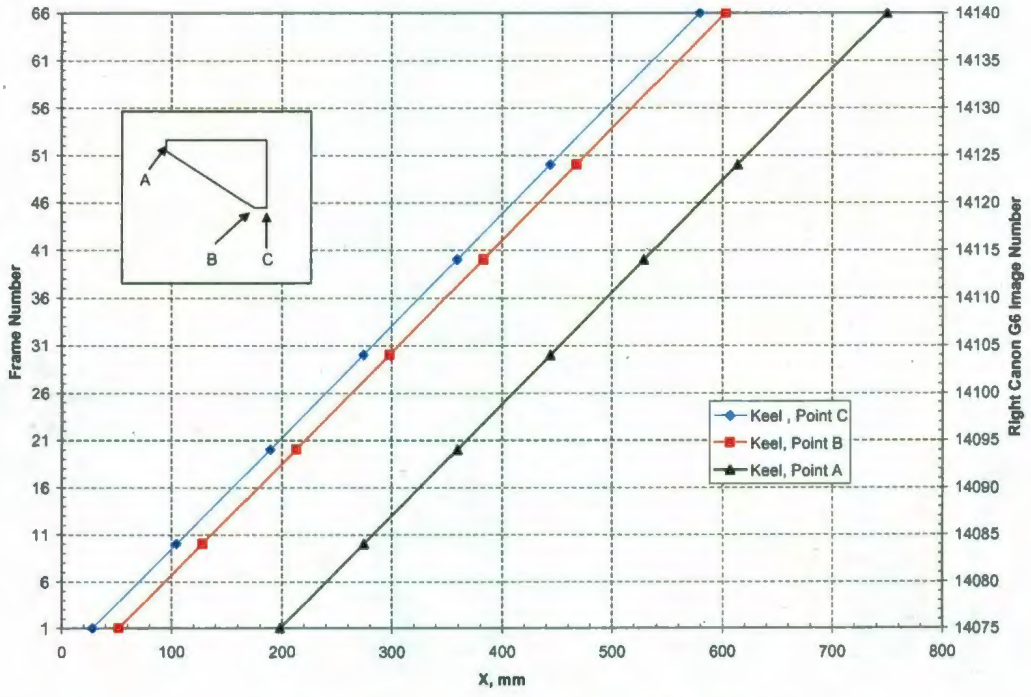

Figure A. 33 Frame number versus keel displacement for P06

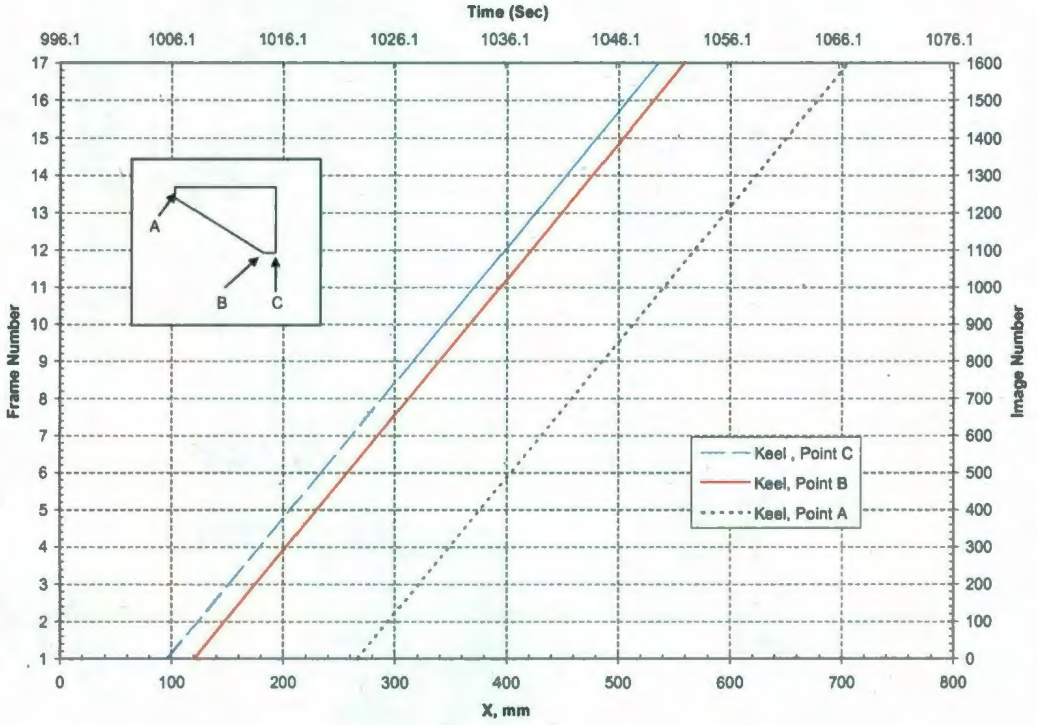

Figure A. 34 Frame number versus keel displacement for P07

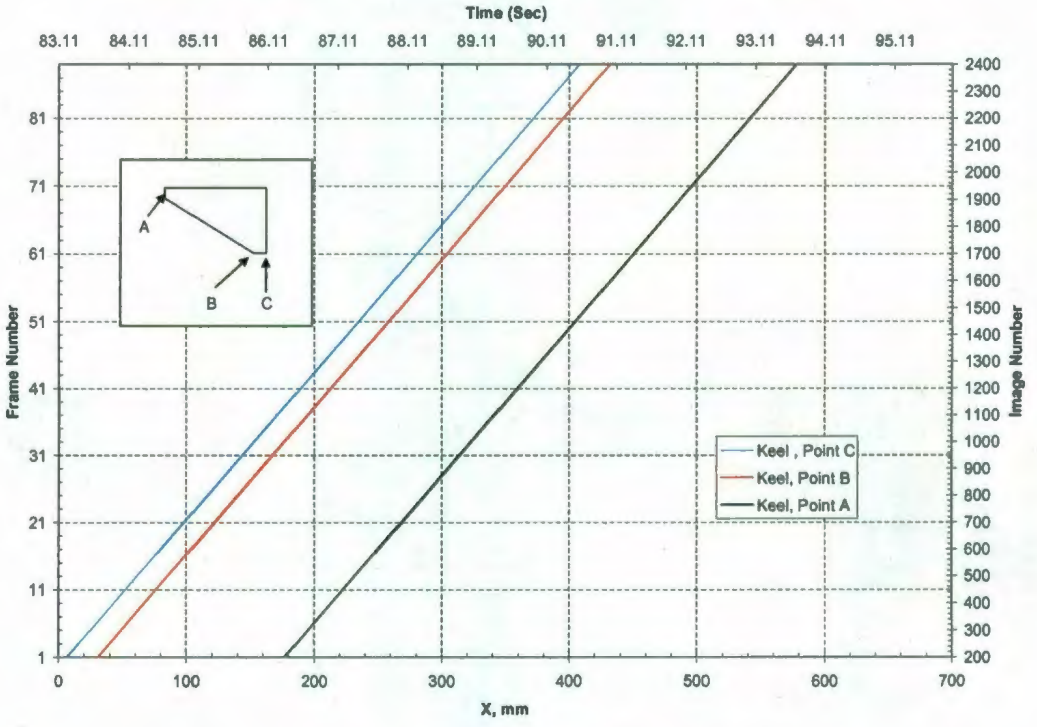

Figure A. 35 Frame number versus keel displacement for P08

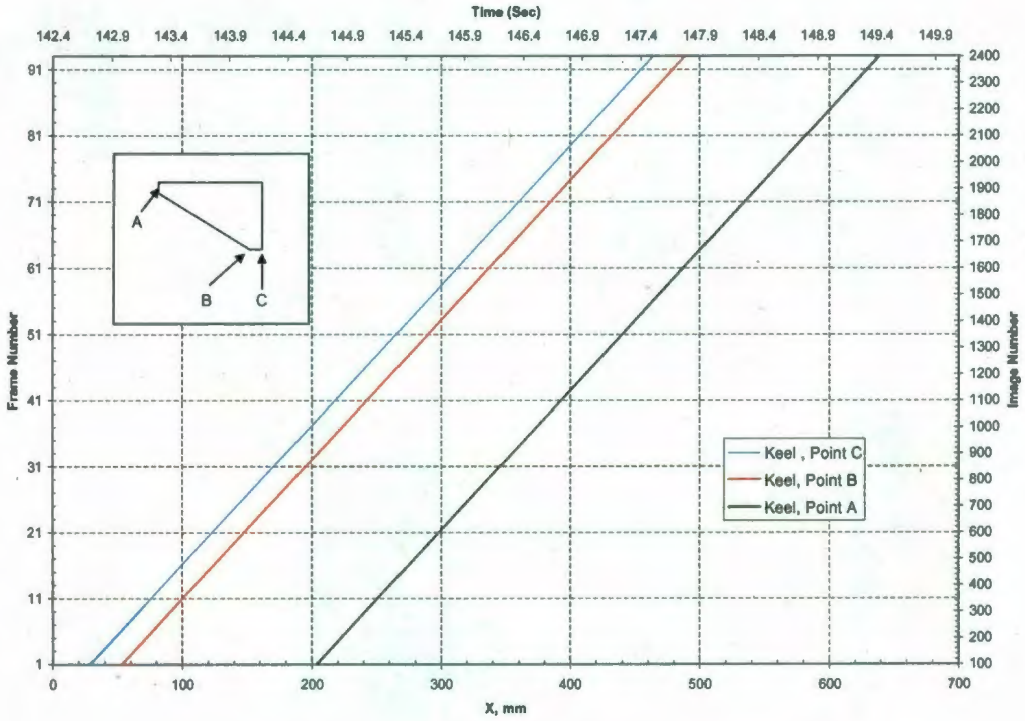

Figure A. 36 Frame number versus keel displacement for P09